Single-Cycle Non-Sequential Double Ionization

Matthias Kübel

München 2014

Single-Cycle Non-Sequential Double Ionization

Matthias Kübel

Dissertation
an der Fakultät für Physik
der Ludwig–Maximilians–Universität
München

vorgelegt von
Matthias Kübel
aus Gießen

München, den 12. Mai 2014

Erstgutachter: Prof. Dr. rer. nat. Matthias F. Kling
Zweitgutachter: Prof. Dr. rer. nat. Reinhard Kienberger
Tag der mündlichen Prüfung: 30. September 2014

Zusammenfassung

Nichtsequentielle Doppelionisation (NSDI) ist ein Paradebeispiel für eine gekoppelte Bewegung zweier Elektronen in einem starken Laserfeld. Der Effekt ist dadurch ausgezeichnet, dass die Ausbeute an zweifach geladenen Ionen gegenüber der sequentiellen Doppel-ionisation, bei der beide Elektronen unabhängig voneinander emittiert werden, um mehrere Größenordnungen erhöht [1] ist. Durch die Messung der Impulsverteilungen der doppelt geladenen Ionen [2, 3] und der korrelierten Elektronen [4] wurden weitreichende Erkenntnisse über die NSDI gewonnen. Aus diesen Ergebnissen wurde geschlossen, dass die nicht-unabhängige Emission zweier Elektronen eine Folge der lasergetriebenen Rekollision [5] des ersten Elektrons mit dem Mutterion ist. Trotz dieser Fortschritte sind die genauen Vorgänge während der durch Elektronen-Rekollision verursachten Ionisation noch nicht vollständig verstanden. Einer der Gründe dafür liegt darin, dass NSDI in Vielzyklen-Laserpulsen durch mehrfache Rekollision ausgelöst werden kann. Dies stellt eine große Herausforderung für die theoretische Beschreibung dar und erschwert die Interpretation experimenteller Ergebnisse.

In der vorliegenden Arbeit wird die Komplexität der NSDI deutlich reduziert, indem der Ionisationsvorgang auf ein einzelnes Rekollisionsereignis während des Laserpulses beschränkt wird. Dieses geschieht durch den Einsatz von Quasi-Einzelzyklen-Laserpulsen [6], deren absolute Phase in Echtzeit gemessen wird [7, 8]. Zudem ermöglicht uns die Verwendung eines Reaktionsmikroskops [9] die Durchführung von kinematisch vollständig bestimmten Experimenten bei denen Ionen- und Elektronenimpulse in Koinzidenz erfasst werden. In dieser Kombination [10] ergeben sich einzigartige Bedingungen, unter denen wir neue Einblicke in den NSDI-Vorgang innerhalb eines einzelnen optischen Zyklus gewinnen.

Das Fundament der Arbeit bilden die Untersuchungen zur Einzelzyklen-NSDI von Ar. Die dabei gemessene korrelierte Zwei-Elektronen-Impulsverteilung (kurz: Korrelationsspektrum) weist die Form eines Kreuzes auf. Folglich ist die durch das Laserfeld übertragene kinetische Energie asymmetrisch auf die beiden Elektronen verteilt: es gibt ein schnelles und ein langsames Elektron. Diese Beobachtung steht im Gegensatz zu allen bisherigen Experimenten, die mit Vielzyklen-Laserpulsen durchgeführt wurden. Dies legt nahe, dass sich die Mechanismen, die der Einzelzyklen-NSDI zugrundeliegen, von denen unterscheiden, die bei der Doppelionisation durch Mehrzyklen-Pulse maßgeblich sind. Als Ausdruck der ultrakurzen Pulslänge in unseren Experimenten, lässt sich die absolute Phase des Laserpulses so wählen, dass entweder eine oder zwei Rekollisionen während des Laserpulses die Doppelionisation auslösen. Durch das Unterdrücken weiterer Rekollisionen wird die Interpretation der experimentellen Daten deutlich vereinfacht. So wird es möglich, die Emission der beiden Elektronen auf einer Sub-Femtosekundenzeitskala zurückzuverfolgen.

Aus der Übereinstimmung der experimentellen Ergebnisse mit den Vorhersagen eines semiklassischen NSDI-Modells lässt sich schlussfolgern, dass die Doppelionisation durch die Re-

kollisionsanregung des Mutterions und dessen anschließender Ionisation durch das Laserfeld [11, 12] erfolgt. Als wichtiges Ergebnis stellt sich heraus, dass sich die experimentellen Beobachtungen nur dadurch erklären lassen, dass der besetzte angeregte Zustand des einfachgeladenen Ions während des zweiten Ionisationsschritts vollständig ionisiert wird - und zwar vorzugsweise *vor* dem Erreichen des Feldmaximums. Die Anwendbarkeit des Modells wird durch die korrekte Vorhersage der Intensitätsabhängigkeit der gemessenen Einzelzyklen-NSDI-Spektren für Ar bestätigt.

Zudem liefert das Modell genaue Vorhersagen zur NSDI von N_2, wofür ebenfalls ein kreuzförmiges Korrelationsspektrum gemessen wird. Trotz dieser Ähnlichkeit zu Ar werden aber auch markante Unterschiede zwischen den NSDI-Spektren von Ar und N_2 beobachtet. Diese Abweichungen können im Rahmen des Modells erklärt werden, indem Unterschiede in den Spektren der elektronischen Zustände von N_2^+ und Ar^+ berücksichtigt werden.

Grenzen unseres Modells treten jedoch auf, wenn die NSDI durch längere Laserpulse verursacht wird. Mittels Experimenten im Übergangsbereich zwischen Einzelzyklen und Vielzyklenpulsen wird gezeigt, dass die Kreuzform des Korrelationsspektrums bei Pulslängen von wenigen Zyklen zusammenbricht. Wir weisen dabei nach, dass der Anteil von anti-korrelierter Elektronenemission an der NSDI-Ausbeute stark mit der Pulslänge ansteigt.

Aus technologischer Sicht stellen unsere Experimente die erste Anwendung der Einzelschussmessung der absoluten Phase über Zeiträume von einigen zehn Stunden dar. Bei der Datenauswertung hat sich die Notwendigkeit einer robusten Routine zur Phasenermittlung herausgestellt. Das in der vorliegenden Arbeit entwickelte Verfahren ermöglicht die zuverlässige Messung der phasenabhängigen (Doppel-) Ionisationsausbeute in einer Vielzahl von Experimenten.

Die Untersuchung der Dissoziationsdynamik mehratomiger Moleküle infolge der Doppelionisation durch ein einzelnes Rekollisionsereignis kann neue Einsichten in das Brechen chemischer Bindungen liefern. Bei der dissoziativen Ionisation von N_2O beobachten wir Phasenabhängigkeiten bei nahezu allen möglichen Fragmentierungen des asymmetrischen, drei-atomigen Moleküls. Aus den Daten lässt sich folgern, dass der Großteil der verschiedenen beobachteten Phasenabhängigkeiten dadurch erklärt werden kann, dass die Einfach- oder Doppelionisation durch geeignete Orientierung der Moleküle begünstigt wird. Allerdings ist dieser Mechanismus unzureichend, um die gemessene Phasenabhängigkeit der Abspaltung von O^+-Ionen zu erklären, was auf einen weiteren Einfluss des Laserfeldes hindeutet.

Einen besonders subtilen Effekt stellt die Kontrolle der Richtung der Protonenemission aus dem *symmetrischen* Acetylenmolekül (C_2H_2) durch die absolute Phase dar. Die Deutung dieser Beobachtung erfolgt mit Hilfe eines quantenmechanischen Modells, das einen neuartigen Kontrollmechanismus nahelegt, bei dem die Kopplung von Vibrationszuständen eine Asymmetrie in der Protonenemission verursacht.

Abstract

Non-sequential double ionization (NSDI) is a classic example for multi-electron dynamics in strong laser fields. It is characterized by an orders-of-magnitude enhancement in the yield of doubly-charged ions [1] as compared to sequential double ionization, where both electrons are emitted independently of each other. Measurements of the momentum distributions of doubly-charged ions [2, 3] and the correlated electrons [4] have provided much insight into the process. From these results, it was concluded that the non-independent release of two electrons is facilitated by the laser-driven recollision [5] of the first electron with the parent ion. However, the exact mechanisms governing the recollision-induced ionization are not yet fully understood. One of the reasons is that in multi-cycle laser pulses, NSDI may involve multiple recollisions, which represent a great challenge for the theoretical description and hamper the interpretation of experimental results.

Here, we significantly reduce the complexity of the NSDI process by confining the double-ionization dynamics to a single recollision event within the laser pulse. This goal is accomplished by employing carrier-envelope phase (CEP)-tagged [7, 8] near-single-cycle pulses [6]. Furthermore, the use of a reaction microscope [9] enables us to conduct kinematically-complete experiments by recording ion and electron momenta in coincidence. Combining near-single-cycle pulses with reaction microscopy [10] provides a unique condition under which we gain unprecedented insight into the sub-cycle dynamics of NSDI.

As the basis of the present work and test case for single-cycle NSDI, the double ionization dynamics of Ar are investigated. The measured correlated two-electron momentum distribution (briefly, correlation spectrum) exhibits a cross shape, which indicates totally asymmetric energy sharing between the two electrons. This observation contrasts all previous experimental results, obtained with multi-cycle pulses. This strongly suggests that the physical mechanisms that govern single-cycle NSDI differ from those that are relevant in the multi-cycle regime. Due to the ultrashort pulse duration in our experiment, the CEP can be chosen such that double ionization is triggered by either one or two recollisions during the laser pulse. Suppressing the contribution of further recollisions greatly simplifies the interpretation of the experimental data, enabling us to trace the two-electron emission on sub-femtosecond timescales.

Our experimental results agree well with predictions from a semi-classical NSDI model. On this basis, it is concluded that double ionization proceeds via the recollision excitation of the parent ion and its subsequent ionization by the laser field [11, 12]. Importantly, the experimental observations can only be explained by considering the depletion of the excited state population during the second ionization step. The applicability of the model is confirmed by the agreement of its prediction with the intensity dependence of measured single-cycle NSDI spectra for Ar.

Moreover, the model also yields accurate predictions for NSDI of N_2, for which a cross-shaped correlation spectrum is measured as well. Despite this resemblance to the case of Ar, distinctive

differences in the NSDI spectra of Ar and N_2 are observed. These differences can be accounted for in the model by considering distinctions in the excited-state spectra of Ar^+ and N_2^+.

Limitations of our model appear, however, when NSDI is driven by pulses with longer durations. By investigating the transition between the single-cycle and the many-cycle regimes experimentally, we show that the cross-shape in the correlation spectra abruptly collapses in the few-cycle regime. Moreover, the share of anti-correlated electron emission in the NSDI yield strongly increases with pulse duration.

From the technological point of view, our experiments represent the first application of CEP-tagging in a single measurement lasting tens of hours. In the course of data analysis the need for a robust CEP-tagging routine emerged. The procedure that was developed in the present work enables the reliable measurement of the CEP-dependent (double) ionization yields in numerous experiments.

Investigating the dissociation dynamics of molecules after double ionization by a single recollision event may provide new insight into the breaking of chemical bonds. Following single or double ionization of N_2O, we observe CEP-dependencies in nearly all fragmentation pathways of the asymmetric, triatomic molecule. The data indicate that the majority of the CEP dependencies can be explained by the orientation selectivity exerted on randomly oriented molecules by single and double ionization. However, this mechanism is insufficient to explain the CEP-dependence of O^+ emission from the dication, indicating further influence by the laser field.

A particularly subtle effect is observed in the fragmentation of acetylene (C_2H_2). Here, the preferential direction of proton ejection from the *symmetric* molecule can be controlled via the CEP. This result is interpreted in terms of a quantum mechanical model suggesting a novel control mechanism where the superposition of vibrational modes causes an asymmetry in the proton emission.

Contents

List of Figures

1. Introduction

Non-sequential double ionization is a fundamental process in strong-field physics. In this field, researchers investigate the interaction of matter with the enormous electric fields of intense laser pulses. The field strength in the laser focus is typically on the order of volts per ångström, which dwarfs those of large natural lightnings by a factor of several hundred thousand. The key to producing the required high light intensities is the capability of confining relatively small amounts of energy (typically micro- or millijoules) into inconceivably short periods of time. The duration of modern few-cycle laser pulses are measured in femtoseconds, several billion times shorter than a single stroke of a lightning flash[1].

Laser intensities in the regime portrayed above became accessible nearly four decades ago, when the birth of strong-field physics was marked by the discovery of *above threshold ionization* (ATI) [14]. When Agostini and co-workers studied the six-photon ionization of xenon with a high-power laser, they observed the formation of discrete peaks in the photo electron spectrum, spaced by the photon energy. The observation indicated that the atom tends to absorb more photons than the minimum number required for ionization. Over the past four decades, strong-field ionization of atoms has become a paradigm for strong-field-matter interactions.

A particularly interesting observation was made a few years later, when the yield of doubly-charged krypton ions generated in a laser focus was found to be orders of magnitude higher than expected [1]. The expectations arose from assuming that both electrons leave the atom independently of each other. Hence, the new observations suggested that the two electrons assist each other in the ionization process. This phenomenon, named non-sequential double ionization (NSDI), has been shown to exist for a large number of atomic and molecular species and has itself become a paradigm for correlated electron dynamics in strong fields.

Over the past 30 years, NSDI has been investigated using a multitude of experimental techniques based on the detection of the doubly-charged ions or the corresponding electrons. The most detailed information about the process is gained by coincidence electron-ion recoil momentum spectroscopy [9], which has enabled the direct observation of the final state of the correlated electron motion [3]. Despite this progress, the underlying processes are not yet fully understood. One of the reasons is that the interpetation of experimental results is severely hampered by the many degrees of freedom permitted by the multi-cycle laser pulses used in nearly all studies to date.

Recent progress in laser technology, however, has made possible the generation of laser pulses down to the duration of a single optical cycle. In attosecond physics [15], such laser pulses are exploited to study electron dynamics on sub-femtosecond timescales. An exciting application of few-cycle pulses is the control of electron motion in strong fields by tailoring the evolution of the

[1] A lightning flash contains several strokes of microsecond duration, separated by few milliseconds each. [13]

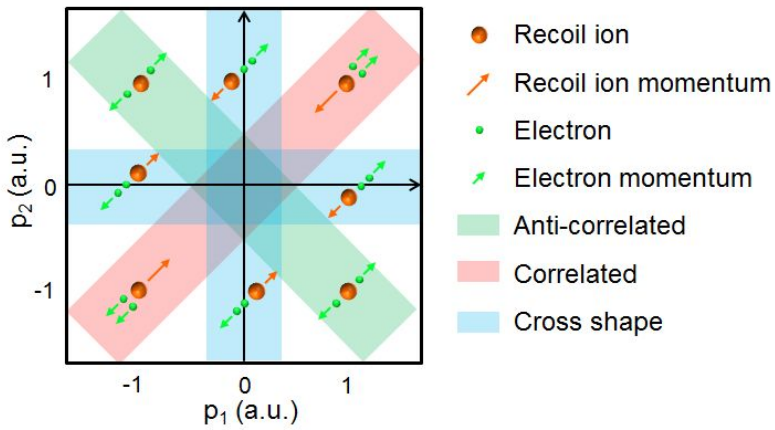

Figure 1.1.: Illustration of the momentum sharing between the two electrons (green spheres) and the ion (orange spheres) after double ionization. Events in the red area in the first and third quadrants correspond to correlated electron emission (i.e. the momentum vectors of the two electrons point to the same direction); events in the green area in the second and fourth quadrants correspond to anti-correlated electrons emission (i.e. the momentum vectors of the two electrons point to opposing directions. The blue cross-shaped area corresponds to events with totally asymmetric kinetic-energy sharing of the electrons along the laser polarization direction (i.e. one of the two electrons carries most of the kinetic energy).

electric field [16]. This capability has, for instance, led to the generation of isolated attosecond pulses [17].

The goal of the present work is to take advantage of the technological advances in ultrashort pulse generation to confine double ionization to an "isolated NSDI event". In this limit it becomes possible to trace back the emission times of both electrons during the interaction with the laser pulse.

The central diagram used in the present work is the correlated two-electron momentum distribution. In this diagram, the double ionization yield is plotted as a function of the momenta along the laser polarization of the first and second electron. As illustrated in figure 1.1, it allows for distinguishing various types of momentum sharing between the two electrons. Because the first and second electron are a priori indistinguishable, the spectra are invariant with respect to relabeling the two electron momenta (p_1, p_2) as (p_2, p_1). This results in a symmetry with respect to the main $(p_2 = p_1)$ diagonal.

2. Theoretical Background

During photoionization by a strong laser field, the atom's binding potential competes with the external laser field. For the propagation of the liberated electron, however, the interaction with the nuclear potential can be neglected in order to qualitatively explain many experimental observations. This fact is utilized in the very comprehensible "simple man's" model, which conveys an intuitive understanding of the relevant dynamics, including nonsequential double ionization. After an introduction to few-cycle pulses, the simple man's model is described in detail. The current status of research on nonsequential double ionization is reviewed in the final section of the chapter.

2.1. Few-cycle laser pulses

Laser technology has made enormous progress since the first observation of stimulated emission in ruby by Theodore Maiman in 1960 [18]. Being marked by the discovery of second harmonic generation in 1961 [19], it was realized early on that lasers enable the exploration of a new field of physics: nonlinear optics. Because nonlinear effects are strongly dependent on the laser intensity, there has been a thrive for higher laser power and shorter pulse duration. Nowadays it is possible to generate intense pulses down to the duration of a single optical cycle, and even less [20].

The electric field of a few-cycle laser pulse can be described as

$$E(t) = E_0(t) \sin(\omega t + \phi). \tag{2.1}$$

Here, $E_0(t)$ is the field envelope, ω is the carrier frequency and ϕ is the carrier-envelope phase (CEP). For practical purposes, it is useful to assume an envelope function $E_0(t) = E_0 \sin^2(t/\tau)$, where E_0 is the peak electric field and τ is the pulse duration. Choosing a $\sin^2$ envelope ensures a completely vanishing envelope at finite times. For near-single-cycle pulses, i.e. intensity envelopes with full width at half maximum (FWHM) duration on the order of an optical cycle, the CEP strongly determines the electric field evolution. By manipulating the temporal shape of the laser electric field via the CEP, it is possible to steer the motion of electrons on sub-femtosecond timescales [15]. This capability finds application in the measurement of the CEP [21, 22], in the generation of isolated attosecond pulses [16], in controlling molecular dissociation dynamics [23], or in driving dielectric currents [24, 22].

2.2. Strong-field photoionization

State-of-the-art few-cycle laser sources operate at near- or mid-infrared wavelengths. The photoionization yield of atoms and molecules by such pulses, whose photon energy is much smaller than the ionization potential, scales quasi exponentially with the intensity until saturation is reached, i.e. when the ionization probability approaches unity. As a rough estimate for the saturation intensity, the classical barrier-suppression intensity (BSI) may be employed. It is defined as the intensity for which the laser potential $-Er$ suppresses the coulomb potential $-Z/r^2$ below the ionization potential I_P of the bound state (Z being the nuclear charge of the ion remaining after ionization). Atomic units, $e = \hbar = m_e = 1/(4\pi\epsilon_0) = 1$, are used throughout. For the BSI one finds

$$I_{\mathrm{BS}} = \frac{I_P^4}{16Z^2}. \tag{2.2}$$

For intensities $I > I_{\mathrm{BS}}$, the *over-the-barrier ionization* regime is reached. Below the saturation intensity, ionization is often described as tunneling[1] through the potential barrier (see [26] for a review). Several formulas, such as the Ammosov-Delone-Krainov (ADK) rate [27], exist that provide approximate solutions for the tunnel ionization probability. In the present work, the formula suggested by Tong, *et al.*[28], was employed. In that work, the authors developed a parametrized extension for the ADK formula such that quantitative agreement with a numerical solution of the time-dependent Schrödinger equation is obtained in both, tunneling and over-the-barrier regimes.

Strong-field ionization depends on the CEP if the driving laser pulse is sufficiently short (see Ref. [29] for a review article). The effect of the CEP is particularly pronounced for recollision processes [30, 5] in which a liberated electron is driven back to its parent ion. These recollisions lead to phenomena such as the generation of fast photoelectrons (high-order above-threshold ionization [31, 32], ATI), emission of coherent extreme ultraviolet radiation (high harmonic generation, HHG) [33, 34], and non-sequential double (multiple) ionization [1].

The ”simple man’s” model

An intuitive understanding of strong-field phenomena is provided by the famous simple man’s model [5]. It states that photoionization can be thought of as a three-step process.

First, an electron is liberated from an atom or molecule by tunnel ionization at a time t_0. Typically, it is assumed that the electron is born with zero initial momentum, $p(t_0) = 0$.

Second, for times $t > t_0$ the electron is accelerated by the electric field of the laser, neglecting the interaction with the magnetic field of the laser and the nucleus.

Third, depending on t_0, the free electron may be driven back to the nucleus and undergo a recollision at time t_1, giving rise to the above mentioned recollision phenomena.

After ionization, the electron momentum at a given time $t > t_0$ can be calculated by integrating Newton’s equation of motion with the only force acting upon the electron being the acceleration

[1] Whether tunneling is an appropriate model to describe strong-field ionization below saturation can be inferred from the value of the Keldysh parameter [25].

by the laser field, $F = -E$ (the electron charge being -1)

$$p(t) = \int_{t_0}^{t} \dot{p}(t')\,\mathrm{d}t' = \int_{t_0}^{\infty} \dot{p}(t')\,\mathrm{d}t' - \int_{t}^{\infty} \dot{p}(t')\,\mathrm{d}t' = -A(t_0) + A(t), \tag{2.3}$$

where

$$A(t) = \int_{t}^{\infty} E(t')\,\mathrm{d}t', \tag{2.4}$$

with $A(t)$ being the vector potential of the laser field and $A(\pm\infty) = 0$.

Equation 2.3 is sufficient to calculate the final drift momentum $p(\infty)$ of *direct* electrons, which only interact with the laser field after ionization. Because, $p(\infty)$ is measured long after the laser pulse has passed, it is given by the vector potential at the instant of ionization $t = t_0$:

$$p_{\mathrm{drift}} = p(\infty) = -A(t_0). \tag{2.5}$$

In principle, equations 2.4 and 2.5 qualitatively explain the shape of photoelectron spectra: the vector potential has an extreme value whenever the electric field experiences a zero-crossing, and vice-versa. Hence, the spectra exhibit a low yield at high electron energies and a high yield at low electron energies. When considering few-cycle fields, even CEP-dependencies of the photoelectron spectra can be derived from these simple considerations. The details are outlined in Ref. [35].

For further discussion, it is useful to introduce the ponderomotive potential U_P, defined as the cycle-averaged oscillation energy of a free electron in a monochromatic laser field:

$$U_p = \frac{1}{2}\left\langle \frac{E_0^2}{\omega^2}\sin^2(\omega t)\right\rangle = \frac{E_0^2}{4\omega^2}, \tag{2.6}$$

where E_0 is the peak value of the electric field. Using equation 2.6, the peak value of the vector potential can be expressed as $A_0 = 2\sqrt{U_p}$. Hence, the maximum electron energies, expected from equation 2.5 are $2\,U_p$. This limit is known as the classical cut-off energy for direct electrons.

However, photoelectrons may acquire much higher energies than $2\,U_P$ during strong-field ionization, e.g. [31, 32]. Such higher photoelectron energies are predicted by the simple man's model when considering recollisions with the parent ion. The electron momentum at time of recollision, t_1, is

$$p_{\mathrm{recollision}} = A(t_1) - A(t_0). \tag{2.7}$$

Maximizing $p_{\mathrm{recollision}}$ under the condition that t_1 is a unique function of t_0 yields the maximum recollision energy of $3.17\,U_p$. Upon recollision, various interactions of the returning electron with the parent ions may occur. Recombination may lead to high-harmonic generation via the emission of a single photon with an energy of $p^2_{\mathrm{recollision}}/2 + I_P$. By elastically scattering off the parent ion, the electron is accelerated further in the laser field and can gain a final momentum

$$p_{\mathrm{resc.}} = -p_{\mathrm{recollision}} - A(t_1) = -2A(t_1) - A(t_0). \tag{2.8}$$

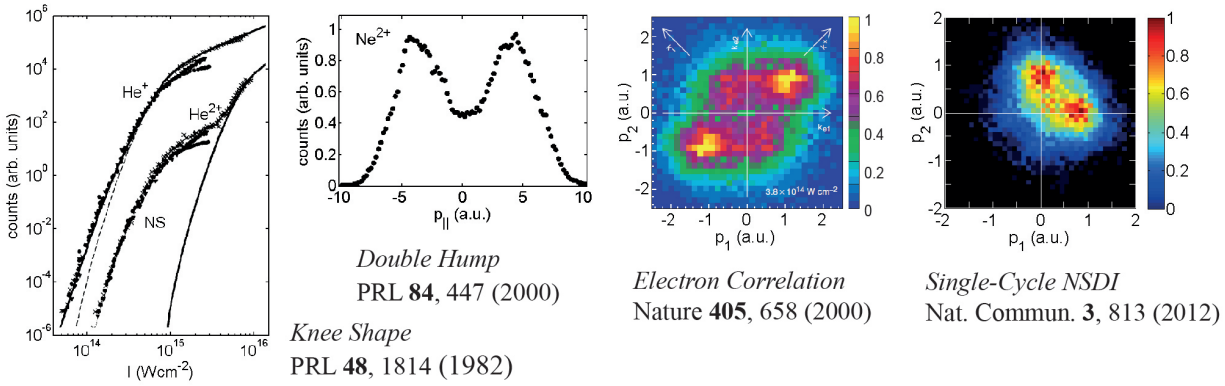

Knee Shape
PRL **48**, 1814 (1982)

Double Hump
PRL **84**, 447 (2000)

Electron Correlation
Nature **405**, 658 (2000)

Single-Cycle NSDI
Nat. Commun. **3**, 813 (2012)

Figure 2.1.: Milestones in the experimental research of strong-field nonsequential double ionization. Shown are the key signatures of NSDI with the publications in which they first appeared. See text for details. Figure adapted from Refs. [42, 2, 3] and publication 7.1. Figure inspired by Ref. [40].

The maximum energy that can be reached by *rescattering* is $10\,U_p$, which corresponds to the cut-off observed in measured photoelectron energy spectra [32].

Finally, inelastic scattering may lead to electron impact excitation or ionization of the parent ion, resulting in nonsequential double ionization (NSDI).

The simple man's model outlined here represents a simplified and - with the exception of tunnel ionization - classical description of strong-field ionization and related phenomena. It fails to predict structures in the spectra of both ATI and HHG. A more accurate description of these phenomena is given by a quantum mechanical treatment of ATI (see Ref. [36] for a review) and HHG [37]. Recently, also quantum effects in NSDI have attracted considerable attention [38, 39].

2.3. Nonsequential double ionization

In this section the state of research on NSDI is briefly described (see Refs. [40, 41] for recent review articles) and the present work is motivated. Two physical mechanisms which have been suggested to underlie NSDI are discussed in detail.

2.3.1. State of research

Research on NSDI has a thirty-year long history. During this time, experimental techniques in atomic, molecular and optical physics have made significant progress and NSDI has been a prototype application for those new technologies. The original signature of NSDI is the "knee" shape in the intensity-dependent strong-field double ionization yield curve, as reported by L'Huillier, *et al.* [1] for rare gases. This observation constitutes the first milestone in figure 2.1. There, the

measured yield for singly- and doubly-charged He ions[2] [42] is plotted as a function of the laser intensity and compared to theoretical predictions assuming the independent release of both electrons, shown as a solid line. The experimental findings for the double ionization yield were found to be inconsistent with the predictions over a broad intensity range (marked with NS for nonsequential). It was concluded that the theoretical description of NSDI must include a mechanism correlating the emission of the two electrons in order to explain the observations. Several such mechanisms were suggested, including collective tunneling, shake-off ionization, and electron impact ionization upon rescattering of the first electron.

Cold target recoil ion momentum spectroscopy (COLTRIMS) [43, 9] has enabled the measurement of the recoil momentum distribution of the doubly-charged ions [2]. In the NSDI regime, a characteristic double hump structure in the momentum distribution of Ne^{2+} ions was observed. This double peak represents the second milestone in figure 2.1. It indicates that at least one of the two electrons carries a non-zero momentum, and, hence, is not liberated at the peak of the electric field. This observation gave strong support to the recollision scenario, where double ionization is triggered by the laser-induced inelastic collision of a first liberated electron with its parent ion.

An impressive confirmation of the recollision model was finally given by a kinematically complete experiment, where ion and electron momenta were measured in coincidence. The correlated two-electron momentum distribution for NSDI of Ar (briefly, correlation spectrum or two-electron spectrum), measured by Weber *et al.* [3], constitutes the third milestone. It is characterized by a strongly correlated emission of both electrons into the same direction. At high intensities, the correlated pattern was shown to change into an uncorrelated one, as expected for sequential double ionization, where the emission of the second electron occurs independently of the first one.

The two-electron distribution in the third panel of figure 2.1 also features a minor signal in the top left and bottom right quadrants. It was found later that this signal of *anti-correlated* electron emission is the dominant contribution to NSDI of Ar at relatively low intensities [44]. Supported by fully-classical calculations [45], multiple recollisions were invoked to explain the dominance of anti-correlated electron emission at low intensities.

Beyond fully-classical models, multiple recollisions represent a great challenge for the theoretical description, hampering the interpretation of the experimental results.

A way around the multiple-recollision problem is the use of near-single-cycle laser pulses. At the beginning of this thesis work, measurements in this highly-interesting regime have been restricted to recoil-ion spectra [46, 10]. These studies have shown that NSDI exhibits a strong CEP-dependence. The latter work by Johnson *et al.* represents a considerable improvement regarding the CEP-resolution. In their experiment, CEP-resolved ion momentum spectra were recorded, rather than ion momentum spectra at specific CEP values. This progress has been made possible by the single-shot measurement of the CEP [7, 8], and association of the measured CEP with the ion spectra recorded on a single-shot basis (see section 3.3). The sub-cycle dependence of electron correlation spectra has been explored in various theoretical studies [47, 48]. However,

[2]The original paper [1] reports the measurement of the yields of singly- and multiply-charged Kr ions. The observations are qualitatively the same.

it had not been accessed experimentally before the work described in this thesis.

2.3.2. Mechanisms

In experiments on NSDI, the correlation spectra have been found to depend strongly on the parameters of the applied laser field (intensity [49, 50], pulse duration [50], wavelength [51]), and on the target atom or molecule [52, 49]. To explain the diverse ion and electron spectra, which were measured, several physical mechanisms within the recollision picture of NSDI were proposed. The corresponding models differ in the required electron recollision energy to trigger the second ionization. They have been successfully applied to describe a variety of experimental outcomes. In the present work, the theoretical interpretation focuses on the recollision excitation with subsequent ionization (RESI) mechanism. Here, the recolliding electron excites the parent ion, which is subsequently ionized by the laser field. At higher recollision energy, an impact ionization, as in an (e,2e) collision, may take place. Recently, evidence for NSDI via the formation of a doubly-excited neutral state has been found at 800 nm [53, 54], as well as at 400 nm [38] laser wavelength. Such a mechanism requires even less recollision energy than RESI. A discussion of this mechanism is given in the recent work by Camus [55].

Recollisional impact ionization

The recolliding electron may liberate a second electron via an inelastic collision if its kinetic energy is equivalent to the second ionization potential of the parent ion. Given that the maximum recollision energy is $3.17\,U_P$, a threshold intensity of approximately $1.5 \times 10^{14}\,\mathrm{Wcm^{-2}}$ in an 800 nm laser field can be derived for NSDI of Ar via the (e,2e) mechanism. After the collision, both electrons are accelerated in the laser field. Thus, one expects the two electron momenta to be strongly correlated. In principle, information on the energy sharing between the two electrons during the collision can be inferred from the final difference momentum of the two electrons. However, this is under the assumption that no electron-electron interaction takes place in the continuum. In fact, it has also been demonstrated experimentally that mutual repulsion of the two electrons influences their final momenta in NSDI via the (e,2e) process [56].

Recollisional excitation and subsequent ionization

Instead of emitting a second electron, the parent ion might be excited upon recollision. Subsequently, the laser field can ionize the excited ion, determining the time of birth of the second electron. The finite delay between electron recollision and the emission of the second electron is a key property of the RESI mechanism. In Ar^+, the lowest excited state lies 13.5 eV above the ground state. This corresponds to an intensity threshold of roughly $7 \times 10^{13}\,\mathrm{Wcm^{-2}}$ for recollisional excitation at the laser wavelength of 800 nm. Notably, the ionization potential of of the lowest-excited state of Ar^+,14.1 eV, corresponds to a barrier-suppression intensity (eq. 2.2) of only $4 \times 10^{13}\,\mathrm{Wcm^{-2}}$. Hence, the population in this excited state can be efficiently depleted by the laser field. This fact will constitute a central argument in the interpretation of the experimental results.

In our NSDI simulation, depletion is taken into account by using rate equations for the calculation of ionization yields. The degree of depletion is found to significantly influence the calculated two-electron spectra. The role of depletion in the simulation results is discussed in section 4.2. The simulation results are also significantly influenced by the excited state used in the simulations. This dependence is discussed in section 4.4. If not otherwise specified, the lowest excited state of Ar was chosen for all simulations.

In our simulations a free parameter, the scattering angle β, influences the final drift momentum of the first electron. β is defined as the angle between the momentum vectors just before and just after the recollision. See section A for a discussion of the scattering angle.

3. Experiment

Essentially three prerequisites exist for the experiments carried out in the present work: first, a reaction microscope (REMI) for the coincident measurement of electron and ion momenta, second, a laser source capable of producing near-single-cycle laser pulses, and third, the knowledge of the carrier-envelope phase of each and every laser pulse. In this chapter, the laser source, the reaction microscope and the stereo-ATI phase meter are briefly described. The chapter closes with details on the data analysis.

3.1. Near-single-cycle laser source

Two laser sources, both based on a Femtopower Compact Pro amplifier by Femtolasers GmbH were used in the present work. Before July 2011, experiments were carried out at the AS-1 beamline at the Max Planck Institute of Quantum Optics. This laser provided sub-4 fs laser pulses with a pulse energy of up to 0.5 mJ at a repetition rate of 3 kHz. After the move of the set-up to the Ludwig-Maximilians-Universität (LMU) a 10 kHz laser delivering equally short pulses with a pulse energy of up to 150 μJ became available.

To achieve the broadband spectra required for near-single-cycle pulses, the amplifier output beam (ca. 25 fs duration with a central wavelength of 785 nm) was focused into a 1 m long hollow-core fiber filled with either approximately 3 bar of Ne (AS-1) or 0.7 bar of Ar (LMU). The coherent white light generated by self-phase modulation in the gas-filled fiber covers a spectral range from approximately 350 to more than 1050 nm. The positive chirp inherent to this supercontinuum is compensated in the spectral range from approximately 500 to 1000 nm using dispersive multi-layer mirrors developed and manufactured at the LMU [57]. By fine-tuning the dispersion with a pair of fused-silica wedges a pulse duration of less than 4 fs full-width-at-half-maximum (FWHM) of the intensity envelope can be achieved, corresponding to about 1.5 optical cycles at the carrier wavelength of 750 nm. At the AS-1, this pulse duration was verified by attosecond streaking [58]. At the LMU, the pulse duration was measured indirectly by comparing the CEP-dependent asymmetries in above-threshold-ionization photoelectron spectra to previous measurements (see section 3.3) and simulations.

3.2. The Reaction Microscope

A detailed overview on reaction microscopy and various applications is given in the review article by Ullrich, *et al.* [9]. In this section, the apparatus used in the present work is described and details relevant to the conducted experiments are outlined.

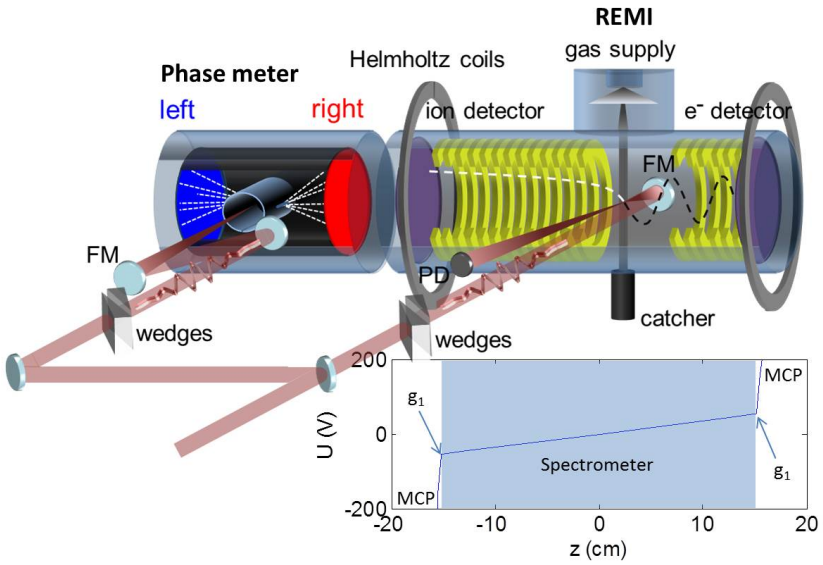

Figure 3.1.: Schematic view of the experimental setup. The laser beam is split in two parts. One part is sent to a Stereo-ATI phase meter (see section 3.3) for CEP characterization, shown on the left. The other part is back-focused into a cold gas jet in the REMI, shown on the right. Ions and electrons generated in the laser focus are detected by position-sensitive time-of-flight detectors on either side of the REMI. The charged particles are guided by homogeneous electric and magnetic fields to achieve detection over the full solid angle of 4π. The acceleration voltages inside the spectrometer are indicated in the inset. See text for details. Figure adapted from Ref. [59]

The reaction microscope is displayed on the right hand side of figure 3.1. It consists of a main chamber, in which an ion/electron sprectrometer[1] is mounted, a mirror chamber, and a cold gas jet. The ultra-high vacuum chambers are pumped by several turbomolecular pumps, which allow for achieving base pressures below 10^{-10} mbar in the main chamber after approximately 3 days of baking at 100-130°C.

On top of the main chamber, the gas jet is mounted. It includes a supersonic nozzle with a $30\,\mu\mathrm{m}$ open diameter and a skimmer pair (diameter $200\,\mu\mathrm{m}$) which facilitates sufficient cooling of the target gas to enable the measurement of recoil ion momenta. Furthermore, the atoms or molecules emitted from the jet cross a piezo-driven slit which allows for adjusting the width of the target along the laser propagation direction and thereby efficiently controlling the number of ions (and electrons) generated per laser pulse.

The incoming laser beam is back-focused into the gas jet by a spherical mirror mounted within the UHV chamber at a distance of approximately 25 cm from the gas jet. The laser focus is situated in the center of the ion/electron spectrometer consisting of 32 equidistant annular electrodes, which are separated by 8 mm each. Resistors of $100\,\mathrm{k}\Omega$ between adjacent electrodes are used to

[1]Here, Cold Target Recoil Ion Momentum Spectroscopy (COLTRIMS) denotes the measurement of recoil ion momenta, a REMI additionaly includes a time- and position-sensitive electron detector.

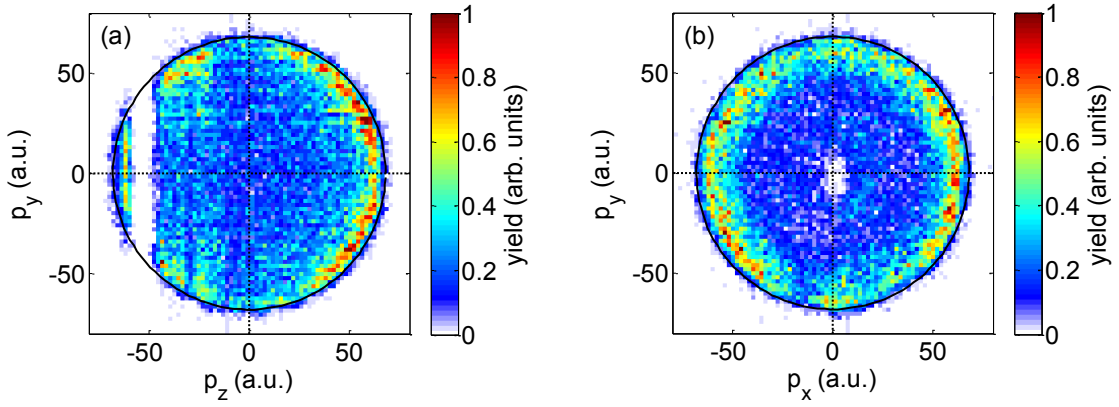

Figure 3.2.: Momentum maps of C^+ ions from the dissociation of $C_2H_2^{2+}$ after isomerization of $HCCH^{2+}$ to CCH_2^{2+} induced by few-cycle laser pulses polarized along the z axis. (a) in the (y, z) plane, (b) in the (x, y) plane. The black circle is drawn to guide the eye.

create a homogeneous electric field between both ends of the spectrometer (see inset in figure 3.1), where the ion or electron detector are located. Two meshes, g_1 and g_2, to which adjustable voltages, V_{g_1} and V_{g_2}, can be applied, are mounted in front of each detector. The voltage V_{g_1} is chosen such that a homogeneous field within the spectrometer is maintained. The second mesh on either side allows rejecting undesired signals by an additional potential barrier, and repelling cations from the electron detector, or electrons from the ion detector, respectively.

A pair of Helmholtz coils is used to generate a homogeneous magnetic field parallel to the electric field of the spectrometer. The magnetic field enables electron detection in a 4π solid angle, as discussed in section 3.2.2.

The laser beam exits the REMI through a window. This allows for monitoring the laser power (or pulse energy), or imaging the focus inside the REMI.

3.2.1. Recoil ion detection

After passing the meshes, g_1 and g_2, particles with charge Z are accelerated to a well-defined energy ZV_{CP1}, where $V_{CP1} \approx -2700\,\mathrm{V}$ is the voltage on the front side of a 75-mm diameter chevron stack multi-channel plate (MCP) detector. Due to this acceleration, the detection probability becomes independent of the initial particle energy. The detection efficiency is typically limited to about 50% by the geometry of the MCP surface. The impact of the particle on the MCP gives rise to a time-of-flight (TOF) signal at time t_{CP} and triggers the generation of an electron avalanche, accelerated towards the back of the MCP stack with a voltage of $V_{\mathrm{CP2}} \approx -500\,\mathrm{V}$. The electron cloud generated in the MCP stack is further accelerated towards a two-dimensional delay-line anode (RoentDek), allowing for the readout of the impact position (x, y) on the detector. Using (x, y, t_{CP}), the three-dimensional momentum vector (p_x, p_y, p_z) can be calculated. This requires the following parameters: length of the spectrometer $l = 15.95\,\mathrm{cm}$, spectrometer

voltage V, mass m and charge q of the ion, as well as time zero t_0, at which the laser pulse interacts with the target gas. In order to determine t_0 it is useful to make use of the relationship between the TOF of an ion and its mass-to-charge ratio, $t_{\mathrm{CP}} = k\sqrt{m/q} + t_0$, where k is a constant.

The consistency of the calibration of the longitudinal (p_z) and transversal (p_x, p_y) momenta can be verified by the circular shape of the momentum image for ions generated at a discrete energy in the dissociation of molecules, as exemplified by fragments from the laser-induced isomerization of acetylene to vinylidene in figure 3.2.

3.2.2. Electron detection

To account for the negative charge of electrons, the front MCP side of the electron detector is at a low positive voltage $V_{\mathrm{CP2}} \approx 200\,\mathrm{V}$, and the back side of the MCP is at a high positive voltage $V_{\mathrm{CP1}} \approx 2200\,\mathrm{V}$.

As compared to ions, electrons gain much higher velocities in the laser field. Hence, they would often miss the detector without further guidance. This problem is circumvented by applying a homogeneous magnetic field along the spectrometer axis using a pair of Helmholtz coils. The magnetic field B confines the electrons to spiral trajectories with the characteristic cyclotron period

$$T_{cyc} = \frac{2\pi m}{qB}, \tag{3.1}$$

and radius

$$r_{cyc} = \frac{p_\perp}{qB}, \tag{3.2}$$

where $p_\perp$ is the transversal momentum perpendicular to the magnetic field.

For a typical magnetic field of $0.9\,\mathrm{mT}$, generated by a current of about 40 A in the present Helmholtz coils, the cyclotron period is $T_{cyc} = 39.7\,\mathrm{ns}$. This period and the cyclotron trajectories are conveniently observed in an r-TOF spectrum (as shown in figure 3.3), where the electron yield is plotted as a function of the radial impact position and the time-of-flight. The nodes in the radial distribution occur at integer multiples of T_{cyc} when the electrons have completed an integer number of round-trips along their spiral trajectories. This fact can be exploited to calibrate the TOF offset t_0 with sub-ns accuracy. The cyclotron trajectories have to be taken into account for the calculation of the 3D electron momenta.

While the delay-line detector allows for the measurement of the impact position of an individual particle, its capability to detect several particles within a brief period of time is limited by a so-called “dead time”. This means, that after a particle has been registered, the detector is insensitive for a period of about 10 ns. The effect is present for electrons as well as for ions but is much more severe for electrons since all electrons arrive on the detector within a typical time window of the order of 100 ns, whereas the ions reach the detector within a time window of several µs. The dead-time issue will be further discussed in sections 3.4.2 and B.

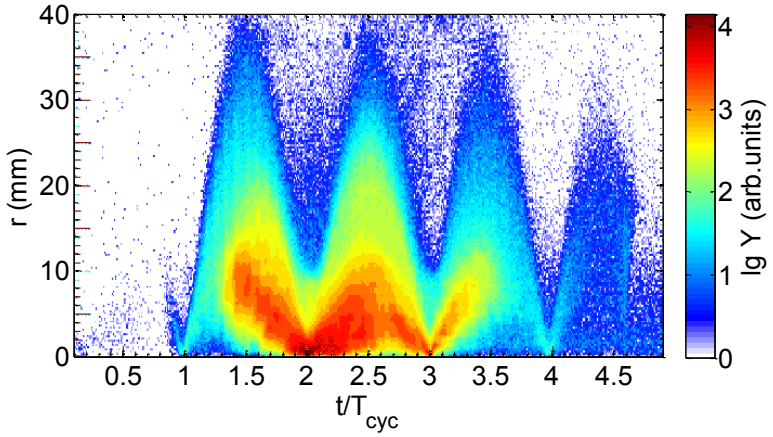

Figure 3.3.: Cyclotron trajectories in the r-TOF spectrum of photoelectrons generated by strong-field ionization of Ar. The electron yield is plotted as a function of the radial impact position and the time-of-flight of the photoelectrons in units of the cyclotron period T_{cyc}.

3.3. Phase-tagging with the Stereo-ATI

The capability of measuring the CEP of each and every single laser shot within a kHz pulse train is provided by the Stereo-ATI phasemeter [21, 7] and enables a new approach to CEP-resolved measurements: *phase-tagging* [8]. Instead of scanning the CEP of phase-stabilized laser pulses, the CEP of each laser pulse is measured. All physical quantities recorded synchronously on a single-shot basis are associated with the CEP of the pulse. A detailed description of the Stereo-ATI phasemeter and its application can be found in [60] and references therein.

The measurement of the CEP relies on the asymmetric electron emission in the strong-field ionization of rare gases by ultrashort laser pulses. Linearly polarized few-cycle laser pulses are focused into a Xe gas cell. Photoelectrons generated by above-threshold ionization of Xe atoms in the laser focus are detected on either side of the laser polarization axis using time-of-flight detectors. In each TOF trace, the ionization yield is integrated over two regions R_x and R_y (see figure 3.4) to calculate the asymmetry parameters $A_{x/y}$

$$A_{x/y} = \frac{N_{\mathrm{left},x/y} - N_{\mathrm{right},x/y}}{N_{\mathrm{left},x/y} + N_{\mathrm{right},x/y}}, \tag{3.3}$$

where $N_{\mathrm{left},x/y}$ ($N_{\mathrm{right},x/y}$) are the photoelectron yields in the left (right) TOF spectrum integrated over $R_{x/y}$. To retrieve the CEP ϕ of a laser pulse, it is useful to plot A_y as a function of A_x for every laser shot in a so-called parametric asymmetry plot (PAP), as displayed in figure 3.5. The resulting polar angle $\theta = \arctan(A_y/A_x)$ is related to ϕ via a continuous monotonic function $\phi(\theta)$. To retrieve $\phi(\theta)$, a sufficiently large ensemble of asymmetry values $A_{x/y}$ measured for laser

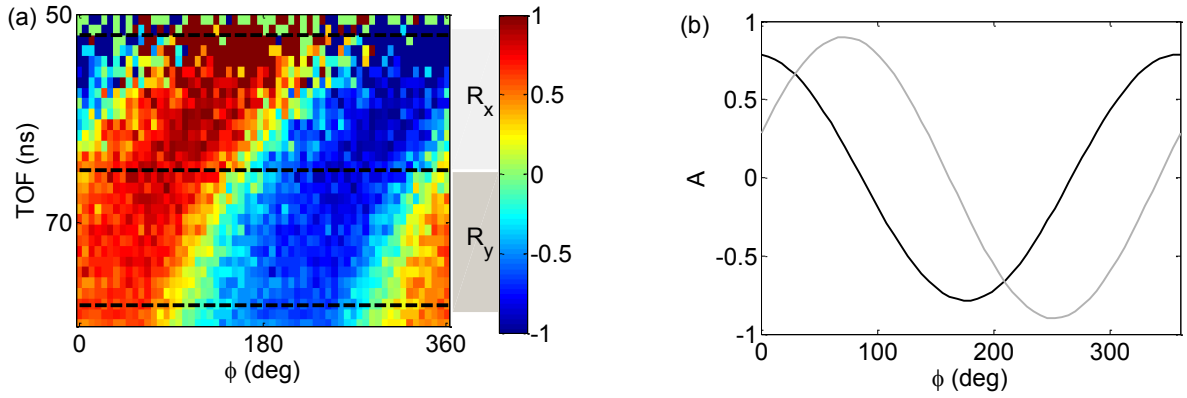

Figure 3.4.: (a) Example of an asymmetry map obtained by plotting the left-right asymmetry of the single ionization yield of a rare gas a function of TOF and CEP. This specific example is for ATI of Ar, which leads to qualitatively very similar results as ATI of Xe. The dashed lines mark the two TOF regions R_x and R_y over which the ionization yields in the left and right TOF spectra are integrated to calculate the CEP-dependent asymmetries A_x and A_y plotted as gray and black curves in panel (b), respectively. Plotting A_y versus A_x for all CEPs yields a parametric asymmetry plot, as exemplified in figure 3.5.

pulses with uniformly distributed random CEP values is required. This ensemble is referred to as reference PAP. The details of the retrieval of ϕ are outlined in chapter 2 of publication 7.2.

Because the magnitude of $A_{x/y}$ is very sensitive to the number of optical cycles driving ionization, the Stereo-ATI can also be used to infer the pulse duration. In Ref. [61], an empirical formula relating the radius $r = \sqrt{A_x^2 + A_y^2}$ of the PAP to the pulse duration is given:

$$r = 1 - \exp\left(-\alpha/(\Delta t - \beta)^2\right), \tag{3.4}$$

where $\alpha = 9.7317 \pm 1.5069$ and $\beta = 1.66063 \pm 0.2593$. Using this expression, the pulse duration corresponding to the measured PAP displayed in figure 3.5, is determined as $3.7 \pm 0.3\,\mathrm{fs}$, which is in good agreement with experimental results and simulations presented in this work. The uncertainty given here includes systematic and statistical errors.

3.4. Data analysis

In this section, three aspects of important data analysis techniques used in the present work are described. In the first part, a method for accurate long-term CEP measurements, presented in publication 7.2, is outlined. The second part deals with the detection of coincident particles in the reaction microscope. Related to this, the retrieval of the correlated two-electron momentum

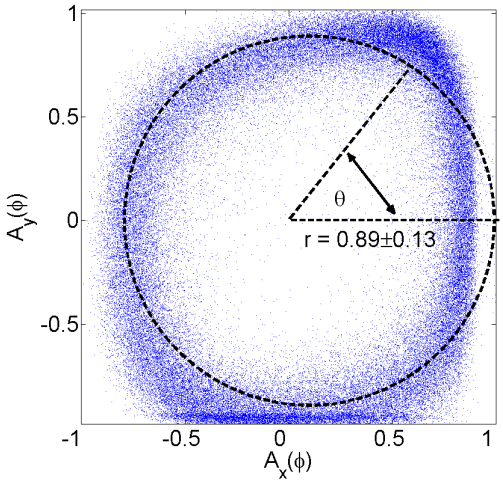

Figure 3.5.: Example for a parametric asymmetry plot, a so-called "phase potato", generated by sub-4 fs pulses. For each laser shot, the asymmetry value A_y is plotted as function of the asymmetry value A_x. The polar angle θ of each dot is related to the CEP ϕ of the corresponding laser pulse. Using an empirical formula [61] the laser pulse duration is estimated to be $3.7 \pm 0.3\,\mathrm{fs}$ from the radius r. See text for details.

distributions from the experimental data is discussed with the help of a computer simulation of the measurement process in the REMI in the third part.

3.4.1. Long acquisition times and CEP-dependent yields

In section 3.3, it was mentioned that a reference PAP is required to retrieve the function $\phi(\theta)$ used to obtain the CEP of a laser pulse from the measured asymmetry values $A_{x/y}$. It is clear that errors in the determination of $\phi(\theta)$ will lead to systematic errors in the CEP measurement. In experiments lasting many hours, the measured PAP can alter its shape over time.

The effect of slight changes in the PAP shape on the phase measurement has been studied in publication 7.2. Such slight changes are caused by the drift of laser parameters, as for instance intensity or pulse duration, in the experiment. Even though small variations of the PAP have only little impact on the precision of the phase measurement, the resulting errors hamper the accurate measurement of CEP-dependent ionization yields. This effect is discussed in detail in publication 7.2.

A quantitative analysis based on two measurements with an intensity difference of 7% suggests that intensity changes during an experiment can be made responsible for the observed changes in the PAP shapes. A solution to minimize the errors in the CEP measurement is provided by updating the reference PAP in sufficiently small time intervals throughout the experiment. For details, see publication 7.2.

The approach has been successfully applied to the measurement of the CEP-dependence of

the yield of Ar^{2+} ions generated by near-single-cycle laser pulses of various intensities, and in several further studies, such as the included publications and Ref. [62].

3.4.2. Gating coincidences

The coincident detection of ions and electrons is the essential capability of the REMI that enables kinematically complete studies of the double ionization process. Furthermore, coincidences of several ions allow for studying different fragmentation channels of a molecule. Coincident fragments are identified using momentum conservation.

In practice, coincident events are selected using a two-dimensional momentum sum condition, as exemplified in figure 3.6. The number of coincident events is plotted as a function of the momentum of the first particle p_1 and the momentum sum $p_1 + p_2$, where p_2 is the momentum of the second particle. Separate conditions are imposed for all three spatial dimensions. Such two-dimensional momentum sum condition has advantages over a one-dimensional histogram of $p_1 + p_2$, i.e. the projection of figure 3.6 onto the vertical axis. First, features such as the indicated dead-time hole or contaminations by other channels can be clearly identified. Second, the two-dimensional condition allows for testing the consistency of the parameters used in the momentum calculation. In case of an incorrect calibration of the parameters, the mean sum-momentum will be dependent on the particle's momentum, such that the main feature (inside the box) in figure 3.6 will assume a tilt. Such a tilt is easily recognized in the diagram due to the small scale of the y-axis as compared to the large scale of the x-axis.

Apart from providing access to otherwise unobservable dynamics, the coincident detection of electrons and ions allows for estimating the detection efficiency ϵ experimentally. In figure 3.7 (a) a two-electron momentum spectrum is shown for events where at least one electron was detected in coincidence with an Ar^{2+} ion. To generate the spectrum, the momentum of the second electron is calculated as the negative momentum sum of the ion and the fastest detected electron. The spectrum exhibits a clear asymmetry with respect to the $p_2 = p_1$ diagonal. This can be understood as follows. Whenever an Ar^{2+} ion is generated, there are also two electrons. Detecting the faster one of these occurs with a probability $P_1 = \epsilon$. In all of these cases the electron will appear on the top left half of the two-electron spectrum. The bottom right half is only populated when the faster electron is not detected but the slower one is. This occurs with a probability $P_2 = (1 - \epsilon)\epsilon$. Thus, the ratio of the yields in the bottom right, Y_2, and top left halves, Y_1, respectively can be used to determine ϵ,

$$X = \frac{Y_2}{Y_1} = \frac{P_2}{P_1} = (1 - \epsilon). \tag{3.5}$$

For the present image, $\epsilon = 0.53$ is deduced. In the above derivation it was assumed that no more than two electrons are detected. Even though additional background electrons may alter the result, the assumption is reasonable as in less than 3% of the detected double ionization events, more than two electrons were registered. Electrons that do not originate from double ionization of Ar, so-called *false coincidences*, preferentially appear in the marked regions of figure 3.7 (a), as determined by comparing figures 3.7(a) and (b). See also section 3.4.3.

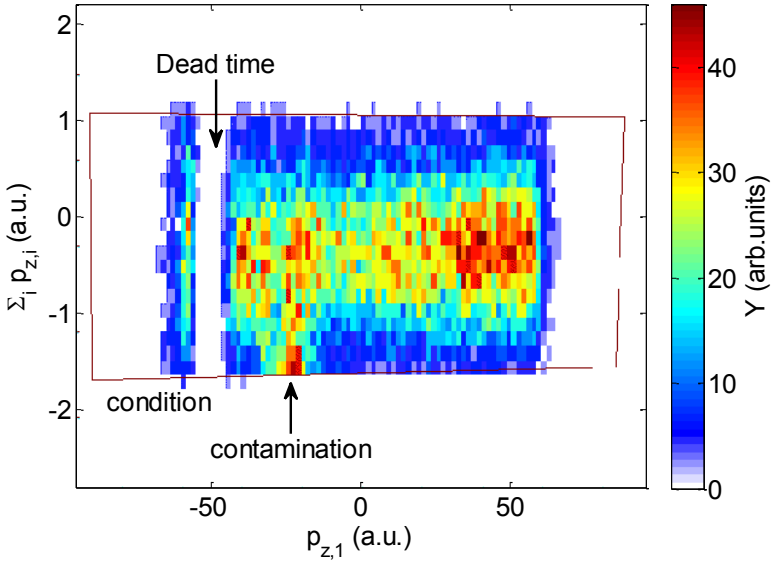

Figure 3.6.: Momentum conservation condition along the z axis for the breakup of $C_2H_2^{2+}$ into C^+ and CH_2^+. Shown is the fragmentation yield as a function of the longitudinal C^+ momentum $p_{z,1}$ and the longitudinal momentum sum with $p_{z,2}$ being the longitudinal CH_2^+ momentum. The detector dead time causes a gap with no detected coincidences when the time-of-flights of the two particles are nearly identical. Contamination by the symmetric breakup channel $C_2H_2^{2+} \rightarrow CH^+ + CH^+$ is marked. The box indicates the condition used for the identification of coincident ions. Note that the width of the momentum sum corresponds to the sum momentum of the two electrons emitted during the double ionization of the neutral molecule.

Contrary to the detection of the first electron, the acquisition of further electrons is affected by the dead time of the detector. This is evident in coincidences of Ar^{2+} and two electrons. Because the detector is temporarily insensitive after registering an electron, a minimum TOF difference between the two electrons $t_2 - t_1 \approx 10\,\mathrm{ns}$ appears, as can be seen from the gap around the diagonal in figure 3.7(b). The few events close to the diagonal are false coincidences.

3.4.3. Correlated two-electron momentum spectra

In NSDI experiments, the vast majority (approximately 99%) of the detected ions and electrons originate from single ionization. Out of this abundance of detected electrons, the NSDI electrons have to be identified for the generation of the two-electron momentum distribution. According to the method for identifying coincidences, discussed in the previous section, the selection of the double ionization events would be made by imposing a momentum sum condition. Instead of requiring the sum of two momenta to be zero, the sum of three momenta would be required to

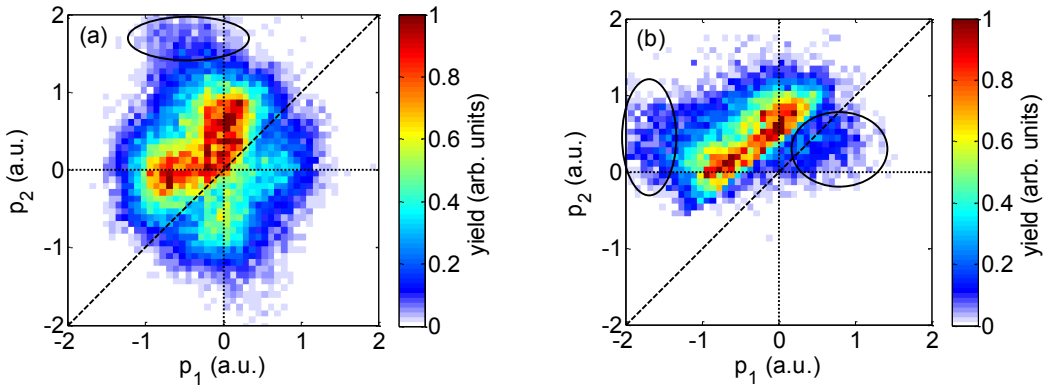

Figure 3.7.: Measured two-electron momentum spectrum for electrons detected in coincidence with an Ar^{2+} ion. In (a), p_1 denotes the measured momentum of the electron detected first, and p_2 is calculated as the negative momentum sum of the ion momentum and p_1. The integrals of the signal left and right of the diagonal allow for determining the detection efficiency (see text). The ellipses indicate regions with considerable false coincident background signal. In (b), p_2 is the measured momentum of the *second* detected electron, and p_1 is calculated as the negative momentum sum of the ion and p_2. The gap between the signal and the dashed diagonal is caused by the dead time of the detector.

vanish: $p_i + p_1 + p_2 = 0$, where p_i is the momentum of a doubly charged ion, and p_1, p_2 are the momenta of two electrons detected in coincidence with the ion. This procedure would work very well if a perfect electron detector with detection efficiency of 100% and without dead time was available.

The three-particle coincidences of a doubly charged ion and both emitted electrons are useful to verify the consistency of the momentum calibration (compare to figure 3.7 but they only constitute a small fraction (approximately 20%) of all detected double-ionization events, reflecting the limited detection efficiency. Furthermore, no more than one out of two electrons with very similar TOF is detected in all cases due to the dead time of the detector after detection of the first electron. Hence, in most cases only one electron momentum p_1 is measured and the second one has to be reconstructed from p_1 and the ion momentum p_i using momentum conservation. This procedure only yields a correct result if the detected electron was actually emitted from the detected ion. In order to ensure this, a low count rate $r \ll 1$ ions per shot must be used, such that it is statistically unlikely that more than one ion is generated per pulse. Electrons that are erroneously associated with a doubly-charged ion lead to false coincidences, distorting the experimental results.

In order to understand in which ways false coincidences and the imperfections of the electron detection affect the experimental results, a series of computer simulations of the measurement and retrieval process of the two-electron momentum distributions were performed. Details on these simulations are given in section B of the appendix. The most important result is that in

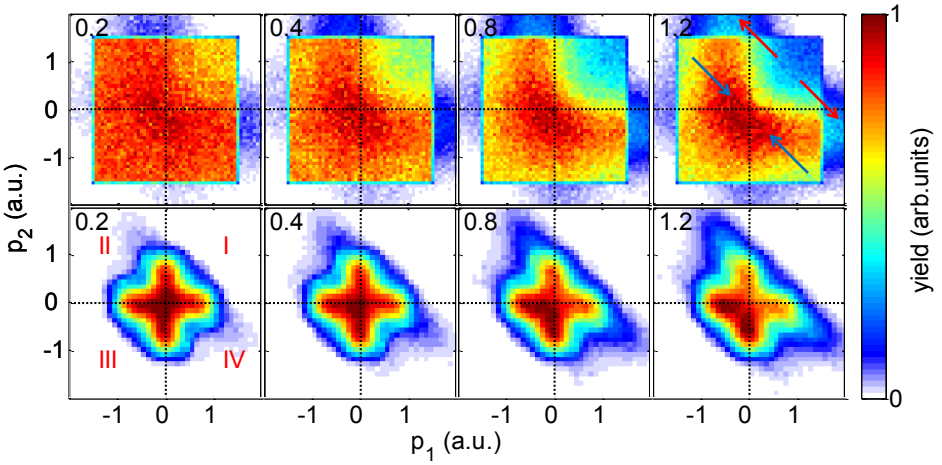

Figure 3.8.: Simulated impact of false coincidences on the retrieved correlation spectra. The top panels are for a hypothetical square distribution of momentum pairs. The bottom panels represents predicted correlation spectra from the semi-classical model. The panels are labeled with the average number of background electrons per laser shot used in the simulation. The Roman numerals in the bottom left panel indicate the labeling of the quadrants. The arrows in the top right panel indicate the direction in which signal is shifted through the contribution of false coincidences.

order to avoid artifacts, all events in which a doubly-charged ion and at least one electron were detected, should be considered for the generation of the two-electron momentum distributions. It is further found that systematic errors are inhomogeneously spread throughout the correlation spectrum and depend on the true distribution. Though a reasonably low impact of systematic errors in the full spectrum is only achieved for count rates $r < 0.2$ electrons per shot, spectra with an acceptable error level may be gained for count rates up to 1 electron per shot when symmetry properties of the two-electron distribution are exploited.

Using the simulations, a series of different approaches for the retrieval of the correlation spectra has been tested. The comparison of the approaches is discussed in section B. For generating the two-electron momentum distributions in this thesis the following method is used: all laser shots for which a doubly charged ion (momentum p_i) and at least one electron were detected, are considered. For each such event, a second electron momentum is calculated as $p_2 = -p_i - p_1$, where p_1 is chosen as the momentum of the "first" electron, i.e. the one with the shortest time of flight if more than one electron was detected[2]. The correlation spectrum is filled using the momentum pairs (p_1, p_2) and symmetrized with respect to the $p_2 = p_1$ diagonal.

To analyze the precision of the obtained two-electron spectra, the retrieval of two different

[2]Selecting a different electron than the first one for the generation of the correlation spectra introduces a few artifacts. See section B for a comparison between the results when alternative approaches to the generation of the two-electron spectra are used.

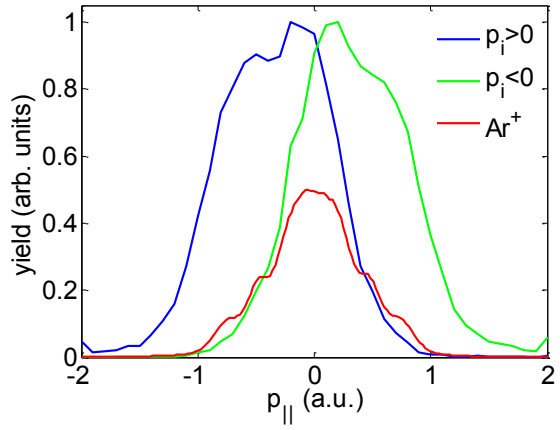

Figure 3.9.: Comparison of the momentum distributions of NSDI and ATI electrons. Shown are measured momentum distributions for electrons detected in coincidence with Ar^{2+} ions with momenta $p_i > 0$ and $p_i < 0$, normalized to 1. These are compared to the measured Ar^+ momentum spectrum, normalized to 0.5 for visual convenience. See text for discussion.

distributions was simulated for different count rates of background electrons. It can be seen in figure 3.8 that the resulting spectra exhibit a pronounced asymmetry, which depends on the background count rate: the bottom left half of the distribution is much less affected by false coincidences than the top right half. This indicates that the two-electron distribution for positive ion momenta is more reliable than for negative ion momenta. In particular, the signal in the top right (first) quadrant is reduced in favor of the signal in the right halves of the top left (second) and bottom right (fourth) quadrants, as indicated by the arrows in the top right panel of figure 3.8.

The differently strong impact of false coincidences in the two halves can be understood as follows. First, recall that it is a-priori unknown whether an electron detected in coincidence with a doubly charged ion actually originates from this ion or not. For the generation of the correlation spectra, the electron with the shortest time-of-flight, corresponding to the smallest (or highest negative) momentum is selected. Whether the selected electron is an NSDI electron or not can be understood as a competition for the shortest electron time of flight between the distributions of NSDI and background electrons. Because the majority of the background electrons originate from single ionization, the momentum spectrum of singly-charged ions, originating from ATI, represents a good approximation for the momentum distribution of background electrons. The momentum spectra of NSDI and ATI electrons are shown in figure 3.9 for an experiment using Ar as target gas. The momentum distribution of electrons detected in coincidence with an Ar^{2+} ion with $p_i > 0$ is centered around a negative value (corresponding to short TOF). Hence, for an Ar^{2+} ion with $p_i > 0$ it is unlikely that background electrons, whose distribution is centered around zero, are detected before the first NSDI electron. For an Ar^{2+} ion with $p_i < 0$, however,

the situation is the opposite. Because the corresponding electron distribution has a positive mean value, an ATI electron, if existent, is likely to be detected before an NSDI electron. Thus, the false coincidences resulting from the selection of ATI electrons instead of NSDI electrons have a much stronger impact on the top right half than on the bottom left half of the correlation spectrum.

As can be seen in figure 3.8, the bottom left hemispheres of the spectra are relatively undistorted, even for rates approaching 1 electron per shot. Hence, one may restrict the analysis to their bottom left half and exploit the symmetry properties of the correlation spectra to gain the top right half.

Because the asymmetry between the first and third quadrants is strongly dependent on the background rate, this asymmetry can be used as a qualitative measure for the electron rate. A relatively symmetric diagram is an indication of a low impact of false coincidences, which represents favorable experimental conditions for the measurement of clean electron-ion coincidences.

3.5. Intensity determination

Two different methods of intensity determination are employed in this work. The first method is purely experimental. The second method relies on fitting the measured Ar^+ momentum spectrum along the laser polarization with a calculated spectrum. Both methods are described below

For purely experimental intensity determination, the characteristic $2\,U_P$ or $10\,U_P$-cutoffs can be employed. When using few-cycle pulses, additional information can be inferred from the CEP-dependent features of the ATI spectra. In the photoelectron momentum spectrum and asymmetry map shown in figure 3.10, such features can be identified. At small longitudinal momenta along the laser polarization, here $p < 1\,\mathrm{a.u.}$, a few shoulders can be identified in the spectrum. These shoulders correspond to pronounced fringes in the asymmetry map. At the direct-electron cut-off near $p = 1\,\mathrm{a.u.}$, the Ar^+ yield begins to decline rapidly. In this range, a region of very high asymmetry is present, which is followed by a minimum in the asymmetry at slightly higher momenta. Above $p = 1\,\mathrm{a.u.}$, the regions of preferential left- and right-emission start to be clearly tilted in the asymmetry map. This "CEP-chirp" is characteristic for electron recollision and the rescattering plateau of ATI electrons, where the asymmetry amplitude rises up to nearly ± 1 in the near-single cycle regime.

Importantly, a few of the features mentioned above are functions of the intensity and can be used for its determination. In particular, this applies to the strong asymmetry maximum before the onset of the ATI plateau. By assuming the maximum of the asymmetry as $2\,U_P$, the intensity can be obtained using the definition of U_P (equation 2.6). The interpretation of the local asymmetry maximum as $p = 2\sqrt{U_P}$ is consistent with the marked position of the high-energy cut-off of approximately $10\,U_P$. Furthermore, a similar drop of the electron yield as observed here at $p = 1\,\mathrm{a.u.}$, has been previously interpreted as the $2U_p$ cut-off [63].

In practice, the intensity determination is performed as follows. As shown in figure 3.10(b), the asymmetry amplitude $A(p)$ is plotted as a function of p. The position of the local maximum just before the onset of the ATI plateau, is determined by fitting a Gaussian to $A(p)$ in this region. Due to the typically good statistics of the Ar^+ data, the determination of the asymmetry maxima can be done with an uncertainty lower than 3%. However, the absolute intensity determination

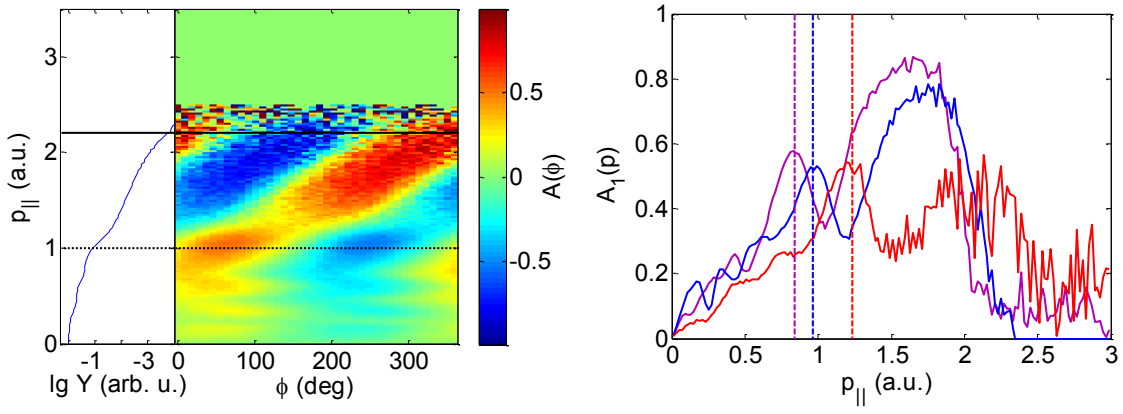

Figure 3.10.: (a) Asymmetry map for the longitudinal momenta of Ar^+ ions generated with laser parameters $\tau = 4\,\mathrm{fs}$, $\lambda = 750\,\mathrm{nm}$, and approximately $I = 1.2 \times 10^{14}\,\mathrm{Wcm^{-2}}$. The dotted and solid lines mark the local asymmetry maximum and the high-energy cut-off, respectively. (b) Dependence of the asymmetry amplitude on the Ar^+ momentum along the laser polarization for different laser intensities. The pulse duration was approximately $4\,\mathrm{fs}$ but may slightly differ for different measurements. For each curve, the dashed line marks the local maximum in the asymmetry. By assuming that the local asymmetry maxima correspond to $p = 2\sqrt{U_P}$, the intensities 0.9, 1.2, and $2.0 \times 10^{14}\,\mathrm{Wcm^{-2}}$ are retrieved.

from these values relies on the correctness of the underlying assumption that the position of the local asymmetry maximum indeed corresponds to $2\,U_P$. Nevertheless, the method is very useful to determine the relative intensity changes between different experiments. The good statistics of the Ar^+ data further enables us to keep track of intensity drifts during the experiment by monitoring the widths of the measured momentum spectra.

The second method used for intensity determination relies on Ar^+ spectra calculated using the ionization rate from Ref.[28] and the simple man's model (see section 2.2). An illustration of this method is given in figure 3.11(a). The measured Ar^+ momentum spectra along the laser polarization are fitted with predicted ones. The intensity value obtained by this fit is used for the calculation of NSDI spectra. We estimate the precision of the intensity calibration to about 20%.

In figure 3.11(b), a predicted Ar^+ asymmetry map is displayed. A comparison to the experimental data in figure 3.10(a) shows that besides the agreement in the FWHM of the momentum distribution, the magnitude of the predicted CEP-dependent asymmetry is consistent with the measured one. In particular, the predicted asymmetry map agrees with the experimental observations regarding the maximum in the asymmetry amplitude near $p = 1\,\mathrm{a.u.}$ and the subsequent minimum in the asymmetry. However, the simulated high-energy cut-off disagrees with the measured one. While the measured electron yield cuts off at approximately $p = 2.2\,\mathrm{a.u.}$, the electron momenta extend up to $p = 3.1\,\mathrm{a.u.}$ in the simulated spectrum . For the laser parameters $\lambda = 750\,\mathrm{nm}$, and $I = 2.8 \times 10^{14}\,\mathrm{Wcm^{-2}}$, the local asymmetry maximum at $p = 1\,\mathrm{a.u.}$ and the

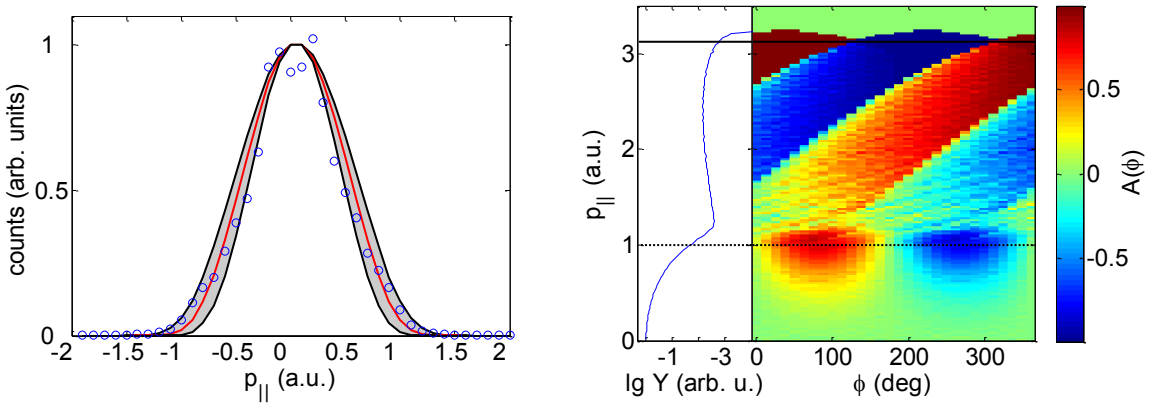

Figure 3.11.: Intensity determination using the model. The measured Ar^+ spectrum (open circles) is plotted together with simulated spectra calculated for three different intensities $3.0 \times 10^{14}\,\mathrm{Wcm^{-2}}$ (red line), $2.4 \times 10^{14}\,\mathrm{Wcm^{-2}}$ and $3.6 \times 10^{14}\,\mathrm{Wcm^{-2}}$ (narrow and wide black spectra, respectively). The gray area in between the two black curves represents the error bars of $\pm 20\%$ in the determination of the peak intensity. (b) Calculated asymmetry map for the Ar^+ momentum along the laser polarization for the intensity $2.8 \times 10^{14}\,\mathrm{Wcm^{-2}}$. In the simulations, a 5% rescattering probability was assumed. The solid and dotted lines mark the positions of the high-energy cut-off at $3.1\,\mathrm{a.u.}$ and the local asymmetry maximum at $1.0\,\mathrm{a.u.}$, respectively.

high-energy cut-off at $p = 3.1\,\mathrm{a.u.}$ correspond to electron energies of approximately $1\,U_P$ and $9\,U_P$[3].

The discrepancy between experiment and theory may have two possible explanations: one explanation would be that the local asymmetry maximum does not correspond to $2\,U_P$ but rather to $1\,U_P$, as indicated by the semi-classical calculations. This would imply that the intensity determined with the first method is underestimated and the $10\,U_P$ cut-off is not visible in the experimental data.

An alternative explanation would be that the semi-classical model predicts an incorrect momentum for the local asymmetry maximum. In that case, the intensity is overestimated by the comparison of the widths of experimental and theoretical Ar^+ spectra.

A detailed experimental and theoretical investigation of intensity and CEP-dependent features in ATI of rare gases using near-single-cycle pulses would be useful in order to clarify the suitability of different approaches for the determination of the laser intensity.

[3]For near-single-cycle pulses, the high-energy cut-off is expected to be slightly smaller than $10\,U_P$.

4. Results I: Single-cycle NSDI

The investigations of NSDI of Ar constitute the central part of this work. In section 4.1, the main results of publication 7.1 are summarized. The summary is supplemented in section 4.2 by a discussion of the role of depletion in the theoretical description of the data. The recollision-excitation with sub-cycle depletion (RESD) mechanism is found to also govern single-cycle NSDI of N_2 in a comparative study of NSDI of Ar and N_2 in publication 7.3. Section 4.3 summarizes these results, which are supplemented by a discussion of the role of the excited state in the RESD simulations in section 4.4. To gain deeper insight into single-cycle NSDI of Ar its intensity dependence has been studied in a series of experiments whose results are discussed in section 4.5. The experimental results are compared to predictions from the semi-classical model and interpreted in terms of RESD. In the final section 4.6, the results of publication 7.4 are summarized: It reports on the experimental investigation of the transition from single-cycle NSDI to many-cycle NSDI of Ar.

4.1. Correlation spectra in the single-cycle limit

Measured two-electron momentum distributions in the single-cycle limit are shown in figure 4.1. When averaging over the CEP, a cross-shaped correlation spectrum is obtained, indicating that one electron momentum is always close to zero while the other one carries the largest fraction of the momentum along the laser polarization. This asymmetric energy sharing of the two electrons is substantially different from earlier experimental results obtained with longer pulses. This strongly suggests that the physical mechanisms that govern NSDI in the near-single-cycle regime differ from the ones in many-cycle regime, where previous experiments were performed.

The strong impact of the CEP on NSDI can be clearly seen in the correlation spectra for fixed CEP. For an adequate CEP value, referred to as $\phi = \phi_0$ (or $\phi = \phi_0 + \pi$), the electron emission is confined to one half of the correlation plot (top right and bottom left diagram in figure 4.1). For the intermediate values, the CEP determines the ratio of the signals in the two halves of the correlation plot. Notably, the two-electron spectra for fixed CEP values are always asymmetric, even for $\phi = \phi_0 + \pi/2$, where the yield in both halves is equal. As discussed in detail in section 4.2, this asymmetry can be understood by how soon after the recollision the ionization of the second electron occurs at different points in time during the near-single-cycle laser pulse.

To gain a deeper understanding of our experimental results we compare them to predictions by the semi-classical model outlined in the methods section of publication 7.1. The cross-shaped correlation spectrum and its CEP dependence are well reproduced assuming recollision-excitation with subsequent ionization. In this NSDI mechanism the recollision of a first ionized electron with its parent ion leads to excitation of the ion which is subsequently ionized by the

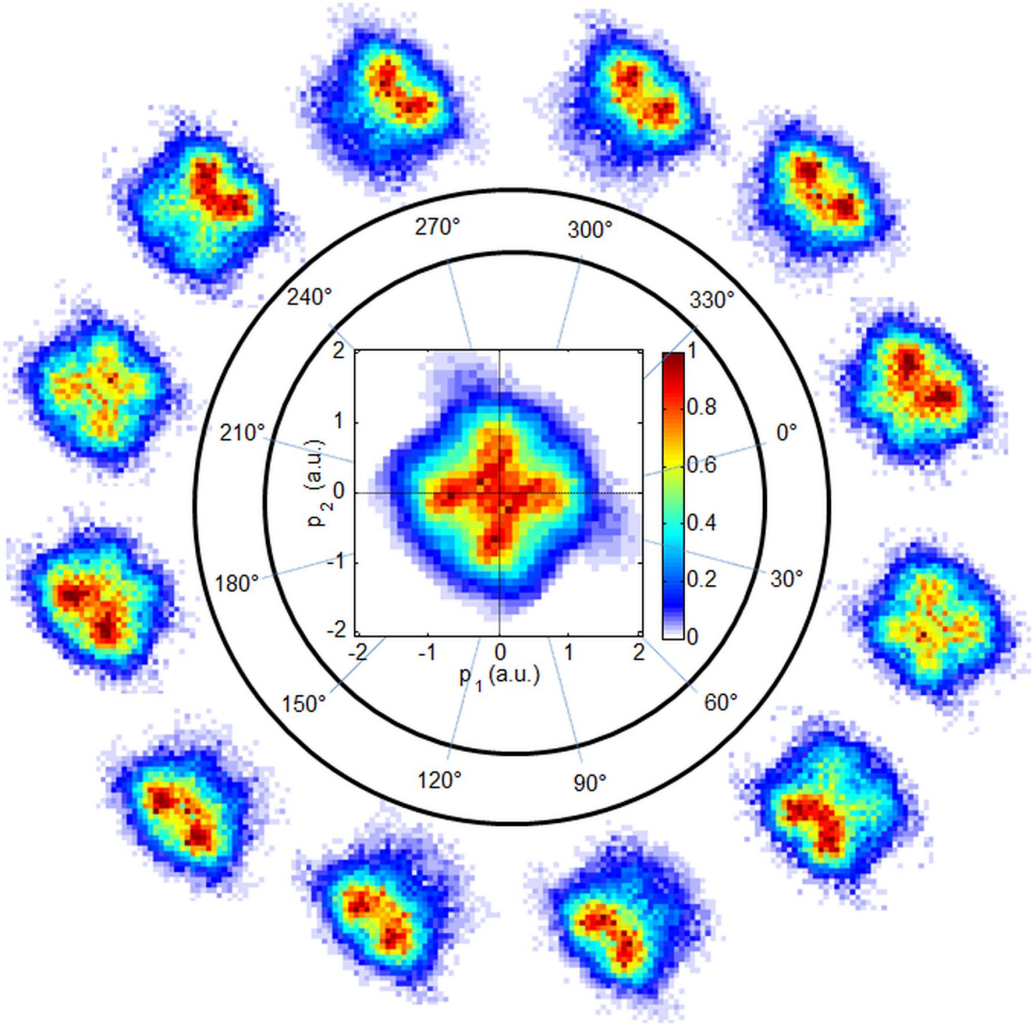

Figure 4.1.: Correlated two-electron momentum distributions for NSDI of Ar in a near-single-cycle laser pulse for different CEP values. The correlation spectrum in the center is averaged over the CEP. The spectra on the outside are each integrated over a CEP range of 30°. As the central diagram, each image displays the NSDI electron yield in the momentum range [-2,2] a.u. for electron and is normalized to its peak value.

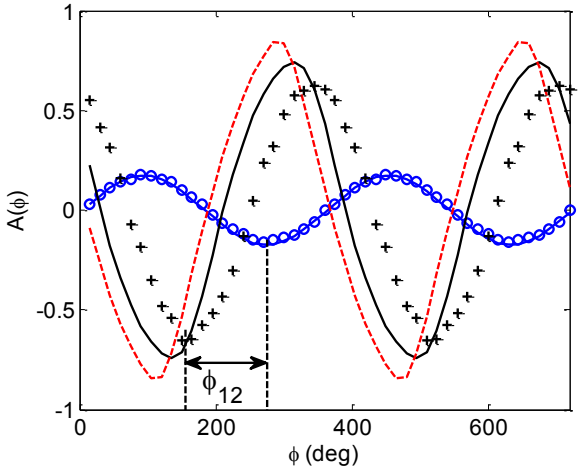

Figure 4.2.: Simultaneously measured CEP-dependent asymmetries in the Ar^+ (blue circles) and Ar^{2+} (black crosses) yields. The experimental results are compared to predictions for the asymmetry in the single ionization (blue line), and double ionization yield assuming recollisional excitation (black solid line) or the (e,2e) mechanism (red dashed line). The measured asymmetry phase shift ϕ_{12} between single ionization and double ionization equals $114°$.

laser field (see section 2.3.2). The analysis of the calculated electron trajectories reveals that depletion of the excited state in the cation, on a time-scale of a quarter optical cycle, plays a crucial role in the formation of the cross-shaped correlation spectrum. Importantly, this sub-cycle depletion causes the second electron to carry a non-zero momentum, while the first electron momentum remains small. Using this result, the most likely emission time of the second electron in the laser pulse can be extracted from the measured correlation spectrum for ϕ=ϕ_0, where only a single recollision contributes to NSDI. We find that the electron emission leads the peak of the field by 210 ± 40 as, which is in good agreement with the predicted value of 230 as.

A particular strength of our experiment lies in the simultaneous measurement of a large number of observables. These include the CEP-dependent asymmetries in the single and double ionization yield. For a comparison of the two, it is useful to introduce the asymmetry parameter A_n, defined in equation 3.3, for the singly ($n = 1$) and doubly ($n = 2$) charged Ar ions. The asymmetry can usually be parametrized as a sinusoidal function of the CEP ϕ,

$$A_n(\phi) = A_n \sin(\phi + \phi_n), \tag{4.1}$$

where A_n is the asymmetry amplitude and ϕ_n is a phase offset. The measured CEP-dependent asymmetries in the Ar^+ and Ar^{2+} yields are displayed in figure 4.2. A phase difference $\phi_{12} = 114°$ is observed between the asymmetry curves for single and double ionization. As shown in section 4.5.3, this value exhibits a pronounced intensity dependence, . It is worth emphasizing that the phase shift, obtained by the simultaneous measurement of different asymmetry data,

represents a new and valuable observable to test the validity of theoretical models.

Despite the good agreement between predicted and measured NSDI spectra, ϕ_{12} is not correctly reproduced. In the RESI simulations ϕ_{12} is overestimated by $40°$. See section 4.5.3 for further information.

4.2. The role of sub-cycle depletion

Depletion of the excited state population is a crucial component of the present NSDI model. According to the classical barrier-suppression intensity (equation 2.2), the saturation threshold depends on both the ionization potential and the ionic charge. For the lowest excited state of Ar^+ with an ionization potential of $14.1\,\mathrm{eV}$, the barrier suppression intensity is only $4 \times 10^{13}\,\mathrm{Wcm^{-2}}$, approximately 6 times lower than for the ground state of the neutral atom ($I_P = 15.76\,\mathrm{eV}$). This comparison is justified because the lowest excited state of Ar^+ ([Ne]$3s^1 3p^6$) has the same degeneracy as the ground state of the neutral atom.

The crucial role of depletion in our model is demonstrated by testing the effect of artificially switching depletion off in the calculations. In that case, the characteristic cross-shape shown in figure 4.3 (a) vanishes and the structureless distribution of panel (b) is obtained.

The connection between depletion and the cross shape can be explained as follows. When the laser intensity is sufficiently high for depletion to be relevant, the ionization yield per unit time is maximal before the electric field reaches its peak value throughout the half-cycle. Since the value of the vector potential is non-zero before the field maximum, the second electron preferentially acquires a non-zero drift momentum. Together with the small drift momentum acquired by the first electron, and averaged over CEP, the cross-shaped correlation spectrum arises.

When depletion is neglected, however, the highest emission probability for the second electron is always reached at the peak of the laser field. At the electric field maximum, the vector potential is zero, which results in the second electron being emitted with zero drift momentum. The consequence is the narrow distribution around the origin of the correlation plot shown in panel (b).

The spectrum shown in figure 4.3 (c) represents an attempt to generate a cross-shape distribution without depletion. Here, the first electron carries large momenta acquired by backscattering ($\beta = 180°$) while the second electron momentum is low. However, the resulting diagram does not exhibit a cross-shape. Because backscattering leads to high electron momenta, the intensity used in the simulation had to be significantly reduced to obtain momenta of the same magnitude as in panels (a) and (b).

The role of depletion can be further examined by inspecting correlation spectra for fixed CEP values. In figure 4.4, precisely two recollisions in subsequent half-cycles result in distinct contributions (1 and 2) in opposite halves of the two-electron distribution. One half is populated by a rather weak signal with large momenta, the other one is populated by a large signal with small momenta. The reason for this difference is the different degrees of depletion in the ionization of the second electron.

The first electron of contribution 1 is emitted early in the pulse, when the field strength is rather weak. Consequently, the yield for this contribution is rather low. After the recollision-

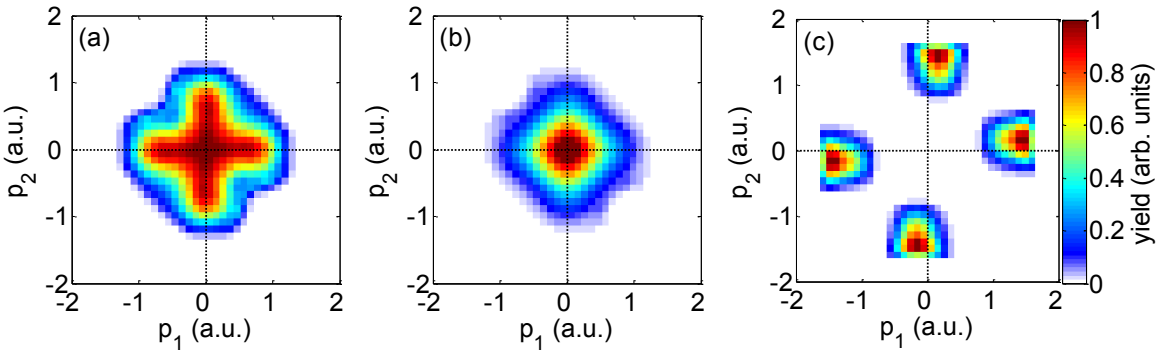

Figure 4.3.: CEP-averaged electron correlation spectrum predicted for Ar with the parameters $I_{\max} = 2.9 \times 10^{14}\mathrm{Wcm}^{-2}$, $\tau = 3.8\,\mathrm{fs}$, $\beta = 20°$ (a) when depletion is considered, (b) when depletion is neglected. In panel (c) the simulation results without depletion are displayed for the intensity $I_{\max} = 1.0 \times 10^{14}\mathrm{Wcm}^{-2}$ and total backscattering, $\beta = 180°$

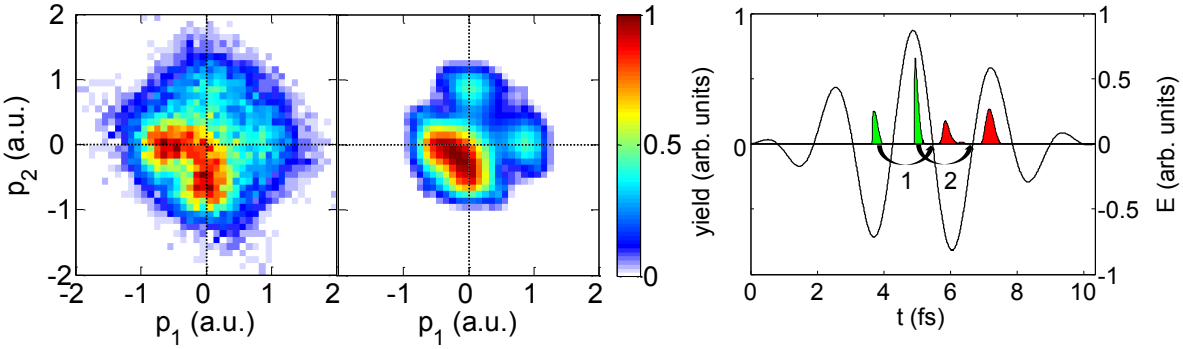

Figure 4.4.: (left) Measured and calculated correlation spectrum for a CEP with zero asymmetry in the ion emission direction. (right) Electric field of the laser pulse and calculated ionization rates for the first (green-filled area) and the second (red-filled area) electron contributing to NSDI of Ar in the laser field (solid line). The numbers 1 and 2 mark the contributions from the two recollisions leading to double ionization. The arrows point to the time of recollision for electrons emitted near the tail of each arrow.

excitation, the excited $Ar^{+}*$ ion is subject to a very strong field that rapidly increases beyond the saturation intensity of the first excited state of Ar^{+}. Therefore, the excited state population is quickly depleted, which causes the second electron to be most likely emitted significantly before the field maximum and thereby acquire a large drift momentum.

Contrary to the situation in contribution 1, the first electron of contribution 2 is emitted near the maximum of the intensity envelope, which leads to a large yield. After the recollision, however, the field strength has decreased, which leads to reduced depletion. Consequently, the second electron is emitted closer to the field maximum and acquires small drift momenta. Because the vector potential has changed its sign with respect to the previous half-cycle, the second electron of contribution 2 is emitted into the opposite direction than the second electron of contribution 1.

In summary, the instantaneous laser intensity determines how strong depletion is, and therefore when the release of the second electron most probably occurs. If depletion is strong, the second electron acquires large drift momenta up to $2\,U_P$. If it is weak, the resulting electron momenta are small. In this sense, the *recollision-excitation with sub-cycle depletion* model has two limits. In the limit of no depletion the structureless distribution of figure 4.3 (b) is obtained which is similar to a distribution expected for sequential double ionization. In the opposite limit of infinite depletion, the electron is emitted at the very time of recollision, which corresponds to the (e,2e) direct impact ionization mechanism when it is assumed that the second electron is born with zero initial momentum[1].

4.3. Nonsequential double ionization of nitrogen

Experiments on strong-field nonsequential double ionization of different atoms and molecules have shown that NSDI exhibits a considerable target-dependence. For the atomic targets He, Ne, and Ar (e.g. [49]) as well as for the diatomic molecules N_2 and O_2 [52], differences in the correlated two-electron momentum distributions were traced back to the electronic structure of the targets. Our observation of strongly altered double ionization behavior of Ar in the near-single-cycle regime as compared to the multi-cycle regime has triggered interest in comparative studies on different targets.

An ideal test case for a comparison to Ar is its companion molecule N_2. The first and second ionization potentials of Ar (15.8 eV and 27.6 eV) and N_2 (15.6 eV and 27.1 eV) are nearly identical and similarities with respect to strong-field ionization and particularly multi-cycle NSDI have been reported, e.g. [64, 65]. However, as shown in the previous sections, double ionization of Ar does not only depend on the ionization potentials but also involves electron excitation in the cation. An inspection of the electronic state spectra of Ar^{+} and N_2^{+}, reveals substantial differences for the two species. In particular, the lowest-excited state of Ar^{+} with an excitation energy of 13.5 eV bridges approximately half of the second ionization potential, whereas N_2^{+} has several excited states below 13 eV [66].

In order to directly compare the CEP-dependent momentum spectra of singly and doubly-charged Ar and N_2 ions, both gases were exposed to the same laser focus within the REMI. The

[1] An example for a two-electron distribution generated by the (e,2e) process is given in figure 6 of publication 7.1.

partial Ar and N_2 pressures in the gas jet were adjusted during the experiment, such that the number of detected doubly-charged ions for both species was approximately equal at all times throughout the entire 69 hours of the experiment. As outlined in publication 7.3, the results of this experiment show that the CEP-resolved ion momentum spectra for Ar^{2+} and N_2^{2+} closely agree in their shape and are in phase with each other.

In order to record two-electron momentum spectra for NSDI of Ar and N_2, two separate experiments with very similar conditions were conducted. The results are displayed in figure 4.5, together with calculated spectra for Ar and results of adapted calculations for N_2, described below. The very close resemblance of the single-cycle NSDI spectra measured for the two species suggests that the same double ionization mechanism should apply for Ar and N_2. However, by close examination of the NSDI spectra of the two targets, a number of differences can be identified. In particular, the CEP-averaged correlation spectrum for N_2 contains a small contribution of low-energy anti-correlated electrons not present in the correlation spectrum for Ar.

Because of the close similarities of the first and second ionization potentials for Ar and N_2, the origin of the observed differences should be the different excited state spectra of Ar^+ and N_2^+. The essential difference between the excited state spectra of Ar^+ and N_2^+ are the low-lying states present in N_2^+ but absent in Ar^+. To explore their influence on the predicted correlation spectra RESD calculations for various values of the excitation energy were performed. The results presented in section 4.4 demonstrate that the shape of the correlation spectrum is significantly altered when the excitation energy is changed.

In particular, as discussed in detail in publication 7.3, incorporating RESD via lower-lying excited states as a correction to the simulations for Ar qualitatively accounts for all observed differences in the NSDI dynamics of Ar and N_2. The CEP-dependent correlation spectra predicted by the adapted model including the low-lying excited states, are displayed in the bottom row of 4.5. On the basis of this good qualitative agreement it can be concluded that RESD represents a valid description of single-cycle NSDI of N_2 at the present laser parameters.

4.4. Influence of the excited-state ionization potential

According to the barrier-suppression intensity (equation 2.2), the degree of depletion in the ionization of an atom should depend strongly on the atom's ionization potential. In our model, we have tested the dependence of the calculated correlation spectra on the ionization energy of the excited state of the cation. In figure 4.6 the predicted correlation spectra for NSDI of Ar via fictional Ar^+ excited states with energies between 9.5 eV to 17.5 eV above the ground state are displayed. Clearly, the width of the distribution increases for decreasing ionization energy of the excited state. Furthermore, the main contribution migrates from the origin of the plot towards the extremities of the cross-shape. Both effects can be well explained by sub-cycle depletion. At small excitation energies, the degree of depletion is low, and the spectrum is similar to 4.3 (b), where depletion is entirely neglected. When the ionization energy is reduced, depletion becomes stronger and sets in sooner in the laser half-cycle. Therefore, the second electron is emitted earlier and acquires higher momenta. It can be argued along the same lines as in the discussion of the role of depletion in section 4.2: recollision-ionization represents the limit of recollision-

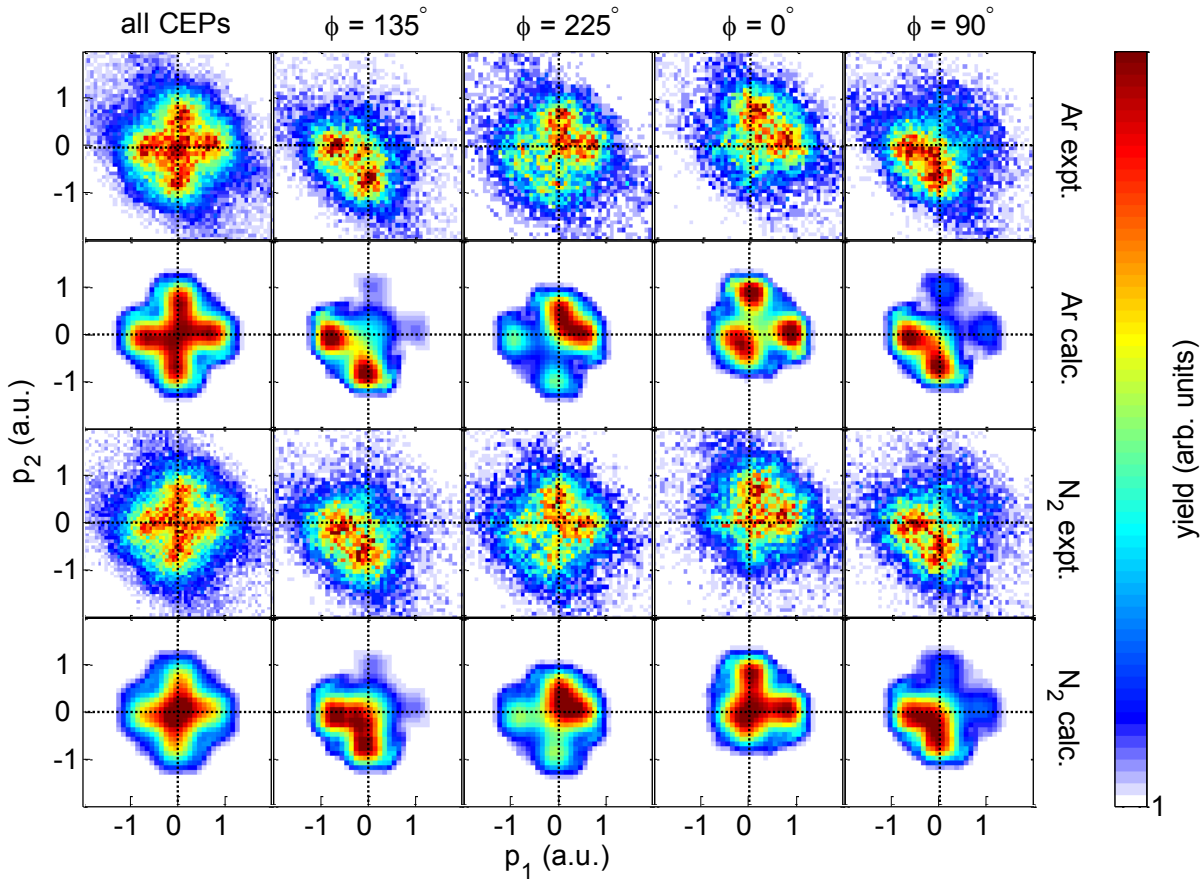

Figure 4.5.: Correlated two-electron momentum spectra measured for NSDI of Ar (top row) and N_2 (third row) and the corresponding predictions for Ar (second row) at the peak intensity $I_0 = 3.2 \times 10^{14}\,\mathrm{Wcm^{-2}}$. In the bottom row, predictions by an adapted version of the semi-classical model, which includes low-lying excited states, are displayed. The CEP-averaged results are shown in the left column. In the second through fifths columns the correlation spectra are presented for the given CEP values.

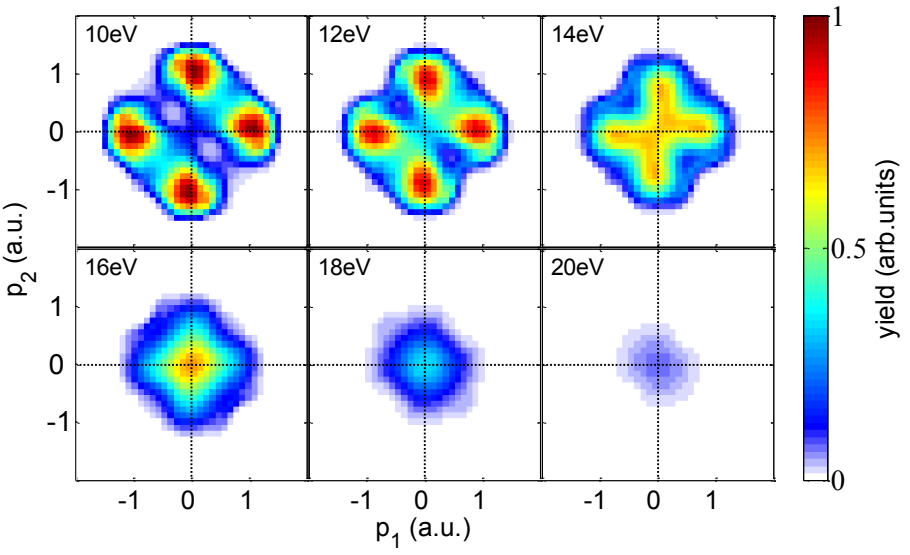

Figure 4.6.: Calculated two-electron momentum distributions for RESD of Ar via different, fictional states of different ionization potential, as indicated in the figure. The parameters used for the simulations were $I_{\max} = 3.2 \times 10^{14}\,\mathrm{Wcm}^{-2}$ and $\tau = 3.8\,\mathrm{fs}$. All images are normalized to the maximum yield in the first figure.

excitation in the case of excitation to a (near-) continuum state. Excitation by very low energies, however, does not provide significant advantage over ionization from the ground state and results in very similar correlation spectra.

4.5. Intensity dependence

In this section, the intensity dependence of single-cycle NSDI of Ar is investigated. In the first part, the ion momentum spectra along the laser polarization are analyzed. The correlated two-electron momentum spectra are discussed in the second part. In the third part, CEP dependencies in the directional and total NSDI yields are investigated. The experimental results are compared to predictions by the semi-classical model.

4.5.1. Ion momentum spectra

Experimental results in the multi-cycle regime, such as the one reported in [50], have shown that the depth of the characteristic double hump in the recoil ion momentum distribution of NSDI of Ar increases with intensity. Our results obtained in the near-single-cycle regime and presented in figure 4.7, make no exception to this rule. The double hump structure has been interpreted as a manifestation of the (e,2e) mechanism [2].According to this interpretation, the intensity

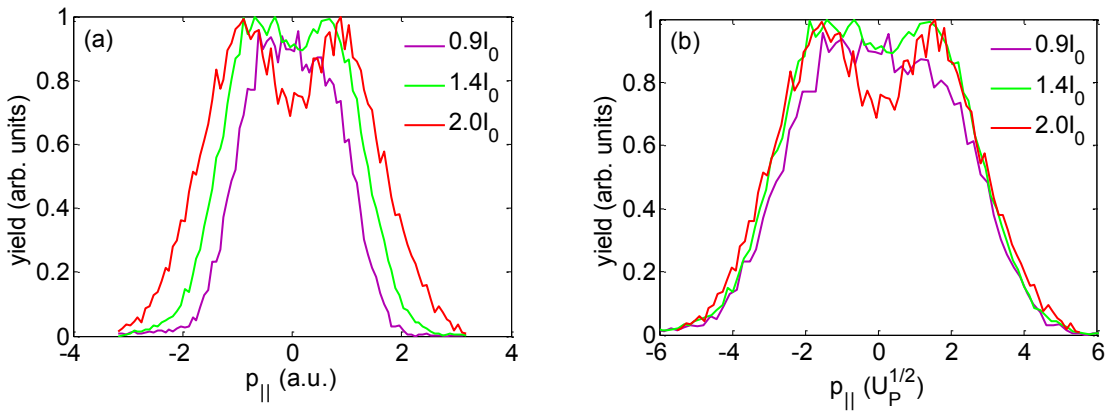

Figure 4.7.: Measured Ar^{2+} recoil momentum distributions along the laser polarization for intensities $0.90I_0$ (purple), $1.4I_0$ (green) and $2.0I_0$ (red), with $I_0 = 10^{14}\,\mathrm{Wcm^{-2}}$ in a.u. (a) and in units of $\sqrt{U_P}$ (b).

dependence of the double hump can be understood as originating from the fact that higher intensities favor (e,2e) recollisions over RESI. In contrast to the assumption that recollision-excitation produces a singly-peaked ion momentum distribution, we have shown in publication 7.1 that recollision-excitation with sub-cycle depletion alone can account for the double hump structure. Within the framework of our model, the enhancement of the double peak comes from the fact that the degree of depletion increases with intensity. This causes the second electron to be emitted earlier within the pulse and thus acquire higher mean momentum (see discussion in section 4.2), reducing the signal at zero ion momentum.

Besides the depth of the double hump, also the width of the ion momentum spectra along the laser polarization are known to depend on intensity. The momentum distribution of the doubly-charged ion is expected to exhibit a cut-off at $p = 4\sqrt{U_P}$, because, without rescattering, each electron involved in double ionization may acquire a momentum of up to $2\sqrt{U_P}$ from the acceleration in the laser field. Indeed, scaling the measured Ar^{2+} momenta with $\sqrt{U_P}$ leads to spectra of nearly-identical widths, as shown in figure 4.7(b). The spectra, scaled in units of $\sqrt{U_p}$, only significantly differ by the depth of the double hump.

4.5.2. Two-electron momentum spectra

The correlated two-electron momentum spectra allow investigating the individual electron momenta that are inaccessible in the ion momentum distributions. Single-cycle NSDI spectra of Ar measured in the intensity range[2] from 0.9 to $2.0\times10^{14}\,\mathrm{Wcm^{-2}}$ are displayed in figure 4.8. As can be seen, changing the intensity is accompanied by qualitative changes in the correlation spectra. Starting from the cross shape of panels (b) and (c), the signal near the origin of the two-electron

[2]The experimental intensity is determined from the $2\,U_P$ cut-offs in the measured single-ionization photoelectron spectra, as identified from the Ar^+ asymmetry map. See section 3.5 for details.

spectrum is enhanced at the expense of the extremities of the cross when the intensity is reduced. For increasing intensity, the extremities of the cross extend to higher momenta and become more densely populated. While at the lower intensities, the spectra are nearly symmetric in all four quadrants, this symmetry is lost at higher intensities, where a clear trend towards correlated electron emission arises: the electron carrying near-zero momentum at lower intensity now acquires a finite momentum pointing in the same direction as the momentum of the fast electron.

Besides this trend towards correlated electron emission, a small signal of strongly correlated electrons emerges outside the cross-patterns in the top right and bottom left quadrants of panels (e) and (f). This is the region expected to be populated by NSDI via electron impact ionization.

When the intensity is slightly further increased such that the distribution shown in figure 4.10 (a) is obtained, a trend that is also present in figure 4.8 becomes very clear: local maxima in the electron yield along the extremities of the cross emerge. For a quantitative comparison, lineouts of the signal in the correlation spectra along the p_1 momentum axis are given in figure 4.10 (b). For the higher intensities, the emergence of an extra peak is clearly seen. This feature is discussed below in terms of recollisional excitation with sub-cycle depletion.

Calculated two-electron spectra corresponding to the experimental results of figure 4.8 are displayed in figure 4.9. The intensity for the simulations was determined by fitting predicted Ar^+ spectra to the measured ones (see section 3.5 for details). As can be seen, the experimentally observed intensity-dependence of the correlation spectra is qualitatively well reproduced by the model. In particular, the signal concentrates toward the origin of the correlation spectrum at low intensities and local maxima emerge on the extremities of the cross-shapes for high intensities. This behavior is a consequence of depletion: when the intensity is increased, the emission of the second electron occurs earlier, which results in a higher momentum. In particular, the larger the separation of the preferential emission time from the peak of the field, the clearer is the separation of the maximum on the momentum axis from the origin of the correlation spectrum. Thus, the local maxima on the extremities of the cross become more pronounced at high intensities.

In order to reproduce the observed distortion of the cross towards positively-correlated electron emission for increasing intensity, the scattering angle β has to be adjusted from 20 degrees for low intensities to 35 degrees for the highest intensity in the range covered in figure 4.9. Increasing β results in a loss of momentum along the laser polarization of the first electron in the recollision. Instead of scattering, excitation of higher-excited states could also result in such a momentum loss. As discussed in section 4.4, the contribution expected from such high-lying states would further enhance the signal on the extremities of the cross.

Despite the good agreement between calculated and measured spectra, the simulations underestimate the yield near the origin of the correlation spectra at the higher intensities (figure 4.8 (e) and (f)). In principle, this signal could be explained by contributions from lower-lying excited states, as the analysis in section 4.4 demonstrates. An alternative explanation would be small contributions from sequential double ionization, which produces a narrow signal around the origin of the correlation plot (cf. figure 4.3 (b)).

The additional contribution of strongly-correlated fast electrons in the experimental data at high intensity (figure 4.8 (f)) is not predicted by recollision-excitation mechanism alone. This signal could originate from higher excited states or the (e,2e) mechanism. While contributions of different states and (e,2e) can be easily added to the simulated NSDI yield, their relative

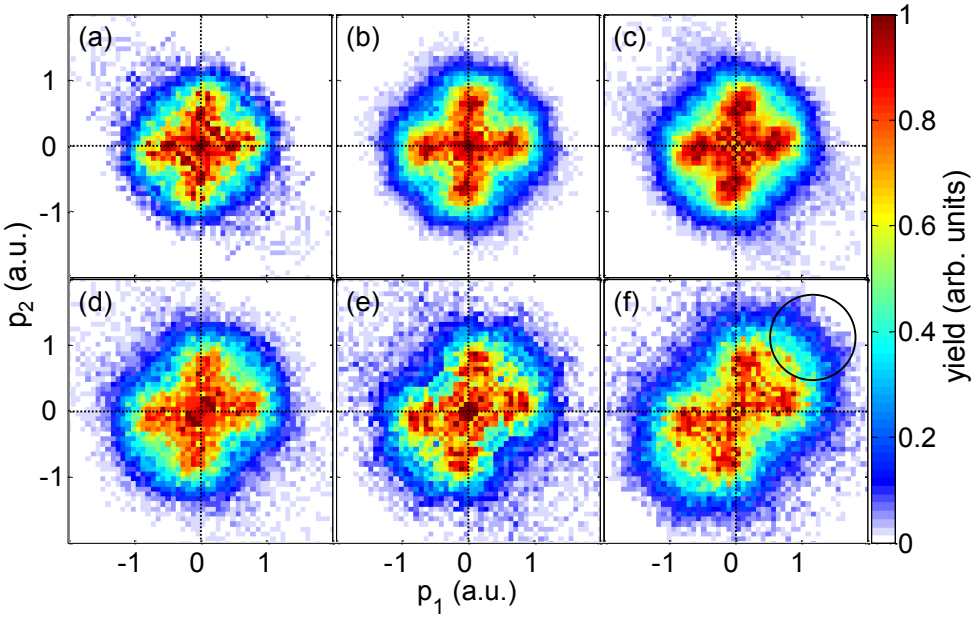

Figure 4.8.: Measured two-electron momentum distributions for NSDI of Ar in near-single cycle laser fields of different intensities, and averaged over CEP. The experimentally determined intensities are (a through f) $[0.9, 1.2, 1.3, 1.4, 1.5, 2.0] \times 10^{14}\mathrm{Wcm}^{-2}$, respectively. The circle in panel (f) marks the small signal of strongly correlated electron emission emerging at high intensities.

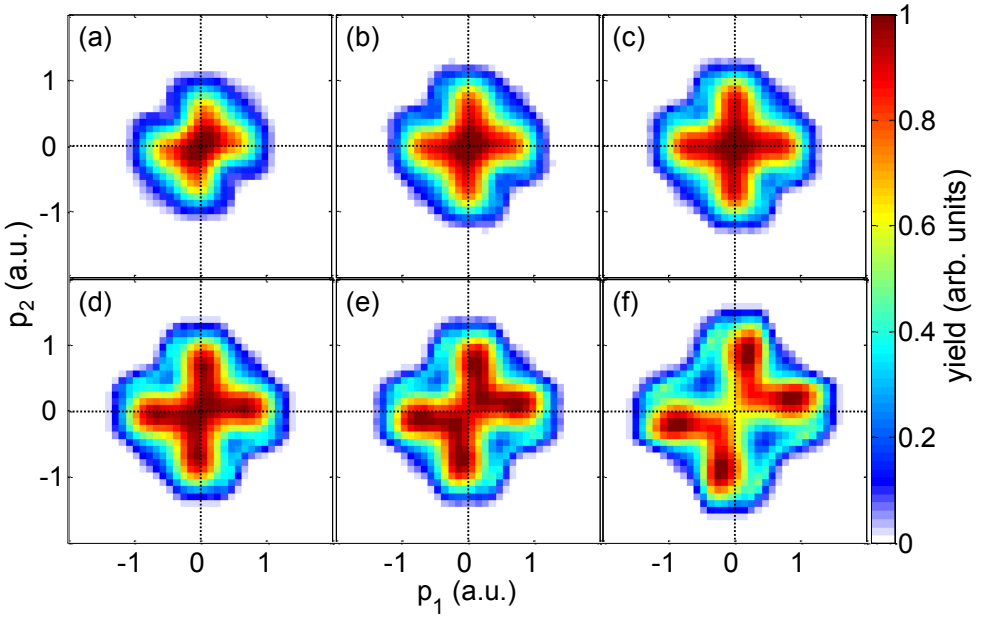

Figure 4.9.: Calculated two-electron momentum distributions for NSDI of Ar with 3.8-fs pulses of intensities (a through f) $[2.4, 2.8, 3.0, 3.2, 3.4, 4.0] \times 10^{14}\mathrm{Wcm}^{-2}$, respectively, and averaged over CEP. The scattering angle β is $[20°, 20°, 20°, 25°, 30°, 35°]$, respectively.

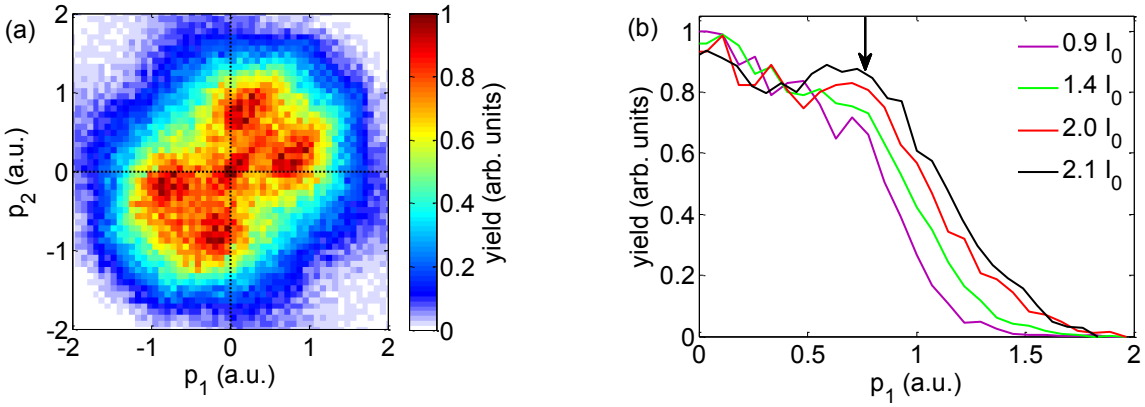

Figure 4.10.: (a) Measured correlation spectrum at approximately $I = 2.1 \times 10^{14}\,\mathrm{Wcm^{-2}}$, and $\tau \approx 5\,\mathrm{fs}$. (b) Momentum distribution of one electron from the double ionization of Ar under the condition that the magnitude of the other electron momentum along the laser polarization is $|p_2| < 0.5\,\mathrm{a.u.}$, for the correlation spectra in figure 4.8 (a, purple, d, green, and f, red). The black curve corresponds to figure 4.10 (a). The arrow marks the local maximum in the electron yield.

contributions are not known. A possible route to calculate the relevant cross-sections would be Quantitative Rescattering Theory [67]. This theory predicts that the share taken by the (e,2e) mechanism increases with intensity but recollisional excitation remains the dominant mechanism for NSDI of Ar at any intensity [68].

4.5.3. CEP-dependence

The CEP dependence of NSDI can be analyzed well on the basis of the CEP-resolved Ar^{2+} recoil ion momentum spectra shown in figure 4.11. The signal in these spectra forms ”islands” of ion emission. For some CEP values, the ions are emitted only in one direction, which is equivalent to only one half of the correlation spectrum being populated. When increasing the intensity, the islands tend to become “longer” along the CEP axis, i.e. the separation between the islands on either side is reduced. In other words, the confinement of NSDI to a single recollision event is incrementally lost for increasing intensity. The spectrum shown in panel (e) represents an exception to this rule, which is probably due to a slightly shorter pulse duration in this particular measurement compared to the other measurements.

The islands in the spectra shown in figure 4.11 exhibit a tilt with respect to the momentum axis. The magnitude of the momenta increases along the CEP-axis well beyond the point of maximum confinement of the ion emission to either side. When comparing the spectra for different intensities, the slope of the tilt appears to increase with intensity.

Furthermore, it can be seen that for increasing intensity the islands in the CEP-resolved momentum spectrum migrate to the left. This indicates that the phase difference ϕ_{12} (see figure 4.2 and equation 4.1) between the CEP-dependent asymmetries in the Ar^{2+} and Ar^{+} emission

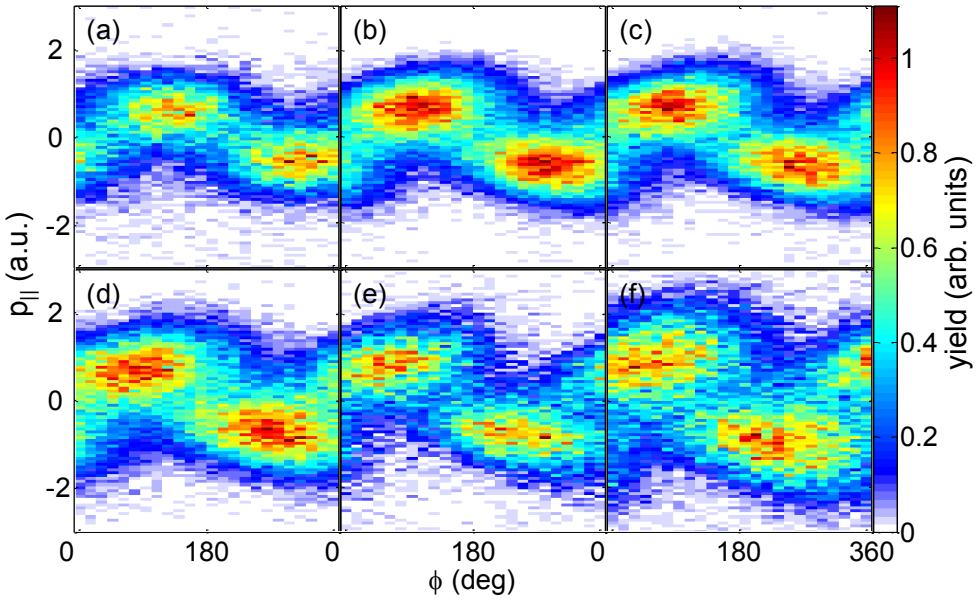

Figure 4.11.: Measured CEP-resolved momentum distributions of Ar^{2+} ions generated in near-single cycle laser fields of intensities (a through f) $[0.9, 1.2, 1.3, 1.4, 1.5, 2.0] \times 10^{14}\mathrm{Wcm}^{-2}$, respectively. The CEP axis displays the phase difference between the CEP-dependent Ar^2+ and Ar^+ asymmetries.

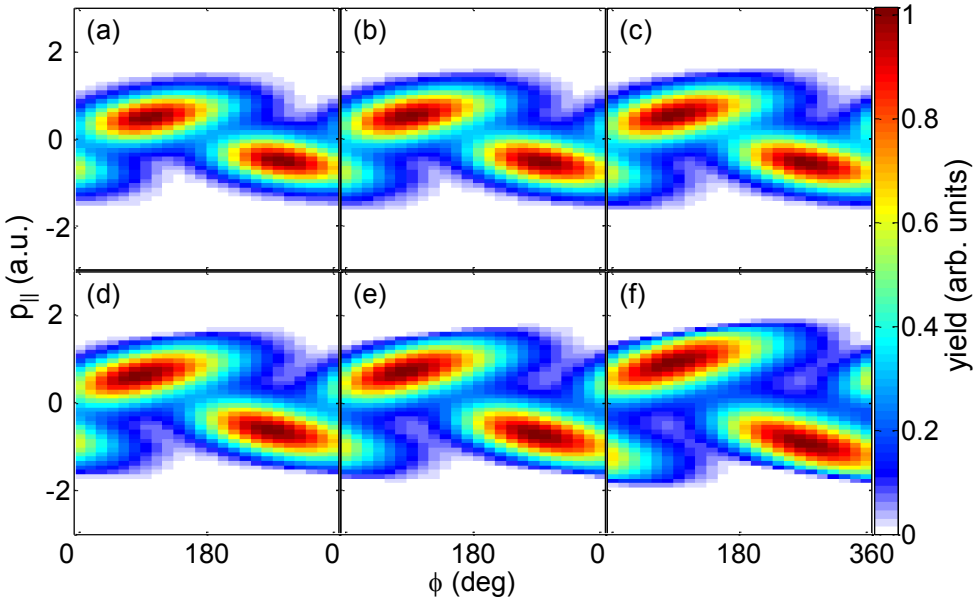

Figure 4.12.: Calculated CEP-resolved momentum distributions for Ar^{2+} ions generated via recollision-excitation with sub-cycle depletion in 3.8-fs pulses of intensities (a through f) $[2.4, 2.8, 3.0, 3.2, 3.4, 4.0] \times 10^{14}\mathrm{Wcm}^{-2}$.

exhibits a pronounced intensity dependence. Note that the intensity dependence of ϕ_{12} might also originate from an intensity dependence of the CEP-dependent Ar^+ asymmetry. Recent experimental and theoretical results [69] indicate that such a dependence, though weak, indeed exists.

For interpretation of the observed intensity dependence, the experimental results of figure 4.11 are compared to spectra predicted by the RESD model, which are displayed in figure 4.12. Despite a slight underestimation of the widths of the spectra[3], the predicted spectra agree well with the measured ones. In particular, the three major trends with rising intensity, (i) reduced confinement of the ion emission to a single recollision, (ii) tilt of the islands, and (iii) phase-shift between single and double ionization, are qualitatively correctly reproduced.

The good agreement between measured and predicted spectra allows us to discuss the underlying mechanisms causing the intensity-dependent trends. The reduction of the single-recollision confinement with increasing intensity is expected due to the recollision energy required for triggering double ionization via excitation of the parent ion. At higher intensities, two sufficiently-energetic recollisions in subsequent half-cycles of the laser pulse are achieved in broader CEP ranges than at low intensities. Thus, the contrast between the double ionization yield caused by two subsequent recollisions is reduced when the intensity is increased.

The tilt of the islands with respect to the CEP axis can be understood as follows. Let us consider a CEP for which the ion emission is confined to either positive or negative momenta and only a single recollision is contributing to NSDI. In that case, the first electron is emitted in the half-cycle just before the peak of the envelope and the second electron is emitted in the half-cycle just after (see figure 3 of publication 7.1). When the CEP is changed to larger values, the second electron is born in a stronger field and, due to the increased degree of depletion, the emission time changes to earlier values. Consequently, the second electron acquires a larger momentum. This is equivalent to an increased ion momentum, when neglecting the small momentum of the first electron. Hence, the mean ion momenta increase with CEP, corresponding to a tilt in the CEP-resolved momentum spectra. In contrast to the field ionizing the second electron, the field ionizing the first electron decreases when the CEP is increased. This leads to the decreasing ion yield along the CEP axis up to the point where a second recollision contributes efficiently to NSDI.

In order to discuss the intensity dependence of the phase shift of the Ar^{2+} asymmetry, a 1D representation of this effect is useful. In figure 4.13 the phase difference ϕ_{12} is plotted as a function of the intensity obtained by fitting the measured Ar^+ spectra with calculated ones. The slopes of the calculated results given in figure 4.13 agree fairly well with that of the experimental results. However, a substantial discrepancy of approximately 40° remains over the entire intensity range. This mismatch will be discussed below.

What is the cause of the intensity-dependence of the phase shift ϕ_{12}? The recollision can be expected to introduce an intensity dependence due to the "CEP-chirp" in the energy distribution of recollision electrons described in section 3.5 (cf. figure 3.10) and because only electrons recolliding with a sufficient amount of energy (here 13.5 eV) can trigger double ionization.

[3]The larger width of the experimental Ar^{2+} momentum spectra compared to the calculated ones might be due to the contribution of higher excited states.

Additionally, depletion may introduce a phase shift. This is clearly the case for single ionization. The effect can be understood in terms of the simple-man's model by considering the ionization of neutral atoms by a cosine-like pulse and neglecting the small electron yield through rescattering. When depletion is negligible, the photoelectron spectrum generated by the cosine-like pulse is expected to be left-right symmetric: by definition, the first half of the pulse produces exactly the same ionization rate as the second half. Since the vector potential of a cosine pulse is anti-symmetric, the positive and negative halves of the momentum distribution of the photoelectrons ionized by the cosine-pulse are identical. However, if depletion is significant, the first part of the pulse will ionize a considerable amount of the available atoms, leaving a reduced initial population for the second half of the pulse to ionize. Hence, the resulting photoelectron momentum spectrum is no longer symmetric, leading to a phase shift in the asymmetry, induced by depletion.

Using the calculations, recollision and depletion phase shifts can be disentangled. The light blue dashed line in figure 4.13 represent the calculation results when depletion in the emission of the second electron is neglected. As can be seen, depletion in NSDI only plays a minor role for the intensity-dependence of the Ar^{2+} asymmetries. The role of depletion for the intensity dependence of the phase of the CEP-dependent asymmetry in single ionization, ϕ_1, can be tested in a similar manner. Neglecting depletion in the first ionization step shows that the effect described in the previous paragraph leads to a significant portion of the observed intensity-dependence of ϕ_{12} for intensities above $\approx 3.0 \times 10^{14}\,\mathrm{Wcm}^{-2}$.

Using near-single-cycle pulses, it has been shown that not only the left-right yields but also the *total* double ionization yield depends on the CEP [10, 70]. Due to symmetry reasons, the modulation in the CEP-dependent yield exhibits a periodicity of π. The CEP-dependent yield normalized to its CEP-averaged value can usually be fitted by

$$\bar{Y} = 1 + A_Y \sin(2\phi + \phi_Y), \tag{4.2}$$

where A_Y is the modulation amplitude and ϕ_Y is a CEP offset. It was shown in figure 6 of publication 7.2 that A_Y decreases with increasing laser intensity, which agrees with our semi-classical model and the predictions from Quantitative Rescattering Theory [68]. However, quantitative agreement for the magnitude of A_Y has not been obtained using our model.

The intensity dependence of $\phi_{1Y} = \phi_1 - \phi_Y$ is shown in figure 4.13. As can be seen, ϕ_{1Y} exhibits a similar trend as the phase of the CEP-dependent Ar^{2+} asymmetry. In the lower intensity range, the two curves are parallel, which suggests that the origin of the intensity dependence is the same. At high intensity, however, the trend changes and ϕ_Y and ϕ_2 overlap.

The rather sudden rise of ϕ_Y with increasing intensity is also predicted by theory (cf. figure 4.13). As done before for the asymmetry, the role of depletion, in the ionization of the second electron, for ϕ_{1Y} is elucidated by artificially switching it off in the simulations. The significant difference between the results obtained with and without depletion indicates a strong impact of the effect on ϕ_Y.

Note that the underlying assumptions of the semi-classical model may lead to an incorrect value for ϕ_1 predicted by the semi-classical model. By solving the time-dependent Schrödinger equation for strong-field ionization of atomic hydrogen, Chelkowski *et al.* found theoretically

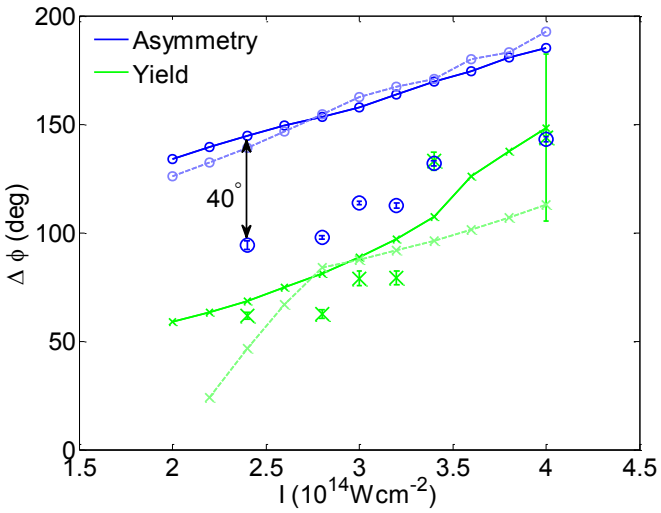

Figure 4.13.: Measured (symbols) and calculated (lines) intensity dependence of the phase of the Ar^{2+} asymmetry and yield. Shown are the phase differences between the Ar^{2+} asymmetry and the Ar^{+} asymmetry, ϕ_{12} (blue), and between the CEP-dependent Ar^{2+} yield and Ar^{+} asymmetry, ϕ_{1Y} (green). The dashed lines in light colors represent the calculated results when depletion is neglected in the ionization of the second electron. The intensity was determined by fitting predicted Ar^{+} momentum spectra to the measured ones. The discrepancy of $40°$ between the predicted and measured values for ϕ_{12} are indicated. The 20% errorbars in the intensity of the experimental data points are omitted for visual convenience.

that the asymmetry assumes a zero value at $\phi_1 \approx -54°$, with only little dependence on the laser intensity [71]. In our simulations we find $\phi_1 \approx 0°$. Provided conclusions for strong-field ionization of Ar can be drawn from the calculations of Ref. [71], the mismatch between the calculated and measured phase of the CEP-dependent asymmetries of double and single ionization is influenced by the disagreement regarding the absolute phase calibration using ϕ_1.

4.5.4. Summary

The results of the studies discussed in this section allow us to summarize the intensity-dependent trends of NSDI of Ar in the single-cycle regime.

For increasing intensity, below the onset of sequential double ionization,

- the Ar^{2+} recoil momentum spectra exhibit an increasingly pronounced double peak structure.
- the width of the Ar^{2+} momentum spectra increases with $\sqrt{U_P}$.

- the signal in the cross-shaped two-electron spectra develops a tendency towards the first and third quadrants corresponding to correlated electron emission.
- in the correlation spectrum, the electron yield along each extremity of the cross-shape develops pronounced local maxima.
- high-energy contributions, ascribed to the (e,2e) mechanism, emerge in the first and third quadrants of the correlation spectra.
- the CEP-range, in which the electron emission is confined to a single recollision, shrinks.
- the phase difference between the CEP-dependent *asymmetries* in the Ar^{2+} and Ar^{+} yields increases.
- the phase difference between the total CEP-dependent of Ar^{2+} *yield* and Ar^{+} *asymmetry* increases.
- the amplitude of the Ar^{2+} *yield* modulation decreases.

As demonstrated in this section, the predictions by the semi-classical model qualitatively agree with the observed intensity-dependent-trends. With the exception of the high-energy contributions, which are ascribed to (e,2e) collisions, all of the effects listed above can be explained within the framework of recollision-excitation with sub-cycle depletion. They originate from the intensity-dependence of the electron recollision energy and, importantly, the increasing degree of depletion of the excited state population with increasing intensity.

While the RESD mechanism represents a valid and comprehensible description of single-cycle NSDI of Ar and N_2 at the investigated laser intensities, the values of the asymmetry phase difference between single ionization and double ionization and the modulation amplitude of the CEP-dependent NSDI yield were not correctly reproduced. For a quantitative agreement, a more sophisticated theoretical description fully accounting for coulomb interaction between the nucleus and all electrons is certainly required. The development of such a description will be hopefully assisted by the highly-differential benchmark data presented in this work.

4.6. Pulse duration dependence

In contrast to previous NSDI experiments in the multi-cycle regime, anti-correlated electron emission is largely suppressed in our experiments on single-cycle NSDI. This strongly suggests that anti-correlated electron emission is caused by multiple recollisions [44, 45] and has motivated us to investigate the intermediate pulse-length regime ($4\,\mathrm{fs} < \tau < 30\,\mathrm{fs}$) for which no kinematically-complete experimental data has been available.

In publication 7.4, we have filled this gap by recording two-electron momentum spectra for pulse durations of 4, 8, 16, and 30 fs. The pulse-duration dependence of the recorded NSDI spectra shown in figure 4.14 is remarkable: increasing the pulse duration from 4 to 8 fs completely changes the shape of the correlation spectrum from a cross to a more or less homogeneous distribution. Doubling the pulse duration again leads to a clear increase in the fraction of

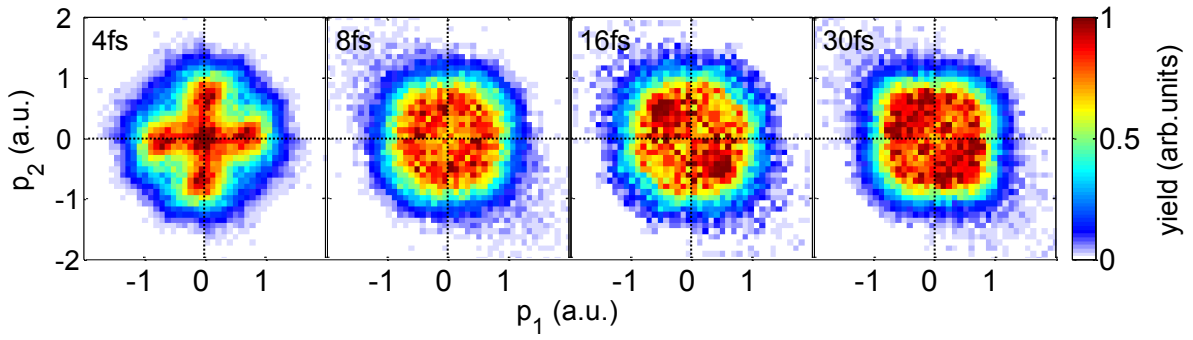

Figure 4.14.: CEP-averaged two-electron momentum spectra for NSDI of Ar with pulses of different durations and an intensity of approximately $1.0 \times 10^{14}\,\mathrm{Wcm}^2$, as indicated in the figures.

anti-correlated electrons. These observations provide strong indication for the involvement of multiple recollisions. Additional data obtained at lower and higher intensities (see publication 7.4) allow us to discuss the combined effects of both pulse-duration and intensity dependence and draw the following conclusions: (i) increasing the pulse duration enhances anti-correlated electron emission and (ii) increasing the intensity enhances positively correlated electron emission. The latter result has been known from previous experiments in the multi-cycle regime [49, 44], and has been generalized here to the few- and single-cycle regime.

Even though the RESD model performs well in the case of single-cycle NSDI, the necessary support for electron trajectories with multiple recollisions would require a large number of additional *ad hoc* assumptions. Such trajectories are naturally supported by fully-classical 3D ensemble calculations which have been successful in producing anti-correlated electrons for multi-cycle pulses, e.g. Ref. [45, 72, 73]. Recently, Huang *et al.* [74] succeeded in accurately describing our single-cycle NSDI experiment from publication 7.1 using a classical ensemble model. This encouriging result indicates that a model yielding a coherent description of NSDI from the single to the many-cycle regime should be within reach. The present data will hopefully contribute to the development of such a model.

5. Results II: Dissociation dynamics of polyatomic molecules in near-single-cycle fields

5.1. Dissociative ionization of laughing gas

Under the clean experimental conditions provided by a single recollision event we have gained new insights into the double ionization dynamics of Ar and N_2. Here, we exploit these conditions for the study of molecular reaction dynamics. In publication 7.5, the dissociative ionization of N_2O by 4-fs pulses has been investigated. N_2O is an asymmetric, linear molecule with an N-N bond length of $1.13\,\text{Å}$ and an N-O bond length of $1.19\,\text{Å}$. It is known from earlier experiments, e.g. [75], that double ionization of N_2O leads to dissociation via two pathways

1. *denitrogenation* $N_2O^{2+} \rightarrow N^+ + NO^+$, and
2. *deoxygenation* $N_2O^{2+} \rightarrow O^+ + N_2^+$.

Recently, Zhou *et al.* demonstrated that the branching ratio of these two channels can be manipulated by varying the time delay in an XUV-IR pump-probe experiment [76]. Kotsina *et al.* [77] showed that the preferential emission direction of N^+ (and NO^+) following double ionization by 40-fs two-color (800 nm and 400 nm) laser pulses can be controlled via the relative phase ϕ of the two colors.

In our experiment, the control of the dissociative ionization of N_2O via the CEP of a near-single-cycle pulse is studied. For the double ionization process, coincidences of N^+ with NO^+ and O^+ with N_2^+ are detected, corresponding to the two dissociation channels given above. By calculating the momentum sum of the two fragments, the dication recoil momentum after double ionization but prior to dissociation can be reconstructed. This capability allows for distinguishing between momenta acquired during ionization and coulomb explosion and thereby enables us to analyze the CEP-dependence of ionization and dissociation independently.

The CEP-resolved spectra of the reconstructed N_2O^{2+} momenta, shown in figure 5.1, are strongly reminiscent of the ones measured for Ar^{2+} or N_2^{2+} (see e.g. publication 7.3. In particular, the momenta of the dication exhibit a strong CEP-dependence with a phase difference between the CEP-dependent asymmetries in the yield of singly- and doubly-charged N_2O ions amounting to $\phi_1 = 120°$. This value matches the phase shift measured in the NSDI experiments on Ar and N_2 (see publications 7.1 and 7.3). This strongly suggests that, at our experimental conditions, double ionization of N_2O is dominantly recollision-induced.

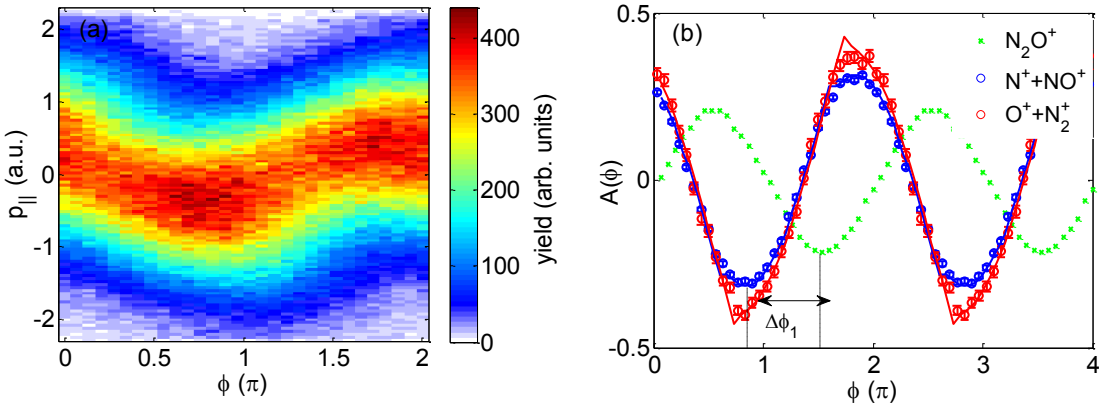

Figure 5.1.: (a) CEP-resolved momentum spectra along the laser polarization for N_2O^{2+}, obtained from the momentum-sum of coincident N^+ and NO^+ fragments (The spectra derived from the deoxygenation channel are almost identical). (b) CEP-dependent asymmetries $A(\phi)$ in the recoil-ion yields along the laser polarization for singly- (green crosses) and doubly-charged (open circles) N_2O ions. The latter are retrieved from the coincidences for the two dissociation pathways, denitrogenation (blue open circles) and deoxygenation (red open circles). The solid lines display predictions from a semi-classical model similar to the one described in publication 7.1. The phase shift $\Delta\phi_1 = 120°$ is indicated.

By reconstructing the dication recoil momenta from both dissociation channels of N_2O^{2+} individually, dications that undergo denitrogenation can be distinguished from those that deoxygenize. Whereas the asymmetry curves for the dications of the two channels are in phase with each other, the amplitude for the deoxygenation asymmetry is slightly larger (see figure 5.1(b)). Semi-classical calculations, similar to the ones described in publication 7.1, suggest that this difference can be explained by the slightly higher energy required to populate the dissociative states leading to deoxygenation.

The above analysis of the CEP-dependent recoil ion momenta provides important information for the interpretation of CEP-dependent asymmetries in the yields of the dissociation products, namely N^+, NO^+, O^+, and N_2^+. Let us first consider the ion yields without coincidence filters. In this case, the dissociation products originate predominantly (with more than 90%) from single ionization of N_2O and subsequent dissociation of the cation. The CEP-dependent asymmetry in the non-coincident N^+ (and N_2^+) ion yield is in phase with the CEP-dependent asymmetry in the N_2O^+ yield. The CEP-dependent asymmetry in the O^+ (and NO^+) ion yield, however, exhibits a phase shift of $180°$ with respect to the N_2O^+ asymmetry. This observation indicates that the CEP-dependent asymmetries in the dissociation product yields following single ionization originate from the orientation-dependence of single ionization. The phase shift of $180°$ between the CEP-dependent asymmetries for N^+ (N_2^+) and O^+ (NO^+) is consistent with this mechanism and the geometry of the molecule.

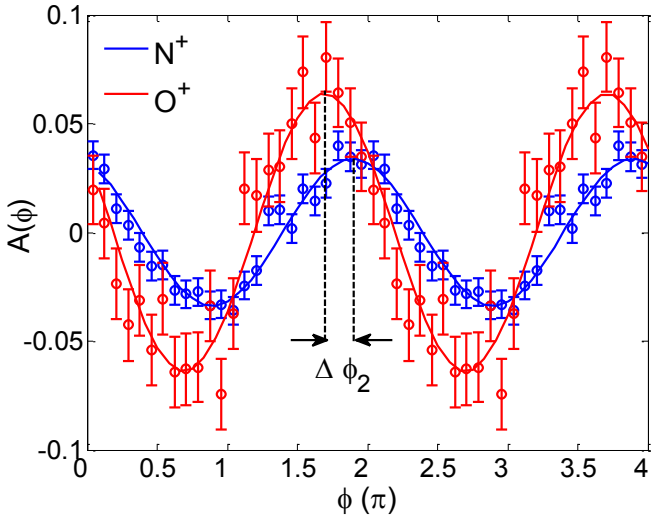

Figure 5.2.: CEP-dependent asymmetries in the deoxygenation (red) and denitrogenation (blue) dissociation pathways of N_2O^{2+}. The asymmetries are calculated from the momenta of the O^+ and N^+ ions detected in coincidence with momentum-matched N_2^+ and NO^+ ions, respectively. The phase shift $\Delta\phi_2$ between the two curves amounts to $(37 \pm 7°)$.

Using coincidence filtering, an exclusive analysis of the denitrogenation and deoxygenation pathways is possible. The CEP-dependent asymmetry in the yield of N^+ ions from the denitrogenation pathway (blue curve in figure 5.2) is in phase with the dication asymmetry curves displayed in figure 5.1. This indicates that, similar to the cause of the asymmetry in the single-ionization fragments, the orientation dependence of the recollision-driven double ionization is responsible for the denitrogenation asymmetry. According to this mechanism, the CEP-dependent asymmetry in the yield of O^+ fragments from the deoxygenation pathway would be expected to exhibit a phase shift of 180° with respect to the CEP-dependent asymmetry in the N^+ yield. As shown in figure 5.2, however, the phase-shift of the CEP-dependent asymmetries of deoxygenation and denitrogenation amounts to only 37°. Hence, the orientation-dependent double ionization is insufficient to explain the CEP-dependence of the deoxygenation channel. Instead, laser-coupling between different electronic states may play a significant role of in the formation of the observed asymmetry. An appropriate modeling of the strongly-coupled electron-nuclear dynamics may shed light on the origin of the observed phase shift.

5.2. Control of hydrocarbon deprotonation

The control of asymmetric ion emission during molecular dissociation via the CEP of a single laser pulse has been reported for asymmetric molecules, such as CO [78] and DCl [79]. Studies

of this phenomenon in symmetric moleules have so far been restricted to molecular hydrogen [23], including its ion [80, 81] (see Ref. [82] for a review of CEP control of molecular dynamics). In the case of H_2 the asymmetry in the ion emission is caused by the coupling of symmetric and asymmetric electronic states. In publication 7.6, we have reported on the *steering* of proton ejection from symmetric acetylene molecules, following double ionization. For C_2H_2, the coupling of symmetric and asymmetric electronic states can be ruled out as the cause of asymmetric deprotonation because the involved electronic states are all symmetric with respect to the proton emission direction. Quantum mechanical calculations indicacte that the experimental findings result from a novel control mechanism involving non-resonant excitation and superposition of vibrational degrees of freedom.

Acetylene is a linear, symmetric molecule consisting of two CH groups connected by a triple C-C bond. After double ionization, the molecular dication may dissociate via several different pathways, including the deprotonation, symmetric dissociation into two CH^+ ions and the isomerization to C-CH_2^{2+} [83]. The depronotation channel is identified by the coincident detection of a proton with a coincident C_2H^+ ion. By calculating the momentum sum of the coincident fragments, the recoil momentum along the laser polarization of the dication prior to deprotonation is reconstructed. The corresponding CEP-resolved momentum spectrum along the laser polarization is displayed in figure 5.3(a) and closely matches the momentum distribution for the recoil momenta of the stable dication (figure 5.3(b)). The CEP-dependent dication momentum spectra are clearly reminiscent of the spectra obtained for NSDI of Ar and N_2, which suggests dication production via recollision-induced ionization.

In Figure 5.3(c), the CEP-resolved momentum spectrum of H^+ fragments, detected in coincidence with C_2H^+ fragments, is shown. Though the CEP-dependence is rather weak, a significant oscillation is visible in the one-dimensional asymmetry curve presented in figure 5.3(d).

In figure 5.3(d), the experimental results are compared to predictions from a quantum mechanical model, developed by the group of Regina de Vivie-Riedle and described in detail in publication 7.6. Conventional mechanisms based on the coupling of symmetric and asymmetric electronic states cannot account for the observed asymmetry since the involved electronic states are symmetric with respect to the deprotonation direction. In the model applied here, only a single electron state in the dication needs to be considered in addition to the the ground states of the neutral and cationic molecule, as shown in figure 5.2(a). The asymmetry in the proton ejection is introduced through the preparation of a vibrational wavepacket and the manipulation of the phases of its components by the laser field.

The deprotonation process of the dication is described in the basis of the symmetric $|0m\rangle$ and anti-symmetric $|n0\rangle$ C-H stretching modes, where m and n are the vibrational quantum numbers of the asymmetric and anti-symmetric stretching modes, respectively. See figure5.3 (b) for an illustration. A linear combination of these modes,

$$|\psi\rangle = \left(1/\sqrt{2}\left(|0m\rangle \pm |n0\rangle\right)\right), \tag{5.1}$$

leads to a wavepacket motion along either one of the C-H stretching coordinates. The negative superposition yields dominant cleavage of the left C-H bond, while the positive superposition yields dominant cleavage of the right C-H bond.

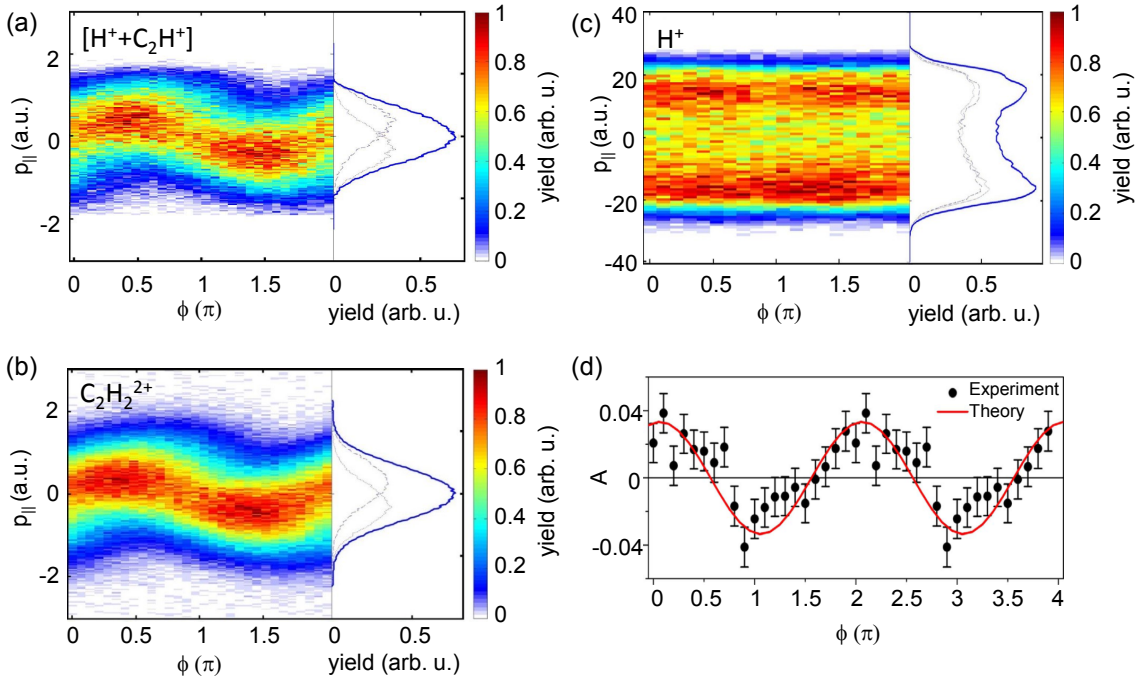

Figure 5.3.: CEP-dependent asymmetries in the dissociative ionization of acetylene. CEP-resolved momentum spectra along the laser polarization of (a) stable dications, (b) the dication prior to deprotonation, (c) H^+ ions emitted from the dication. In the side panels, the CEP-averaged momentum distribution is shown. The dashed (dotted) lines shown correspond to CEP with maximum positive (negative) asymmetry in the ion emission, respectively. (d) Measured and predicted CEP-dependent asymmetry for the H^+ emission. The errorbars reflect the statistical uncertainty.

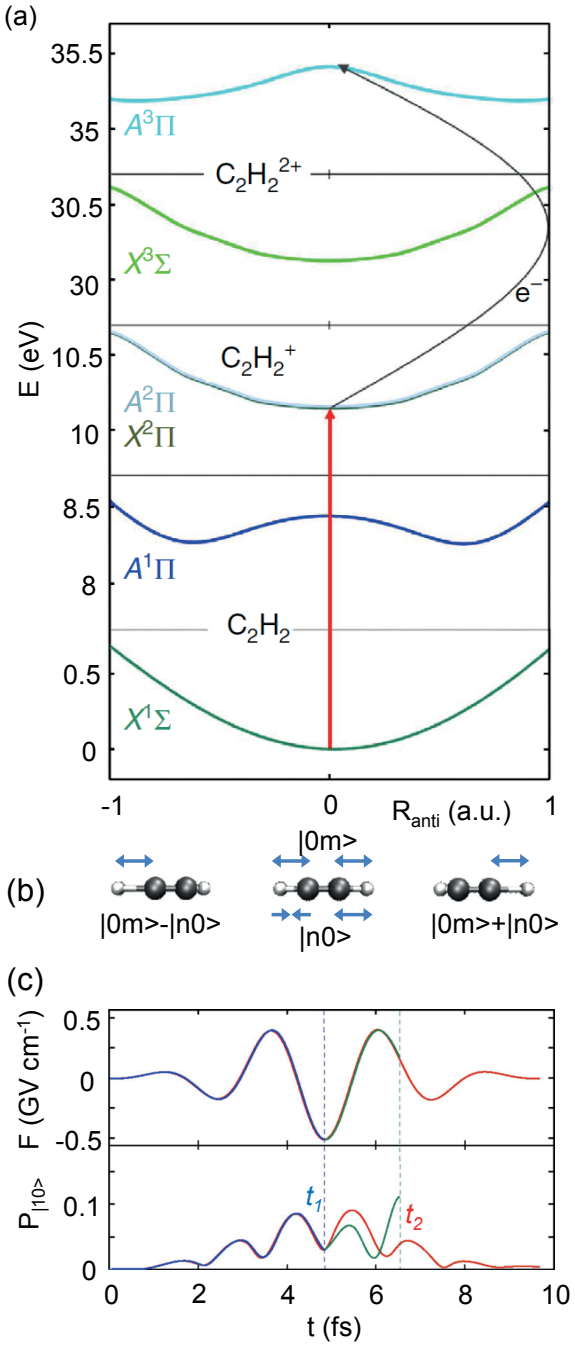

Figure 5.4.: (a) Potential energy curves of the electronic states considered in the ionization and deprotonation along the anti-symmetric stretching coordinate and otherwise equilibrium distance: ground ($X^1\Sigma_g^+$) and first excited state ($A^1\Pi_u$) of the neutral molecule, the cation ground ($X^2\Pi_u$) and degenerate first excited state ($A^2\Pi_u$), and the dication ground ($X^3\Sigma_g$) and first excited state ($A^3\Pi_u$). The red vertical line indicates the tunneling ionization and the grey curved line marks the second ionization step by electron recollision. (b) Illustration of the symmetric $|0m\rangle$ and anti-symmetric $|n0\rangle$ C-H stretching modes and its positive and negative superposition. (c) Top: electric field F of the near-single-cycle pulse used in the calculation for CEP $\phi = \pi$ (red line). Bottom: Population $P_{|10\rangle}$ of the IR-active mode $|10\rangle$. The parts of the field that act on the neutral and cation are displayed as blue and green lines, respectively. The population induced in the neutral molecule is shown as blue line. At the peak of the laser field (t_1), the $|10\rangle$ population is transferred to the cation and its evolution is shown as the green line. Recollisional excitation, 1.7 fs later (t_2), transfers the population to the $A^3\Pi_u$ state of the dication, from where dissociation can occur. Without ionization at t_1, interaction with the entire field would induce only a transient population shown as red line, which vanishes with the end of the laser pulse.

The only stretching mode that is IR-active is the anti-symmetric mode $|10\rangle$, which can be off-resonantly excited in the neutral molecule and cation by the light field. The CEP of the pulse imprints a certain phase (Φ_{CEP}) on the population of the anti-symmetric mode $|10\rangle$, whose evolution during the laser pulse is illustrated in figure 5.2 (b). As described in the following, due to ionization, excitation of the asymmetric C-H stretching mode $|10\rangle$ in the neutral molecule and in the cation is sufficient to initiate a vibrational wavepacket motion leading to asymmetric deprotonation of the dication. The symmetric mode contributions required for the wavepacket motion arise from the tunnel ionization process occurring at t_1. The ionization is modelled by projecting the vibrational wavepacket from the ground state potential energy surface (PES) of the neutral molecule onto the one in the cation. Due to the slightly different shapes of the PES's of the ground states of the neutral and cationic molecules, this projection leads to a slight population of the IR inactive symmetric stretching mode $|01\rangle$. Interaction with the laser field for times $t_1 < t < t_2$ leads to further population of the $|10\rangle$ mode, as illustrated in figure 5.2 (b). At t_2, the electron liberated at t_1 recollides with the molecular ion, leading to population of the relevant $A^3\Pi_u$ state of the dication. In this second ionization step the vibrational wavepacket is projected from the cationic ground state to the dissociative dicationic $A^3\Pi_u$ state. The dominant direction of the deprotonation depends on the sign in the superposition of the symmetric and asymmetric stretching modes (equation 5.1). If this sign can be controlled, the predominant deprotonation directino can be controlled.

In the simulations it is indeed observed that the propagation of the vibrational wavepacket in the dication to either one of the dissociative channels (H^+ + CCH^+ and HCC^+ + H^+) can be manipulated by the CEP. Evaluation of the fraction of the wavepacket correlating with the individual dissociation channels provides the theoretical asymmetry plotted in figure 5.3(d). The theoretical curve shows excellent agreement with the experimental data, which lends support to the novel sub-femtosecond control mechanism. We expect that the presented control scheme is applicable to the control of a variety of chemical processes in symmetric molecules.

6. Conclusions and outlook

Combining phase-tagged near-single-cycle pulses with coincidence spectroscopy to study non-sequential double ionization has provided new insights into a fundamental process in strong-field physics.

Investigating the elementary dynamics responsible for NSDI has become possible by confining the double ionization dynamics of Ar to an isolated recollision event. Resolving the CEP-dependence of the two-electron spectra has allowed us to trace the correlated electron emission on attosecond timescales. In particular, we have demonstrated that, owing to depletion of the excited Ar^+ ions, the second electron is emitted before the maximum of the laser electric field following recollision of the first electron. Predictions based on recollision excitation with sub-cycle depletion (RESD) agree well with the observed intensity and CEP dependence of single-cycle NSDI of Ar.

The same mechanism has also been shown to govern single-cycle NSDI of N_2. In the framework of RESD it is possible to understand both, the remarkably high degree of similarity and the distinctive differences between the results obtained for Ar and N_2.

Averaged over the CEP, the measured two-electron momentum spectrum exhibits a cross-shape, which has not been observed in previous experiments, all of them using longer laser pulses. This suggests that the transition from the near-single-cycle regime to the multi-cycle regime substantially modifies the dynamics of NSDI. Indeed, we have observed an abrupt change in the recorded correlation spectra when increasing the pulse duration. The altered double-ionization dynamics lead to a considerable increase of the contribution of anti-correlated electron emission to NSDI in the multi-cycle regime.

Whereas our semiclassical model captures the essential features of the experimental single-cycle NSDI data, quantitative disagreement between experiment and theory exists with regard to the phase shift between the Ar^+ and Ar^{2+} asymmetry curves. For longer pulse durations, the calculations fail to predict the observed anti-correlated electron emission. More sophisticated models accounting for Coulomb and exchange interaction, as well as for multiple recollisions, are certainly needed to fully resolve the correlated electron motion underlying NSDI. More importantly, however, our highly-differential data provides a solid basis for assessing the validity of different theoretical approaches and will hopefully contribute to the emergence of a coherent and quantitative theoretical description of NSDI from the single to the multi-cycle regime.

By applying the experimental scheme of phase-tagged coincidence momentum imaging to the study of molecular dynamics it is possible to obtain detailed information on the processes leading to the breaking of chemical bonds. The approach has allowed us to distinguish between asymmetries acquired in the ionization and the dissociation of N_2O and C_2H_2. Specifically, the CEP-dependent recoil momentum spectra, obtained for dications prior to dissociation, demonstrate for both molecules that electron recollision is the dominant route to double ionization at the

present laser conditions. Despite this similarity, the mechanisms responsible for the asymmetric ion ejection during dissociation are intrinsically different for the two molecules. In the case of the asymmetric N_2O, the data indicate that for the majority of the fragmentation channels, the CEP-dependence is caused by the orientation dependence of either single ionization by tunneling or double ionization facilitated by electron recollision.

Due to the symmetry of C_2H_2, however, the orientation selection effect is ineligible for explaining any asymmetries in the dissociation of this molecule. Nevertheless, a significant CEP-dependence is observed in the direction of the proton emission following double ionization of C_2H_2. This result is interpreted in terms of a new control mechanisms based on the manipulation of the phases of the components of a vibrational wavepacket excited by the laser before double ionization. We expect this new control scheme to be widely applicable to manipulate a variety of chemical processes in symmetric molecules.

So far, only ions were detected in our experiments on molecular dynamics. Deeper insight, especially into the ionization step, could be achieved by additionally detecting electrons in coincidence with the fragment ions. In particular, recording the correlated two-electron momentum distributions for a dissociating molecule may help identifying the involved electronic states and would allow us to study the correlated electron motion in the molecular frame. Even though such quadruple coincidence (two ions and two electrons) experiments require extraordinary long-term stability and high repetition rate, they may become possible using a new laser system, which became very recently available. While the degree of control of the ion emission has been rather limited in the experiments so far, it might be further enhanced in pump-probe experiments. In such a scheme, a first laser pulse prepares a target in excited states, which can then be efficiently manipulated with a second, phase-controlled or phase-tagged, near-single-cycle pulse.

Besides the widespread perspectives for experiments on molecular dynamics, the number of open questions on double ionization of atoms is far from exhausted. In the present work, single-cycle NSDI of Ar has been thoroughly studied. However, the intensity dependency towards the sequential double ionization (SDI) limit has not yet been carefully examined due to the low signal to noise ratio at the high intensities required to drive SDI. SDI is also the dominant pathway in circularly polarized fields. Earlier experiments (e.g. [84]) and recent calculations [85, 86] hold out the prospect of yet unobserved effects in double ionization by elliptically polarized near-single-cycle pulses. In particular, *angular streaking* [87] enables attosecond tracing of electron emission without the use of attosecond pulses.

The present experimental results on single-cycle NSDI of Ar and N_2 are well understood in terms of the RESD mechanism. For increased laser wavelength, the dominant NSDI mechanism is expected to change as the increased electron recollision energies promote direct electron impact ionization [51]. NSDI experiments at longer wavelength are coming within reach through the recent development of CEP-stable broad-band mid-infrared laser sources [88]. At 800 nm wavelength, NSDI of neon is known to preferentially proceed via the (e,2e) mechanism [2]. The question whether the transition from multi-cycle to single-cycle NSDI of Ne provides similarly surprising results as for Ar is still open. The same applies to NSDI of He [89, 47], which is of particular interest due to the feasibility of a nearly exact quantum mechanical treatment of the correlated electron dynamics [90].

7. Included publications

7.1. Publication I

B. Bergues, M. Kübel, N. G. Johnson, B. Fischer, N. Camus, K. J. Betsch, O. Herrwerth, A. Senftleben, A. M. Sayler, T. Rathje, T. Pfeifer, I. Ben-Itzhak, R. R. Jones, G. G. Paulus, F. Krausz, R. Moshammer, J. Ullrich, and M. F. Kling, Attosecond tracing of correlated electron-emission in non-sequential double ionization. *Nat. Commun.* **3**, 813 (2012).

Motivated by the successful implementation of the phase-tagged REMI in early 2010, it was our declared goal to record CEP-dependent electron correlation spectra for NSDI of Ar. After many long nights in the lab, we mastered the difficulty of measuring clean electron-ion coincidences and collected the data for this paper. I was deeply involved in performing the experiment and analyzed the major part of the data. In this process, I learned how to extract the correlation spectra and developed a considerable amount of analysis tools and methods. Furthermore, I assisted Boris Bergues in the development of the semi-classical model and implemented my own version of it for cross checking. I contributed largely to the interpretation of the data and the writing of the manuscript.

nature COMMUNICATIONS

OPEN

ARTICLE

Received 26 Jan 2012 | Accepted 28 Mar 2012 | Published 8 May 2012

DOI: 10.1038/ncomms1807

Attosecond tracing of correlated electron-emission in non-sequential double ionization

Boris Bergues[1,*], Matthias Kübel[1,*], Nora G. Johnson[1,2], Bettina Fischer[3], Nicolas Camus[3], Kelsie J. Betsch[1,4], Oliver Herrwerth[1], Arne Senftleben[3], A. Max Sayler[5,6], Tim Rathje[5,6], Thomas Pfeifer[3], Itzik Ben-Itzhak[2], Robert R. Jones[4], Gerhard G. Paulus[5,6], Ferenc Krausz[1], Robert Moshammer[3], Joachim Ullrich[3,7] & Matthias F. Kling[1,2]

Despite their broad implications for phenomena such as molecular bonding or chemical reactions, our knowledge of multi-electron dynamics is limited and their theoretical modelling remains a most difficult task. From the experimental side, it is highly desirable to study the dynamical evolution and interaction of the electrons over the relevant timescales, which extend into the attosecond regime. Here we use near-single-cycle laser pulses with well-defined electric field evolution to confine the double ionization of argon atoms to a single laser cycle. The measured two-electron momentum spectra, which substantially differ from spectra recorded in all previous experiments using longer pulses, allow us to trace the correlated emission of the two electrons on sub-femtosecond timescales. The experimental results, which are discussed in terms of a semiclassical model, provide strong constraints for the development of theories and lead us to revise common assumptions about the mechanism that governs double ionization.

[1] Max-Planck-Institut für Quantenoptik, D-85748 Garching, Germany. [2] J.R. Macdonald Laboratory, Department of Physics, Kansas State University, Manhattan, Kansas 66506, USA. [3] Max-Planck-Institut für Kernphysik, D-69117 Heidelberg, Germany. [4] University of Virginia, Charlottesville, Virginia 22904, USA. [5] Institut für Optik und Quantenelektronik, Friedrich-Schiller-Universität, D-07743 Jena, Germany. [6] Helmholtz Institut Jena, D-07743 Jena, Germany. [7] Physikalisch-Technische Bundesanstalt, D-38116 Braunschweig, Germany. *These authors contributed equally to this work. Correspondence and requests for materials should be addressed to B.B. (email: boris.bergues@mpq.mpg.de) or to M.F.K. (email: kling@phys.ksu.edu).

Many fundamental processes in nature such as the formation and dissociation of molecules are governed by multi-electron dynamics (MED). Understanding MED is one of the grand contemporary challenges of quantum physics. While the ground state properties of multi-electron systems are described with reasonable accuracy, the modelling of their dynamics is still in its infancy. Even for rather simple systems involving only a few interacting electrons such as low-Z atoms beyond helium (Z being the nuclear charge), the exact theoretical treatment of MED is hardly practicable. The identification of suitable approximations that capture the essential features of MED relies on the development of experiments aimed at resolving the electron dynamics on the characteristic attosecond timescale of their motion. An established technique for resolving one-electron dynamics on sub-femtosecond scales involves the use of a strong few-cycle infrared laser field as a clock[1–3]. The well-known concept of attosecond streaking spectroscopy has permitted the observation of single-electron dynamics with attosecond time resolution[4]. Despite this progress, however, the ultrafast dynamics of multiple electrons has resisted direct observation, even though far-reaching conclusions were drawn from kinematically complete strong-field double[5,6] and multiple ionization[7] experiments.

Among countless phenomena involving the motion of multiple electrons, non-sequential double ionization (NSDI) of atoms is a pure and, meanwhile, classic example for MED in the presence of strong fields. As reported for rare gases almost 30 years ago[8], it manifests itself as an unexpected, orders-of-magnitude enhancement in the strong-field double ionization yield. This finding cannot be explained within the framework of the single active electron approximation, where both electrons are assumed to be ionized sequentially and independently of each other. A mechanism correlating the emission of the two electrons must be included to adequately describe this effect and different models have been proposed[5,9].

Since the pioneering works, NSDI has been the subject of numerous experimental and theoretical studies (for a recent review, see ref. 6 and references therein). Recording the momentum spectra of doubly[10,11] and multiply[7] charged ions provided clear evidence that the emission of the second electron is triggered by the laser-driven recollision of the first electron with its parent ion. Even more insight into the process was gained in kinematically complete studies where the correlated two-electron momentum distributions were measured[11] and investigated for different laser parameters[12–15]. Measurements of the dynamics of NSDI in near-single cycle laser pulses have been restricted to recoil-ion spectra, which did not allow for the direct retrieval of the correlated electron-emission dynamics[16,17]. The sub-cycle dependence of electron correlation spectra has been explored by various theoretical studies, where the double-ionization dynamics were confined to a single cycle of a laser pulse[12,18]. A direct test of the validity of these theoretical models, however, has been impeded so far by the lack of kinematically complete experimental data obtained with ultrashort pulses and precise control or knowledge of the electric field.

Here we present measurements of correlated two-electron momentum spectra for the strong-field NSDI of argon atoms in the single-cycle limit. The measured spectrum exhibits a cross-shaped structure that qualitatively differs from spectra recorded in all previous experiments using many-cycle pulses. Confining the ionization dynamics to a single laser cycle by choosing an adequate carrier envelope phase (CEP) allows us to perform a clean experiment with only one single recollision event contributing to NSDI, thus excluding the contribution of multiple recollisions that hamper the interpretation of experimental results. From the CEP-resolved spectra the correlated emission of two electrons is traced on sub-femtosecond timescales. In particular, we can determine at which time the second electron is released within the laser pulse.

Results

Experimental set-up. A detailed sketch of our experimental set-up is given in the Methods. Briefly, the experiments were performed using linearly polarized laser pulses with a central wavelength of 750 nm and a full-width at half-maximum (FWHM) of the temporal intensity envelope of 4 fs, which were generated at a repetition rate of 3 kHz[19]. The electric field of the laser pulse can be approximated as $E(t) = E_0 \cos^2(t/\tau) \cos(\omega t + \phi)$, where E_0 is the field amplitude, ω is the carrier frequency, τ is the pulse duration, and ϕ is the CEP. Combining a reaction microscope (REMI)[20] with a newly developed phase-tagging technique[21], we obtained the CEP of the laser pulse for each and every ionization event[22] recorded with the REMI. The laser was focussed to a maximum instantaneous intensity of $I_0 = c\varepsilon_0 E_0^2 = (3.0 \pm 0.6) \times 10^{14}\,\mathrm{W\,cm^{-2}}$ into a cold supersonic gas jet of neutral argon atoms located in the centre of the REMI. The momenta of electrons and ions created in the laser focus were measured in coincidence in the REMI. For the conditions of our experiment, the ratio of the measured Ar^{2+} to Ar^{+} yields was about 0.1%.

Two-electron momentum distributions. Figure 1 shows experimental correlated two-electron momentum distributions, where the number of recorded double-ionization events is plotted as a function of the momenta p_1 and p_2 along the laser polarization axis of electron 1 and electron 2, respectively. The spectra are symmetric with respect to the $p_2 = p_1$ diagonal because the two electrons, the recolliding electron and the one liberated as a result of this recollision, cannot be distinguished in the experiment. The CEP-averaged correlation spectrum is shown in Fig. 1a. The cross-shaped structure indicates that the momentum of one electron is always close to zero whereas the momentum of the other electron varies between −1.5 to 1.5 atomic units. Similar structures were found in a recent theoretical study on NSDI of argon employing S-matrix theory[18]. So far, however, such a cross-shaped two-electron momentum distribution has not been observed experimentally. This strongly suggests that the physical mechanisms that govern NSDI in the near single-cycle regime differ from the many-cycle regime, where previous experiments were performed. The CEP-resolved correlation spectra presented in Fig. 1b–e exhibit a strong CEP dependence. For CEP values of 155° (Fig. 1c) and 335° (Fig. 1e), the signal is predominantly (with more than 80% of the counts) located below and above the red diagonal line ($p_2 = -p_1$), respectively. For intermediate CEP values of 65° (Fig. 1b) and 245° (Fig. 1d), the signal is distributed on both sides of the red diagonal.

The semiclassical model. To interpret the experimental results, we investigate the recollision-induced ionization dynamics using a semiclassical model (for details, see Methods). In the present intensity regime, essentially two mechanisms may contribute: the first is the (e, 2e)-mechanism, in which the recolliding electron directly promotes a second electron into the continuum via electron impact ionization[23]. The second is recollision-induced excitation with subsequent ionization (RESI)[24,25], where the recolliding electron excites the parent ion, which is subsequently ionized by the laser field as depicted in Fig. 2a. A key property of the RESI process is the delayed emission of the second electron with respect to the recollision event, the latter occurring near the zero crossing of the electric field of the laser. As shown below, our experimental results identify RESI as the dominant process, and, more importantly, enable the determination of the emission delay.

In our semiclassical model, the probability to liberate the first electron at any moment in time is calculated using the instantaneous Ammosov–Delone–Krainov (ADK) tunnelling rate including a correction factor to account for over-the-barrier ionization[26]. The propagation of the electron after the ionization in the electric field of the laser pulse is treated classically, neglecting the Coulomb interaction with the ionic core and with the other electron. For the RESI

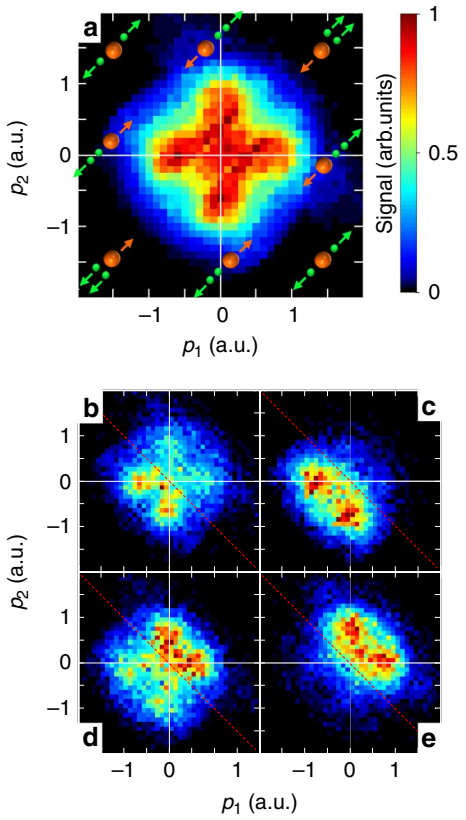

Figure 1 | Correlated two-electron momentum spectra. Experimental two-electron momentum distributions for the double ionization of argon with near-single cycle, 4 fs laser pulses at a maximum instantaneous intensity of $I_0 = 3.0\times10^{14}\,\mathrm{Wcm^{-2}}$. Here p_1 and p_2 are the momentum components of the first and the second electron along the laser polarization direction, respectively. The cartoons in (**a**) illustrate the emission direction of the two electrons (green spheres) and the ion (orange spheres). The arrows represent the sign of the longitudinal momentum of the fragments. An event in the first or third quadrant corresponds to the emission of two electrons into the same direction; electrons emitted in opposing directions appear in the second or fourth quadrant. A cross-shaped structure is seen in the phase-integrated plot (**a**), reflecting the correlated nature of the NSDI process. In images (**b–e**), spectra are shown for different values of the CEP, namely (**b**) 65°, (**c**) 155°, (**d**) 245° and (**e**) 335°. The spectra are averaged over a $\pi/6$ CEP range and are symmetrized with respect to the $p_2 = p_1$ diagonal. Images (**c**,**e**) correspond to CEPs with maximum asymmetry in the Ar^{2+} emission and (**b**,**d**) to CEP with zero asymmetry in the Ar^{2+} emission. The same colour scale is used for all (**a–e**).

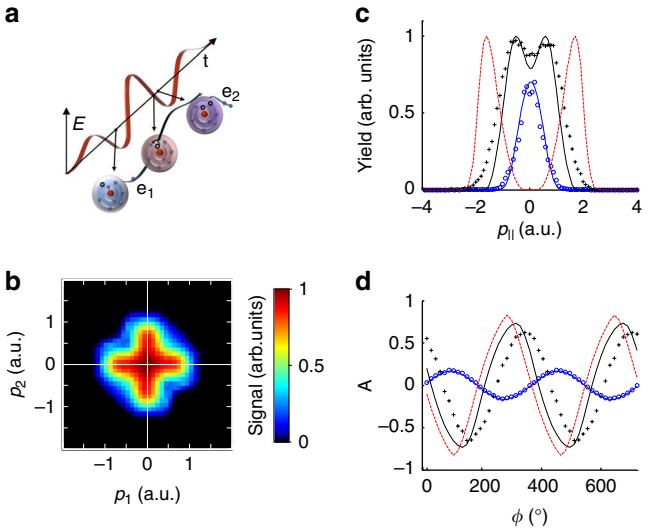

Figure 2 | Comparison of experimental and theoretical results. (**a**) Illustration of the RESI mechanism dominating NSDI at the experimental parameters: the laser electric field as a function of time is drawn along with schematics of the electronic configuration of the outer shell of Ar at three key time steps of the process. First, an electron e_1 is liberated from Ar, leaving a hole (small circle) in the outer shell of Ar^+ (light blue). Second, an excited Ar^+ ion (pink colour) is produced upon recollision of electron e_1 near the zero-crossing of the electric field. Finally, a second electron e_2 is liberated from the excited Ar^+ ion forming Ar^{2+} (purple). (**b**) Calculated two-electron momentum spectrum averaged over CEP for the experimental parameters using the semiclassical RESI model, described in the text. (**c**) Experimental recoil-ion momentum spectra (for momenta $p_{||}$ parallel to the polarization axis) for single (Ar^+ ions, blue open dots) and double ionization (Ar^{2+} ions, black crosses), respectively, averaged over CEP. The experimental data are compared with the model results for single ionization (blue line), and double ionization ((e, 2e)-mechanism (dashed red line) and RESI-mechanism (black line)). Scattering angles $\beta = 0°$ and $\beta = 20°$ are used to simulate the (e, 2e) and RESI processes, respectively. (**d**) Comparison of the experimental and calculated asymmetry A as a function of the CEP ϕ for Ar^+ and Ar^{2+} (using the same symbols and colour coding as in (**c**)). All the theoretical results shown in (**b**,**c**,**d**) were obtained from the same simulation with the parameters given in the text.

process, the calculation is performed as follows: if the first electron recollides with the parent ion with sufficient kinetic energy, the lowest excited state of Ar^+ is populated and the second electron is liberated by subsequent field ionization. For the (e, 2e) process, we consider only recolliding electrons having sufficient energy to overcome the second ionization potential of argon. In this case, the second electron is assumed to be liberated with zero-initial momentum via electron impact ionization. In both the RESI and (e, 2e) processes, the magnitude of the first electron momentum, just after the recollision, is determined by energy conservation. The direction of this momentum vector, described by the scattering angle β (where β is the angle between the momentum vectors just before and just after the recollision), is undetermined in our model and constitutes the only free parameter. The dependence of the simulated correlation spectra on the scattering angle is discussed in the Methods.

Comparison of measured and calculated spectra. The results of our calculations are displayed in Fig. 2b–d, for the instantaneous peak intensity of $I_0 = 2.9\times10^{14}\,\mathrm{Wcm^{-2}}$ (the cycle-averaged peak intensity equals $I_0/2$) and a pulse duration of 3.8 fs (FWHM in intensity). In Fig. 2c, the measured CEP-averaged momentum distributions of Ar^+ and Ar^{2+} are compared with their simulated counterparts for the (e, 2e) and RESI mechanisms. The calculated width of the Ar^+ spectrum is in good agreement with the measurement. The double hump structure of the Ar^{2+} spectrum is also correctly reproduced by the simulation for the RESI mechanism, where the best agreement was reached with $\beta = 20°$. We note that small contributions of higher excited Ar^+ states or the (e, 2e) mechanism would lead to a slightly broader momentum distribution of the Ar^{2+} ions in the calculations. The prediction for the (e, 2e) mechanism alone (red line in Fig. 2c), however, does not reproduce the experimental Ar^{2+} spectrum even if we use $\beta = 0°$, where the best agreement was reached for this mechanism. Interestingly, the double hump structure, which was previously believed to originate from an (e, 2e) mechanism[27] can be reproduced considering the RESI mechanism only. Figure 2b shows the calculated CEP-averaged correlation spectrum for the RESI process, which exhibits the characteristic cross-shaped structure observed in the experiment.

The corresponding two-electron momentum distribution for the (e, 2e) process is shown for comparison in the Methods.

Comparison of measured and calculated asymmetries. In earlier work, the (e, 2e) mechanism was invoked to explain the CEP-dependent Ar^{2+} recoil-ion spectra at about twice the intensity[16,28]. Our results clearly indicate that, under the conditions of the present experiment, electron impact excitation to the lowest excited Ar^+ state and subsequent field ionization (RESI) constitutes the main contribution to NSDI of argon. To discuss the CEP dependence of NSDI, it is instructive to introduce the asymmetry parameter $A=(N_+-N_-)/(N_++N_-)$, where N_+ and N_- denote the number of ions with positive and negative momentum along the polarization axis, respectively. In Fig. 2d, the measured asymmetries of the Ar^+ and Ar^{2+} yields as a function of CEP are compared with the results of our calculations (using the parameters given above). The experimental CEP is only determined up to a constant offset (see Methods). We use the theoretical Ar^+ asymmetry as a reference to set the value of the offset such that the maximum of the measured Ar^+ asymmetry curve coincides with the maximum of the calculated one. Remarkably, both the amplitude and the shape of the simulated Ar^+ asymmetry curve exactly match the measurement. Whereas the amplitudes of the calculated and measured Ar^{2+} asymmetry curves are in good agreement, the calculated phase shifts between the Ar^+ and the Ar^{2+} asymmetry curves (154° for RESI and 177° for (e, 2e)) do not match the measured phase shift of 114°. We would like to emphasize that such asymmetry data obtained simultaneously for single and double ionization is only accessible in the few and near single-cycle regime and was not available before. The measured phase shift represents a useful observable to test the validity of theoretical models. In spite of the small discrepancies between the experimental data and the simulation results, the overall agreement is impressive, considering the simplicity of the theoretical model.

Discussion

In light of the good agreement between simulation and experiment, the electron dynamics can now be analysed in more detail. In Fig. 3, experimental (Fig. 3a,b) and simulated (Fig. 3c,d) correlation spectra are compared for CEP values that correspond to maximum (Fig. 3a,c) and zero (Fig. 3b,d) Ar^{2+} asymmetry, respectively.

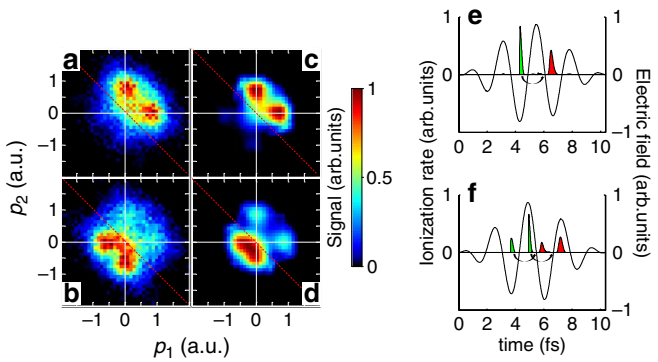

Figure 3 | Timing of the first and second ionization. Comparison of measured (**a,b**) and calculated (**c,d**) two-electron momentum distributions for CEPs corresponding to a maximum (**a,c**) and zero value (**b,d**) of the Ar^{2+} asymmetry. The predicted ionization rates of the first (green-shaded area) and second (red-shaded area) electron contributing to NSDI are displayed in (**e**) and (**f**) together with the electric field of the laser pulse (black line) for maximum and zero Ar^{2+} asymmetry parameters, respectively. Each black arrow points to the time of recollision for electrons liberated near the tail of the arrow. In (**a,c,e**) only a single recollision leads to NSDI, while in (**b,d,f**) two recollision events in successive half-cycles contribute.

Figures 3e and 3f show the calculated ionization rates of the first (green area) and second (red area) electron together with the temporal profile of the laser electric field for these two CEP values. Due to depletion of the excited Ar^+ population, the second electron is emitted before the maximum of the laser electric field. Our analysis thus reveals that under our experimental conditions, it is the momentum of the first electron that is close to zero while the momentum of the second electron is non-zero and varies as a function of the CEP. Averaged over the CEP, this results in the cross-shaped structures seen in Figs 1a and 2b. This finding is in contrast to the common assumption that the second electron in the RESI mechanism is released at the peak of the electric field and acquires a small momentum distributed around zero[7].

Multiple recollision events, which occur in the several-to-multi-cycle regime, severely hamper the interpretation of measured correlation spectra. Figure 3 illustrates how the short pulses used in our study allow for a clean experiment by confining NSDI to essentially one single recollision event for an appropriate choice of the CEP yielding the maximum Ar^{2+} asymmetry. For a CEP corresponding to a zero Ar^{2+} asymmetry (Figs 3b and d), precisely two recollision events from consecutive half-cycles contribute to NSDI. Here the second electron, liberated as a result of the first recollision, acquires a higher momentum with positive sign whereas the second recollision results in a lower momentum with negative sign. Even in this case, the change in sign of the slope of the electric field allows for distinguishing the contributions from the two consecutive recollision events.

With the analysis presented in Fig. 3, we can also unambiguously determine whether excitation of the singly charged ion occurs without recollision, that is, via laser excitation alone. Recollision-induced excitation takes place about three quarters of a cycle after the emission of the first electron. In contrast, a laser-excited ion would be efficiently ionized in the half-cycle following ionization of the first electron, leading to a signal on either side of the red diagonal in Fig. 3a, which is not observed. Disentangling laser excitation from recollisional excitation is possible only because the double ionization process has been confined to a single cycle.

Using the infrared field as an inherent clock and neglecting the effect of the Coulomb potential as commonly assumed in the attosecond streaking scenario[1,29], we can retrieve the electron's most likely emission time, which is directly mapped onto its drift momentum. Specifically, $\Delta t=\arccos(p_0/p_{max})/\omega$, where p_0 and p_{max} are the most probable and the maximum momentum of electron 2, respectively. From the experimental data, we find the maximum emission probability of the second electron at 210 ± 40 attoseconds before the peak of the half-cycle following the recollisional excitation. This is in good agreement with our simulations predicting the emission leading the maximum of the field by 230 attoseconds.

In conclusion, using a near-single-cycle laser pulse with appropriate CEP, the double ionization dynamics of argon could be confined to an isolated recollision event, allowing us to investigate the elementary process responsible for NSDI. The measured correlated two-electron momentum spectrum has a cross-shaped structure, which has not been observed in previous experiments, all of them using longer laser pulses. This suggests that the transition from the multi-cycle to the near-single-cycle regime substantially modifies the dynamics of NSDI. Resolving the CEP-dependence of the correlated two-electron spectra has provided new insights into the double ionization dynamics. In particular, we have shown that, owing to depletion of the excited Ar^+ ions, the second electron is emitted before the maximum of the laser electric field. The mean delay between the zero crossing of the electric field and the emission of the second electron could be determined unambiguously. More generally, the highly differential data obtained in our experiment provide strong constraints to multi-electron theories and may greatly stimulate their development. Whereas our semiclassical model captures the essential features of

the data, electron correlations enter the model only indirectly via the ionic excitation and the scattering angle. More sophisticated models accounting for Coulomb and exchange interaction are certainly needed to fully resolve the correlated electron motion and predict the correct value for the phase shift observed between the Ar^+ and Ar^{2+} asymmetry curves. Extension of our approach to the study of molecular dynamics may give a more detailed insight into the breaking of chemical bonds.

Methods

Experimental technique. The experiment was performed at the AS-1 attosecond beamline at the Max Planck Institute of Quantum Optics[19]. Linearly polarized laser pulses with a central wavelength of 750 nm, an energy of 400 μJ and a FWHM of the temporal intensity envelope of 4 fs are generated at a repetition rate of 3 kHz in an amplified laser system. Active stabilization of the CEP is difficult to conciliate with the long data-acquisition times (32 h for the present experiment) imposed by coincident particle-detection schemes. As a significant advance over previous efforts to measure the sub-femtosecond dynamics of the NSDI of argon, we recorded the CEP of each laser pulse by sending a fraction of the laser beam (25 μJ) into a single-shot stereographic above-threshold ionization (Stereo-ATI) phase-meter[21] (see Fig. 4).

A detailed description of the CEP measurement technique using ATI and the Stereo-ATI phase meter can be found in refs 17,21,22,30,31. Briefly, the time-of-flight spectra of electrons emitted along both directions of the laser polarization axis are recorded on either side of the apparatus (left and right detector in Fig. 4). For each laser shot, the CEP is inferred from the asymmetry between the left and the right TOF spectra. The CEP is measured up to a constant offset in the phase meter.

A fraction (11 μJ) of the remaining part of the laser beam is focussed with a spherical mirror (f=25 cm) into a well-localized (1 mm width) and cold supersonic gas jet of neutral argon atoms in the centre of a REMI[20]. Ions and electrons created in the laser focus (~40 μm diameter) are extracted by a weak electric field towards microchannel plate (MCP) detectors equipped with delay line anodes for position readout at the left and right side of the instrument, respectively. A pair of Helmholtz coils generates a homogenous magnetic field to guide the electrons towards their detector reaching a 4π acceptance angle for all electrons of interest (Fig. 4). The 3D momentum vectors of ions and electrons are reconstructed from their measured flight times and impact positions on the corresponding detectors. The low density of the jet allows for detection of on average less than one ionization event per laser shot, an important constraint to minimize the number of false coincidences, when measuring ions and electrons in coincidence. In the present experiment, 0.25 ions per laser shot were detected on average.

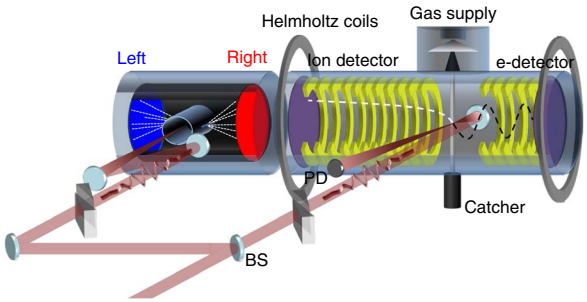

Figure 4 | Experimental set-up. Schematic of the set-up consisting of a single-shot Stereo-ATI phase meter (left chamber) and a REMI spectrometer (right chamber). A beamsplitter (BS) directs the laser pulses into both chambers. Each arm is equipped with a pair of fused-silica wedges for compensating residual chirp. The phase meter contains a layer of μ-metal to shield from external magnetic fields. The inner gas cell is filled with xenon gas at a pressure of about 5×10^{-3} mbar. In the Stereo-ATI, xenon atoms are ionized near the focus of the horizontally polarized laser beam, and the electrons produced enter the high-vacuum drift tubes through slits. Electrons resulting from the ionization by a single-laser shot are detected by MCP detectors to the left and to the right, enabling the determination of the CEP for each REMI event, as described in the text. Simultaneously, ions and electrons created in the overlap of the laser focus and a skimmed supersonic jet of the REMI are extracted from the interaction region by a weak electric field (3 V cm^{-1}) and detected by MCP and delay line detectors on the left and right side of the instrument, respectively. Helmholtz coils are used to facilitate the detection of electrons over a solid angle of 4π. The jet is efficiently pumped by the catcher. The master trigger for the electronics is provided by a fast photodiode (PD). The ion and electron optics are symmetric in reality, and a few electrodes have been removed for visualization of the laser path.

Data processing and false coincidences. To generate the correlated two-electron momentum distributions shown in Fig. 1, we select laser shots where at least one electron and one Ar^{2+} ion are detected. As most of the time only one of the two electrons generated together with Ar^{2+} is detected (because of the single-particle detection efficiency of ~50%), the momentum of the missing second electron is calculated using momentum conservation. Electrons emerging from single ionization of argon introduce a false coincidence background in the electron correlation spectra of less than 15%. The contribution of false Ar^{2+} events (<0.5% of the total Ar^{2+} signal) is negligible.

Laser intensity and CEP offset measurement. The analysis of the Ar^+ spectra, recorded in the same measurement, provides important information allowing for *in situ* determination of the peak intensity of the laser pulse in the interaction region, as shown in Fig. 5. Furthermore, the comparison of the measured and calculated Ar^+ asymmetry curves allows for the determination of the absolute CEP of the laser pulses in the interaction region in the REMI.

Simulation procedure. The yield $Y(t)$ of electrons emitted in a time interval $[t, t+dt]$ is calculated using the instantaneous ADK tunnelling rate w_{ADK} (refs 32,33) summed over all occupied degenerate states of the outer shell. This rate is further multiplied with the correction factor from (ref. 26) to account for above the barrier ionization:

$$w(t) = w_{ADK}(t) \times \exp\left(-\alpha \frac{Z^2 E(t)}{I_p (2I_p)^{3/2}}\right). \quad (1)$$

Here I_p is the ionization potential and α is a numerical factor adjusted such that the rate, $w(t)$, fits the result obtained by solving the Schrödinger equation numerically. The value of parameter α is 9 for Ar and 8 for Ar^+ (ref. 26).

The ionization yield is calculated as

$$Y(t) = N(t_i) \exp\left(-\int_{t_i}^{t} w(t')dt'\right) w(t)dt, \quad (2)$$

where $N(t_i)$ is the initial population of the electronic state under consideration. After ionization, at time t_0, the electron enters the continuum with zero momentum at a distance x_t of the parent ion, where x_t is the exit of the tunnel. The electron is propagated classically in the electric field of the laser pulse, neglecting the interaction with the parent ion. The electron may return at a later time t_1, to the position at x_0, with sufficient energy to either excite the parent ion in the case of RESI or to directly ionize the parent ion in the case of the (e, 2e)-mechanism.

For the RESI process, the calculation is performed as follows: if the kinetic energy, $E_{kin}(t_1)$ of the returning electron is higher than the excitation energy, E_{exc} = 13.5 eV, needed to reach the lowest excited state of Ar^+, this state, $(3s\,3p^6)\ ^2S_{1/2}$, is populated with the probability $Y(t_0)$ and the propagation of the re-scattered electron is continued with an initial kinetic energy $E'_{kin}(t_1) = E_{kin}(t_1) - E_{exc}$. For the ionization of the second electron from the excited ion, we proceed in the same way as for the ionization of the first electron, using the parameters of the excited state for the ionization rate.

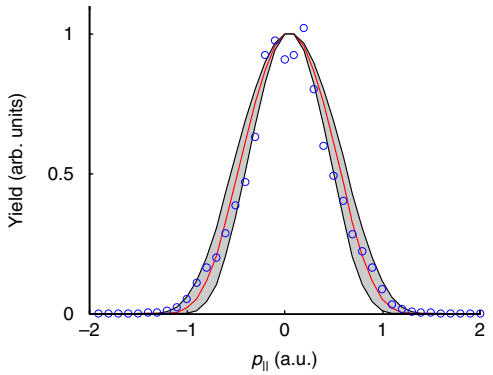

Figure 5 | Determination of the peak intensity. The peak intensity in the laser focus is inferred from the momentum spectra of Ar^+ ions (parallel to the polarization axis) by comparison with simulations. The measured Ar^+ spectrum (open circles) is plotted together with simulated spectra calculated for three different intensities: 3.0×10^{14} W cm^{-2} (red line), 2.4×10^{14} W cm^{-2} and 3.6×10^{14} W cm^{-1} (narrow and wide black spectra respectively). The gray area in-between the two black curves represents the error bars of ±20% in the determination of the peak intensity.

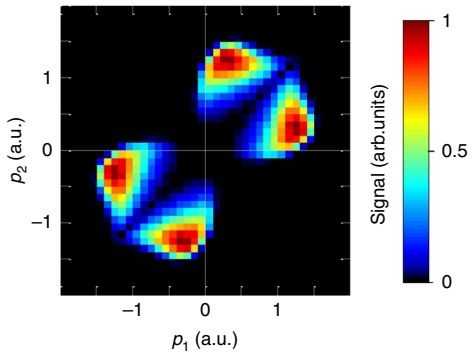

Figure 6 | Simulation results for electron impact ionization. Predicted two-electron momentum distribution for the (e, 2e) mechanism and $\beta = 0°$. The discrepancies between the (e, 2e) calculations and the measured data become even larger for other values of β.

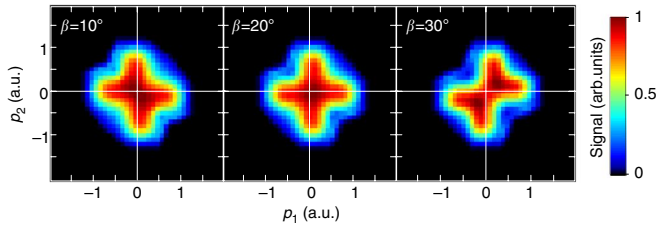

Figure 7 | Sensitivity with respect to the scattering angle. Simulated two-electron momentum distribution assuming the RESI process for three different scattering angles β.

To simulate the (e, 2e) process, a recolliding electron with sufficient energy to overcome the second ionization potential of argon is assumed to produce a second electron with zero-initial momentum. The magnitude of the first electron momentum just after the recollision is determined by energy conservation. As indicated in the main text, the experimental data cannot be described by our model assuming the (e, 2e) process. In addition to the predicted recoil-ion momentum spectrum and asymmetry curve presented in Fig. 2, the two-electron correlation spectrum calculated assuming the (e, 2e) mechanism is shown in Fig. 6.

For both the (e, 2e) and RESI processes, the final drift momentum of the first electron depends on the scattering angle β (the angle between the momentum vectors just before and just after the recollision). The sensitivity of the simulation on the scattering angle is shown in Fig. 7 for the RESI process. We find that the cross-shaped structure is significantly altered if β is varied by ±10 degrees. Focal volume averaging is taken into account by assuming a Gaussian intensity profile, neglecting the intensity variation across the argon gas jet of 1 mm diameter.

References

1. Kienberger, R. *et al.* Atomic transient recorder. *Nature* **427,** 817–821 (2004).
2. Eckle, P. *et al.* Attosecond ionization and tunneling delay time measurements in helium. *Science* **322,** 1525–1529 (2008).
3. Pfeiffer, A. N., Cirelli, C., Smolarski, M., Dörner, R. & Keller, U. Timing the release in sequential double ionization. *Nature Phys.* **7,** 428–433 (2011).
4. Krausz, F. & Ivanov, M. Attosecond physics. *Rev. Mod. Phys.* **81,** 163–234 (2009).
5. Dörner, R. *et al.* Multiple ionization in strong laser fields. *Adv. At. Mol. Opt. Phys.* **48,** 1–36 (2002).
6. Figueira de Morisson Faria, C. & Liu, X. Electron-electron correlation in strong laser fields. *J. Mod. Opt.* **58,** 1076–1131 (2011).
7. Rudenko, A. *et al.* Correlated multi electron dynamics in ultrafast laser pulse interactions with atoms. *Phys. Rev. Lett.* **93,** 253001 (2004).
8. L'Huillier, A., Lompré, L. A., Mainfray, G. & Manus, C. Multiply charged ions formed by multiphoton absorption processes in the continuum. *Phys. Rev. Lett.* **48,** 1814–1817 (1982).
9. Walker, B. *et al.* Precision measurement of strong field double ionization of helium. *Phys. Rev. Lett.* **73,** 1227–1230 (1994).
10. Moshammer, R. *et al.* Momentum distributions of Ne^{n+} ions created by an intense ultrashort laser pulse. *Phys. Rev. Lett.* **84,** 447–450 (2000).
11. Weber, Th. *et al.* Correlated electron emission in multiphoton double ionization. *Nature* **405,** 658–661 (2000).
12. Staudte, A. *et al.* Binary and recoil collisions in strong field double ionization of helium. *Phys. Rev. Lett.* **99,** 263002 (2007).
13. Rudenko, A. *et al.* Correlated two-electron momentum spectra for strong-field nonsequential double ionization of He at 800 nm. *Phys. Rev. Lett.* **99,** 263003 (2007).
14. Liu, Y. *et al.* Strong-field double ionization of Ar below the recollision threshold. *Phys. Rev. Lett.* **101,** 053001 (2008).
15. Liu, Y. *et al.* Multiphoton double ionization of Ar and Ne close to threshold. *Phys. Rev. Lett.* **104,** 173002 (2010).
16. Liu, X. *et al.* Nonsequential double ionization at the single-optical-cycle limit. *Phys. Rev. Lett.* **93,** 263001 (2004).
17. Johnson, N. G. *et al.* Single-shot carrier-envelope-phase-tagged ion-momentum imaging of nonsequential double ionization of argon in intense 4-fs laser fields. *Phys. Rev. A* **83,** 013412 (2011).
18. Shaaran, T., Nygren, M. T., & Figueira de Morisson Faria, C Laser-induced nonsequential double ionization at and above the recollision-excitation-tunneling threshold. *Phys. Rev. A* **81,** 063413 (2010).
19. Schultze, M. *et al.* State-of-the-art attosecond metrology. *J. Electron Spectrosc.* **184,** 68–77 (2011).
20. Ullrich, J. *et al.* Recoil-ion and electron momentum spectroscopy: reaction-microscopes. *Rep. Prog. Phys.* **66,** 1463–1545 (2003).
21. Wittmann, T. *et al.* Single-shot carrier-envelope phase measurement of few-cycle laser pulses. *Nature Phys.* **5,** 357–362 (2009).
22. Sayler, A. M. *et al.* Precise, real-time, every-single-shot, carrier-envelope phase measurement of ultrashort laser pulses. *Opt. Lett.* **36,** 1–3 (2011).
23. Corkum, P. B. Plasma perspective on strong-field multiphoton ionization. *Phys. Rev. Lett.* **71,** 1994–1997 (1993).
24. Feuerstein, B. *et al.* Separation of recollision mechanisms in nonsequential strong field double ionization of Ar: the role of excitation tunneling. *Phys. Rev. Lett.* **87,** 043003 (2001).
25. Kopold, R., Becker, W., Rottke, H. & Sandner, W. Routes to nonsequential double ionization. *Phys. Rev. Lett.* **85,** 3781–3784 (2000).
26. Tong, X. M. & Lin, C. D. Empirical formula for static field ionization rates of atoms and molecules by lasers in the barrier-suppression regime. *J. Phys. B.* **38,** 2593–2600 (2005).
27. Rudenko, A. *et al.* Intensity-dependent transitions between different pathways of strong-field double ionization. *Phys. Rev. A* **78,** 015403 (2008).
28. Rottke, H. *et al.* Non-sequential double ionization in a few-cycle laser pulse: the influence of the carrier-envelope phase. *J. Mod. Opt.* **53,** 149–162 (2006).
29. Itatani, J. *et al.* Attosecond streak camera. *Phys. Rev. Lett.* **88,** 173903 (2002).
30. Sayler, A. M. *et al.* Real-time pulse length measurement of few-cycle laser pulses using above-threshold ionization. *Opt. Express* **19,** 4464–4471 (2011).
31. Paulus, G. G. *et al.* Measurement of the phase of few-cycle laser pulses. *Phys. Rev. Lett.* **91,** 253004 (2003).
32. Ammosov, M. V., Delone, N. B. & Krainov, V. P. Tunnel ionization of complex atoms and of atomic ions in an alternating electromagnetic field. *Sov. Phys. JETP* **64,** 1191–1194 (1986).
33. Perelomov, A. M., Popov, V. S. & Terent'ev, M. V. Ionization of atoms in an alternating electric field. *Sov. Phys. JETP* **23,** 924–934 (1966).

Acknowledgements

We acknowledge fruitful discussions with M. Lezius and H. Schröder and experimental support by C.-D. Schröter and N. Kurz. We are grateful for support by the Max Planck Society, the Chemical sciences, Geosciences, and Biosciences Division, Office of Basic Energy Sciences, Office of Science, U.S. Department of Energy under DE-FG02-86ER13491 and DE-FG02-00ER15053, the National Science Foundation under CHE-0822646 and the DFG via the Emmy-Noether program, the International Collaboration in Chemistry program and the Cluster of Excellence: Munich Center for Advanced Photonics (MAP). We acknowledge support by the EU via the ITN ATTOFEL and LaserLab Europe.

Author contributions

B.B. and M.K. performed the measurements and calculations, analysed and interpreted the data; N.G.J., K.J.B., O.H., R.M., R.R.J., and M.F.K. provided experimental support during the measurements; M.F.K. planned the experiment and supervised the work; part of the REMI and support in its operation was provided by A.S., R.M. and J.U.; the phase-meter and support in its operation was provided by A.M.S., T.R. and G.G.P.; B.F., N.C., T.P., I.B., and F.K. contributed to the discussion of the results; the manuscript was prepared by B.B., M.K., N.G.J., K.J.B. and M.F.K and was discussed among all authors.

Additional information

Competing financial interests: The authors declare no competing financial interests.

Reprints and permission information is available online at http://npg.nature.com/reprintsandpermissions/

How to cite this article: Bergues, B. *et al.* Attosecond tracing of correlated electron-emission in non-sequential double ionization. *Nat. Commun.* 3:813 doi: 10.1038/ncomms1807 (2012).

7.2. Publication II

M. Kübel, K. J. Betsch, N. G. Johnson, U. Kleineberg, R. Moshammer, J. Ullrich, G. G. Paulus, M. F. Kling, and B. Bergues, Carrier-envelope-phase tagging in measurements with long acquisition times. *New J. Phys.* **14**, 093027 (2012).

The idea for this paper was born as a spin-off of our experiments on NSDI of argon and nitrogen. In the process of data analysis, it became clear that the slight changes in the CEP measurement may introduce severe artifacts in the recorded CEP-dependent ionization yields. To circumvent these problems, I developed a practical routine which allows for extracting the CEP-dependent yield accurately from our measurements. After having recorded NSDI data at various intensities, we included the measured CEP-dependent double ionization yields as an application example for the improved phase-tagging method in the publication. Besides performing the experiments and developing the new method, I contributed to the writing of the manuscript.

New Journal of Physics
The open-access journal for physics

Carrier-envelope-phase tagging in measurements with long acquisition times

M Kübel[1,8], K J Betsch[1], Nora G Johnson[1,2], U Kleineberg[3], R Moshammer[4], J Ullrich[4,5], G G Paulus[6,7], M F Kling[1,2] and B Bergues[1,8]

[1] Max-Planck-Institut für Quantenoptik, D-85748 Garching, Germany
[2] J R Macdonald Laboratory, Department of Physics, Kansas State University, Manhattan, KS 66506, USA
[3] Department für Physik, Ludwig-Maximilians-Universität, Am Coulombwall 1, D-85748 Garching, Germany
[4] Max-Planck-Institut für Kernphysik, D-69117 Heidelberg, Germany
[5] Physikalisch-Technische Bundesanstalt, D-38116 Braunschweig, Germany
[6] Institut für Optik und Quantenelektronik, Friedrich-Schiller-Universität, D-07743 Jena, Germany
[7] Helmholtz Institut Jena, D-07743 Jena, Germany
E-mail: matthias.kuebel@mpq.mpg.de and boris.bergues@mpq.mpg.de

New Journal of Physics **14** (2012) 093027 (11pp)
Received 26 June 2012
Published 14 September 2012
Online at http://www.njp.org/
doi:10.1088/1367-2630/14/9/093027

Abstract. We present a detailed analysis of the systematic errors that affect single-shot carrier envelope phase (CEP) measurements in experiments with long acquisition times, for which only limited long-term laser stability can be achieved. After introducing a scheme for eliminating these systematic errors to a large extent, we apply our approach to investigate the CEP dependence of the yield of doubly charged ions produced via non-sequential double ionization of argon in strong near-single-cycle laser pulses. The experimental results are compared to predictions of semiclassical calculations.

[8] Authors to whom any correspondence should be addressed.

Contents

1. Introduction

The electric field of a short laser pulse can be described as $E(t) = E_0 \cos^2(t/\tau) \cos(\omega t + \phi)$, where E_0 is the field amplitude, ω is the carrier frequency, τ is the pulse duration and ϕ is the carrier envelope phase (CEP). When the pulse duration enters the few-cycle regime, the value of the CEP strongly influences the temporal shape of the electric field. For frequencies in the visible range, the control of the CEP allows shaping the electric field waveform on attosecond timescales [1, 2] and allows efficiently control of ultrafast strong-field-driven electron dynamics [3–5].

Except for some intrinsically CEP-stable optical parametric chirped pulse amplification systems [6], where the CEP was demonstrated to remain stable for many hours [7], the CEP of pulses generated in few-cycle laser systems that are not actively CEP stabilized is changing from pulse to pulse, impeding exact knowledge of the temporal shape of the electric field $E(t)$. Stabilization of the CEP usually involves feedback loops to actively control the dispersion inside the laser oscillator [8]. Such active stabilization schemes, however, are very sensitive to small drifts in the laser parameters, and only practicable for a few hours, thus precluding measurements with long acquisition times.

A way around the difficulties related to active CEP stabilization is the recently introduced single-shot phase-tagging technique [9–11], where instead of being stabilized the CEP is measured for every single laser shot. In this way, each laser pulse and all physical quantities measured synchronously on a single-shot basis can be tagged with the CEP of the pulse. Recently, the combination of phase tagging with a coincidence spectroscopy technique [12] allowed the gaining of new insights into the attosecond dynamics of the non-sequential double ionization (NSDI) of argon atoms exposed to few-cycle [13] and near-single-cycle [14] laser pulses. NSDI of atoms [15] is characterized by the correlated emission of two electrons. According to the present understanding, a first electron liberated from the atom via tunnel ionization triggers the ionization of a second electron by laser-induced recollision with the parent ion. While the intensity dependence of NSDI yields in the long pulse regime has been investigated in numerous experimental and theoretical studies [15], only a limited number of experimental [12] and theoretical [16, 17] studies have addressed the CEP dependence of the total NSDI yield. The results of [16] indicate that the CEP dependence of the NSDI yield increases with the peak intensity of the laser. However, a more recent work [17] based on the

use of refined inelastic scattering cross-section predicts a decrease of the CEP dependence with increasing intensity. Both theoretical studies are in reasonable agreement with the experimental data at about 1.8×10^{14} W cm^{-2} reported by Johnson *et al* [12]. From the experimental point of view, the precision of this initial measurement [12] was limited by unavoidable long-term drifts of the laser parameters such as peak intensity, beam pointing or beam profile. In the present study we show how CEP tagging is affected by such drifts and quantify the systematic errors they introduce to the measurement. We then present a scheme for minimizing the effects of slow laser drifts and apply it to re-inspect the experimental results of [12] and further investigate the CEP dependence of the NSDI yield from argon as a function of intensity.

2. Experimental approach

The experimental setup used in the present study is described in detail in [12]. Briefly, linearly polarized near-single-cycle laser pulses (full-width at half-maximum of the intensity envelope of 4 fs) with a carrier wavelength of 750 nm are generated at a repetition rate of 3 kHz or 10 kHz in an amplified laser system [18].

A fraction of the laser beam is focused with a spherical mirror ($f = 25$ cm) into a cold supersonic gas jet of argon atoms in the center of a reaction microscope (REMI) [19]. Ions and electrons generated in the laser focus are directed by weak electric and magnetic fields towards time- and position-sensitive detectors on either side of the REMI. The 3D momentum vectors of the fragments are reconstructed from their time of flight (TOF) and impact position on the detectors.

Another fraction of the laser beam (25 μJ) is focused into a single-shot stereographic above-threshold ionization (Stereo-ATI) phase-meter [9]. There the TOF spectra of electrons produced via above-threshold ionization of xenon are recorded to the left and right of the focus along the laser polarization direction. The CEP is inferred from the asymmetry between the left and the right TOF spectra. The basic principle of CEP retrieval is illustrated in figure 1. A more detailed description of the stereo-ATI phase-meter can be found in [20] and references therein. In figure 1(a), the left–right asymmetry of the photoelectron yield is plotted as a function of TOF and CEP. In the stereo-ATI phase-meter the ionization yield is integrated over two regions R_x and R_y (denoted by the dashed lines in figure 1(a)) of the left and right TOF spectra to calculate the asymmetries $A_{x/y}$ for each region $R_{x/y}$ as

$$A_{x/y} = \frac{N_{\mathrm{left},x/y} - N_{\mathrm{right},x/y}}{N_{\mathrm{left},x/y} + N_{\mathrm{right},x/y}}. \tag{1}$$

Here, $N_{\mathrm{left},x/y}$ ($N_{\mathrm{right},x/y}$) are the photoelectron yields in the left (right) TOF spectrum integrated over $R_{x/y}$. Plotting A_y versus A_x yields the parametric asymmetry plot (PAP) shown in figure 1(c). The polar angle θ in the PAP defined as $\theta = \arctan(A_y/A_x)$ is related to the CEP ϕ via a continuous monotonic function $\phi(\theta)$. The function $\phi(\theta)$ is determined using the fact that the CEP of laser pulses from a kHz pulse train is uniformly randomly distributed when the laser is not CEP-locked [21]. In practice, the polar angle θ of a PAP with N entries is discretized to form b intervals $[\theta_k, \theta_k + \Delta(\theta_k)]$, each containing the same number $n = N/b$ of entries. The discrete angles θ_k are calculated as $\theta_k = \arctan(A_{y,k}/A_{x,k})$, where $(A_{x,k}, A_{y,k})$ are the coordinates of the entry with the smallest angle θ in the interval k. By construction, the steps $\Delta(\theta_k) = \theta_{k+1} - \theta_k$ correspond to equidistant steps $\Delta\phi$ in CEP. Finally, the continuous function

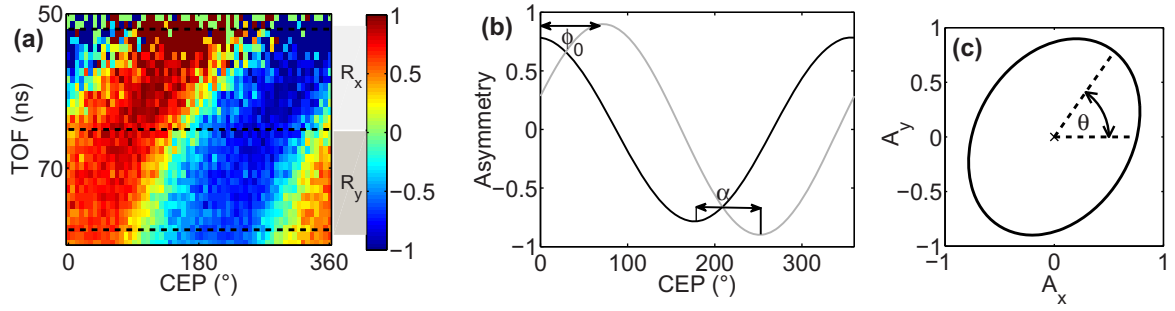

Figure 1. (a) Example of an asymmetry map obtained by plotting the left–right asymmetry of the single ionization yield of a rare gas as a function of TOF and CEP. In this specific example we present a REMI measurement of argon exposed to 4 fs laser pulses with a peak intensity of $(2.6 \pm 0.4) \times 10^{14}\,\mathrm{W\,cm^{-2}}$. Replacing argon by xenon would lead to qualitatively very similar results. The dashed lines mark the two TOF regions R_x and R_y over which the ionization yields in the left and right TOF spectra are integrated to calculate the CEP-dependent asymmetries A_x and A_y plotted as gray and black curves in panel (b), respectively. The parameter α denotes the phase shift between the two asymmetry curves A_x and A_y and ϕ_0 denotes the common phase offsets of A_x and A_y. Plotting A_y versus A_x for all CEPs yields the PAP shown in panel (c).

$\phi(\theta)$ is obtained by interpolation of the values $\phi(\theta_k) = k2\pi/b$. Note that the CEP measured with the stereo-ATI phase-meter is only determined up to a constant offset [20].

3. Effect of slow laser parameter drifts on carrier envelope phase measurements

In order to avoid saturation of the data acquisition system, only the data from laser pulses leading to a detected ionization event in the REMI were acquired. In the initial experiment [12], the function $\phi(\theta)$, relating the polar angle of the PAP to the CEP, was determined using a reference PAP, i.e. a PAP recorded independently of the REMI data acquisition just before the beginning of the experiment. This prevents any bias of the function $\phi(\theta)$ by our trigger scheme. NSDI events in this initial experiment were recorded over 3.5 h. In experiments with much longer acquisition times, slow drifts of the laser parameters, unaccounted for by the single reference PAP scheme, become problematic as they lead to distortions of the PAP. In order to discuss the distortions of the PAP we introduce the phase density

$$\rho(\phi) = \frac{2\pi}{N_0}\frac{\mathrm{d}N(\phi)}{\mathrm{d}\phi}, \tag{2}$$

where $N(\phi)$ is the number of laser shots with a CEP ϕ in $[\phi, \phi + \mathrm{d}\phi]$ measured by the stereo-ATI phase-meter and N_0 is the total number of laser shots. Equivalently, the $\rho(\phi)$ can be calculated as

$$\rho(\phi) = \left(\frac{\mathrm{d}\phi_{\mathrm{ref}}(\theta)}{\mathrm{d}\theta}\right)^{-1}\frac{\mathrm{d}\phi(\theta)}{\mathrm{d}\theta}, \tag{3}$$

where $\phi_{\mathrm{ref}}(\theta)$ was determined using a reference PAP measured at the beginning of the experiment. For non-CEP-locked pulses, a constant phase density of $\rho(\phi) = 1$ is expected in

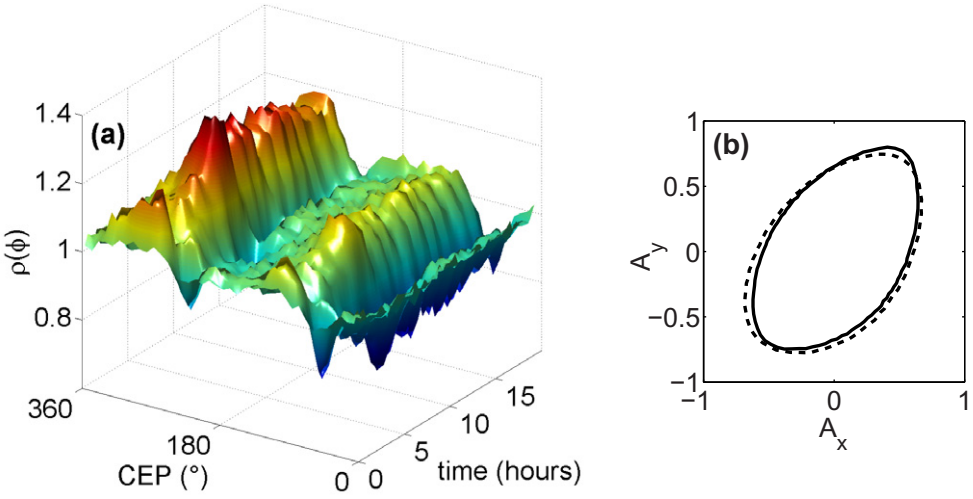

Figure 2. (a) Evolution of the phase density over the course of 19 h. The changes in the shape of the PAP with time are reflected by the appearance of inhomogeneities in the phase density. (b) The PAP measured by the stereo-ATI phase-meter at the beginning (solid) and the end (dashed) of the experiment. Here, the angle and radius were averaged over 200 adjacent points.

an ideal experiment. Drifts of the laser parameters, however, introduce modulations of the measured phase density as demonstrated in figure 2, where we show the evolution of $\rho(\phi)$ over the course of an experiment lasting 19 h (amounting to about 2×10^8 laser shots). The phase density is not constant over time and exhibits strong deviations from 1 even though these changes correspond to only small variations in the shape of the PAP as shown in figure 2(b), where a PAP with 20 000 laser shots is displayed at the beginning and the end of the experiment. The observed modulations of $\rho(\phi)$ are likely to be caused by variations of the laser intensity.

In order to quantitatively investigate how distortions of the PAP affect the CEP measurement, we describe the asymmetries $A_x(\phi)$ and $A_y(\phi)$ by

$$(A_x(\phi), A_y(\phi)) = (a_x \cos(\phi + \phi_0), a_y \cos(\phi + \phi_0 + \alpha)), \tag{4}$$

which is a parametric equation of an ellipse centered at the origin. Changes of the laser parameters affect not only the asymmetry amplitudes a_x and a_y but also the parameters ϕ_0 and α. This is illustrated in figure 3(a), where schematic asymmetry maps are shown for two laser intensities. The maxima (red) and minima (blue) of the asymmetry are displayed as a function of TOF (solid line for the lower intensity and dashed line for the higher intensity). While a change in the CEP offset ϕ_0 affects the phase tagging of the quantities measured in the experiment, it has no effect on the shape of the PAP, so it cannot be determined from the PAP alone. Any laser parameter drift will thus result in a transformation of the initial PAP into another ellipse centered at the origin with $(-1 \leqslant A_x, A_y \leqslant 1)$.

To give a concrete example, we simulate the effect of parameter drifts that correspond to realistic experimental conditions. In the first step we calculate an initial PAP (blue dots in figure 3(b)) using the parameters $a_x = 0.75$, $a_y = 0.85$, $\alpha = 67^\circ$ and a set of uniformly distributed CEP values ϕ_k $(k = 1, \ldots, 360)$. The conversion function $\phi(\theta)$ is determined from

$$\theta_k = \arctan\left(\frac{A_y(\phi_k)}{A_x(\phi_k)}\right).$$

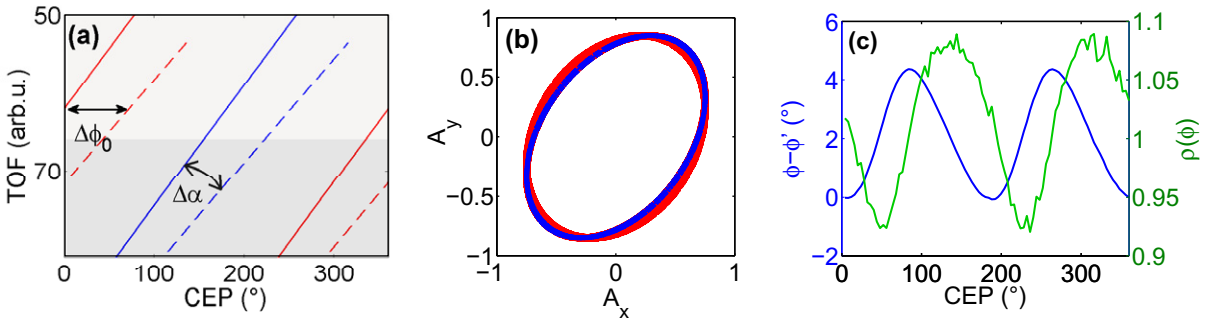

Figure 3. Illustration of the effect of intensity drifts on the CEP measurement. (a) Schematic asymmetry maps of ionization yields for two different intensities. The solid (higher intensity) and dashed (lower intensity) lines indicate the maxima (red) and minima (blue) of the asymmetry. The shaded areas represent the two TOF regions R_x, R_y used to calculate the asymmetries A_x and A_y. $\Delta\phi_0$ denotes the shift of the parameter ϕ_0 induced by an intensity change in the stereo-ATI phase-meter. The notation $\Delta\alpha$ indicates the change in slope between the solid and dashed lines that is causing a variation of α. (b) Simulated set of distorted PAPs (red). The initial (reference) PAP is shown in blue. The variations of the parameters a_x, a_y and α (defined in the text) used to calculate the distorted PAPs were inferred from experimental data where the intensity slowly decreased by 7%. (c) The CEP error and the resulting phase density for the distorted PAP when the conversion function $\phi(\theta)$ is determined from the reference PAP of panel (b).

In the next step, modified PAPs (red dots in figure 3(b)) are calculated by gradually changing the PAP parameters to $a'_x = 0.79$, $a'_y = 0.89$ and $\alpha' = 75°$. Applying $\phi(\theta)$ to the polar angles

$$\theta'_k = \arctan\left(\frac{A'_y(\phi_k)}{A'_x(\phi_k)}\right)$$

obtained from the modified PAP yields the apparent CEP $\phi'_k = \phi(\theta'_k)$.

Figure 3(c) shows the CEP error $\Delta\phi_k = \phi'_k - \phi_k$ (blue line) and the phase density $\rho(\phi'_k)$ (green line) of the modulated PAP as a function of ϕ_k. The error $\Delta\phi_k$ oscillates around a generally non-zero value but remains of the order of only a few degrees. In contrast, these relatively small distortions of the PAP strongly affect the phase density. The apparent yield $Y'_X(\phi)$ of ions of the species X relates to $\rho(\phi)$ as

$$Y'_X(\phi) = Y_X(\phi)\rho(\phi),$$

where $Y_X(\phi)$ is the true (CEP-dependent) ionization yield of X. Therefore, the relative error of the measured CEP-dependent ionization yield is

$$\frac{\Delta Y_X(\phi)}{Y_X(\phi)} = \rho(\phi) - 1.$$

The retrieval of CEP dependences of ionization yields thus requires $\rho(\phi) - 1$ to be much smaller than the expected modulations of $Y_X(\phi)$. To demonstrate how modulations of $\rho(\phi)$ can hamper the measurements of $Y_X(\phi)$, the apparent CEP-dependent yield $Y'_{Ar^+}(\phi)$ of Ar^+ ions measured in our experiment is shown along with the calculated CEP dependence of the Ar^+ yield in figure 4.

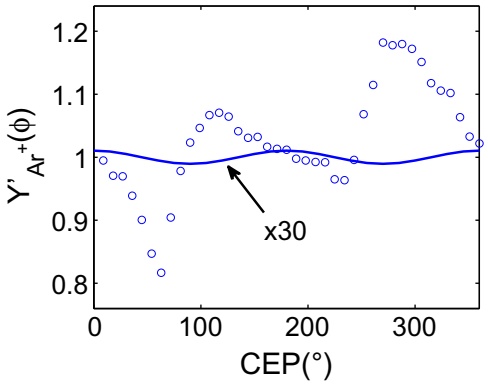

Figure 4. Apparent CEP-dependent yield of Ar^+ ions generated in 4 fs laser pulses with a central wavelength of 750 nm and a peak intensity of 3.0×10^{14} W cm^{-2} (open circles). The solid line represents the calculated CEP dependence of the Ar^+ yield for the experimental laser parameters using a semi-classical approach. For visual convenience, the modulations of the predicted curve are multiplied by a factor of 30.

A solution to minimize the modulations of $\rho(\phi)$ is provided by updating the function $\phi(\theta)$ in sufficiently small time intervals throughout the measurement. Based on the results of our calculations we neglect the CEP dependence of the single ionization yield of argon and use the subset of laser shots for which an Ar^+ ion was detected to update $\phi(\theta)$. In the present case, $\phi(\theta)$ was updated every 30 min each time using 1 million laser shots.

Although updating $\phi(\theta)$ reduces the modulations of $\rho(\phi)$ to a large extent, this scheme cannot correct for the shift $\Delta\phi_0$ of the CEP offset. In our experiment we measure a new asymmetry curve for Ar^+ every 30 min and observe CEP shifts of a few degrees between two such curves. Similarly to the phase density, the shifts of the CEP evolve over the course of hours and reach values up to 10° in the present experiment. Using the Ar^+ asymmetry curves measured at regular time intervals during the experiment, CEP offset variations can be corrected.

We would like to remark that our method can be applied to reduce the impact of laser fluctuations with frequencies smaller than 0.1 Hz. A stabilization scheme such as that demonstrated in [22] would allow one to further improve the precision of CEP tagging by reducing the effects caused by much faster power fluctuations.

4. Carrier envelope phase dependence of the non-sequential double ionization yield

The strength of our improved analysis is demonstrated in figure 5, where we compare CEP-dependent yields of doubly charged argon ions obtained with (green crosses) and without (red line) a continuous update of the function $\phi(\theta)$. It can be clearly seen that for the data presented in figure 5(a), recorded over 19 h, the improved analysis becomes indispensable for obtaining a meaningful result. The result of the new analysis of the data obtained in the initial proof-of-principle experiment [12] is shown in figure 5(b). Since the Ar^+ ions were not recorded in that experiment, we used the background of singly ionized H_2O to update the function $\phi(\theta)$. Because the data were acquired for only 3.5 h, there is still qualitative agreement between the results of both analyses. However, even for this rather short acquisition time, systematic errors in the CEP

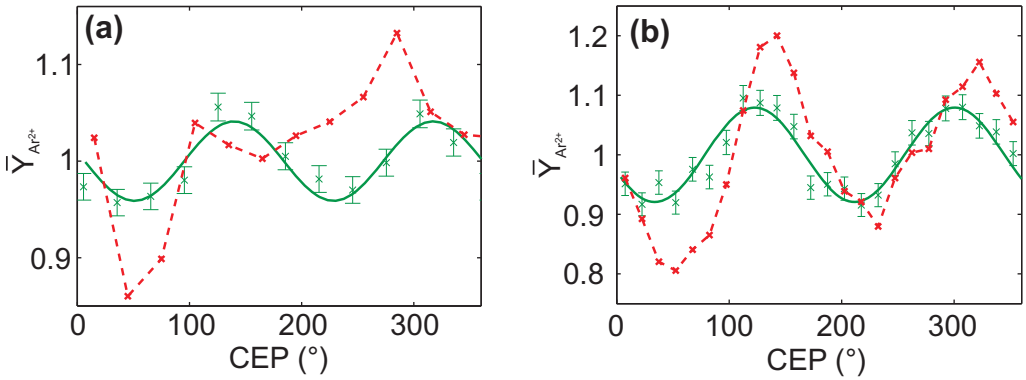

Figure 5. CEP-dependent yields of doubly charged argon ions obtained with (green crosses) and without (red line) a continuous update of the function $\phi(\theta)$. The solid green lines represent a sinusoidal model function: $\overline{Y}_{Ar^{2+}}(\phi) = 1 + A_{NSDI} \sin(\phi + \phi_Y)$, where ϕ_Y is a CEP offset and A_{NSDI} is the modulation amplitude of the oscillation. (a) For the 19 h long measurement described in the text. (b) For the data from [12]. The red line represents the Ar^{2+} yield obtained by the previous (uncorrected) analysis.

measurement considerably affect the experimental result, precluding a quantitative comparison with theoretical results. With our improved analysis these errors can now be eliminated to a large extent. The results of both experiments indicate that for both the presented data sets, the modulation of the normalized NSDI yield

$$\overline{Y}_{Ar^{2+}}(\phi) = Y_{Ar^{2+}}(\phi)\, 2\pi \left(\int Y_{Ar^{2+}}(\phi) \mathrm{d}\phi \right)^{-1} \tag{5}$$

is consistent with sinusoidal model functions

$$\overline{Y}_{Ar^{2+}}(\phi) = 1 + A_{NSDI} \sin(\phi + \phi_Y)\,, \tag{6}$$

where ϕ_Y is a CEP offset and A_{NSDI} is the modulation amplitude of the oscillation.

Modulation amplitudes of (4.8 ± 0.8) and $(8.0 \pm 0.6)\%$ are found for the CEP-dependent yield shown in figures 5(a) and (b), respectively.

In the following, we apply our new scheme to investigate the dependence of A_{NSDI} on the laser intensity.

In figure 6, we compare the measured values for A_{NSDI} obtained from the double ionization of argon with 4 fs laser pulses at intensities ranging from about 0.2 to 0.4 PW cm^{-2} with the predictions of semiclassical calculations that are described in the appendix. The peak intensity of the laser pulses was determined from the width of the Ar^+ momentum spectra. In the intensity range under study, we clearly observe a decrease of A_{NSDI} with increasing intensity up to about 4×10^{14} W cm^{-2} where no significant CEP dependence of the NSDI yield was observed. Our experimental results and calculations thus confirm the predictions reported in [17]. While our model correctly predicts the slope of the intensity-dependent modulation amplitude A_{NSDI}, the absolute values for A_{NSDI} differ from the measured ones by a constant offset of about 5%. While at first glance the discrepancy would also be explained by a systematic underestimation of the measured intensity, we believe that this hypothesis is rather unlikely. Instead, it is more probable

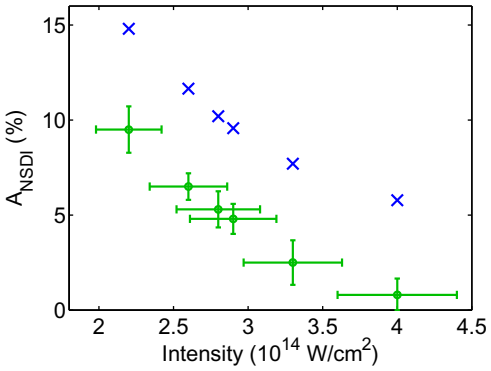

Figure 6. Measured (green dots) and calculated (blue crosses) CEP-induced modulation amplitudes A_{NSDI} of the NSDI yield of Ar in 4 fs laser fields of different intensities. Each point represents the ratio of the amplitude of the modulation to the CEP-averaged NSDI yield at a specific intensity. The y-errors are statistical error bars of the NSDI yield modulations. The x-error is an estimated 10% uncertainty in the intensity determination.

that the disagreement is due to the limitations of the semiclassical model. Further investigations are required to elucidate the exact reasons for the observed discrepancies.

5. Conclusion

In conclusion, we have presented a detailed analysis of systematic errors in single-shot CEP measurements with a stereo-ATI phase-meter. We demonstrated that these errors, which are essentially due to slow drifts of the laser intensity, can dramatically affect the results of phase-tagged ionization yield measurements with long acquisition times. We showed how these systematic errors can be eliminated to a large extent in spite of the unavoidable slow drifts of the laser parameters and applied our new scheme to retrieve the accurate CEP dependence of the total NSDI yield of argon at various intensities. While the measured intensity dependence of the CEP-induced modulation amplitude is qualitatively reproduced by our classical calculations, more involved theoretical models are certainly needed to reach quantitative agreement with the experimental data.

Acknowledgments

We acknowledge Ferenc Krausz for his support and for making specialized equipment available to us. We are grateful for support from the DFG via Kl-1439/2, Kl-1439/3, Kl-1439/5 and the Cluster of Excellence: Munich Center for Advanced Photonics (MAP). We acknowledge support from the EU via the ITN ATTOFEL and LaserLab Europe. NGJ and MFK were partially supported by the Chemical Sciences, Geosciences, and Biosciences Division, Office of Basic Energy Sciences, Office of Science, US Department of Energy under DE-FG02-86ER13491 and the National Science Foundation under CHE-0822646 and EPS-0903806.

Appendix. Theoretical modeling

The semiclassical calculations used for describing our experimental data are outlined in our previous study [14]. It was shown there that the experimental results for NSDI in argon are well described by the rescattering-induced excitation and subsequent ionization mechanism. Briefly, tunnel ionization rates are calculated using a corrected Ammosov–Delone–Krainov (ADK) formula [24, 25] that adequately accounts for over-the-barrier ionization [23]:

$$w(t) = w_{\mathrm{ADK}}(t) \times \exp\left[-\alpha \frac{Z^2 E(t)}{I_{\mathrm{P}}(2I_{\mathrm{P}})^{3/2}}\right]. \tag{A.1}$$

Here, w_{ADK} is the instantaneous ADK rate, I_{P} the ionization potential, $E(t)$ the electric field of the laser, Z the charge of the parent ion and α a numerical factor adjusted such that the rate, $w(t)$, fits the result obtained by solving the Schrödinger equation numerically. The value of parameter α is 9 for Ar and 8 for Ar^+ [23]. After tunnel ionization at $t = t_0$, the electron is propagated as a free classical particle in the electric field of the laser. Upon recollision at $t = t_1$, the parent Ar^+ ion is assumed to be instantaneously excited to its lowest excited state, Ar^{+*}: $[Ne]3s^1 3p^6$, provided the recolliding electron carries enough energy for the excitation (13.5 eV). The electron energy dependence of the excitation cross-section is neglected. A second electron is then emitted from the excited ion in another tunneling process described by the corrected ADK formula using the appropriate parameters for the excited Ar^+ ($I_{\mathrm{P}} = 14.1$ eV, $Z = 2$, $\alpha = 8$) ion. The final momenta of the electrons are calculated for every initial ionization time t_0. The CEP-dependent single and double ionization yields of argon are obtained by performing the calculations for different CEPs. Focal volume averaging and depletion of the Ar and Ar^{+*} populations are taken into account.

References

[1] Krausz F and Ivanov M 2009 *Rev. Mod. Phys.* **81** 163–234
[2] Baltuška A *et al* 2003 *Nature* **421** 611–5
[3] Hentschel M, Kienberger R, Spielmann Ch, Reider G A, Milosevic N, Brabec T, Corkum P, Heinzmann U, Drescher M and Krausz F 2001 *Nature* **414** 509–13
[4] Kling M F and Vrakking M J J 2008 *Annu. Rev. Phys. Chem.* **59** 463–92
[5] Abel M, Neumark D M, Leone S R and Pfeifer T 2011 *Laser Photon. Rev.* **5** 352
[6] Baltuška A, Fuji T and Kobayashi T 2002 *Phys. Rev. Lett.* **88** 133901
[7] Bergues B, Zherebtsov S, Deng Y, Gu X, Znakovskaya I, Kienberger R, Krausz F, Marcus G and Kling M F 2011 *New J. Phys.* **13** 063010
[8] Udem T, Holzwarth R and Hänsch T W 2002 *Nature* **416** 233–7
[9] Wittmann T, Horvath B, Helml W, Schätzel M G, Gu X, Cavalieri A L, Paulus G G and Kienberger R 2009 *Nature Phys.* **5** 357–62
[10] Paulus G G, Grasbon F, Walther H, Villoresi P, Nisoli M, Stagira S, Priori E and Silvestri S De 2001 *Nature* **414** 182–4
[11] Paulus G G, Lindner F, Walther H, Baltuška A, Goulielmakis E, Lezius M and Krausz F. 2003 *Phys. Rev. Lett.* **91** 253004
[12] Johnson N G *et al* 2011 *Phys. Rev.* A **83** 013412
[13] Camus N *et al* 2012 *Phys. Rev. Lett.* **108** 073003
[14] Bergues B *et al* 2012 *Nature Commun.* **3** 813
[15] Figueira de Morisson Faria C and Liu X 2011 *J. Mod. Opt.* **58** 1076–131
[16] Micheau S, Chen Z, Le A T and Lin C D 2009 *Phys. Rev.* A **79** 013417

[17] Chen Z, Liang Y, Madison D H and Lin C D 2011 *Phys. Rev.* A **84** 023414
[18] Schultze M *et al* 2011 *J. Electron Spectrosc. Relat. Phenom.* **184** 68
[19] Ullrich J, Moshammer R, Dorn A, Dörner R, Schmidt L P H and Schmidt-Böcking H 2003 *Rep. Prog. Phys.* **66** 1463–545
[20] Rathje T, Johnson N G, Möller M, Süßmann F, Adolph D, Kübel M, Kienberger R, Kling M F, Paulus G G and Sayler A M 2012 *J. Phys. B: At. Mol. Opt. Phys.* **45** 074003
[21] Sayler A M, Rathje T, Müller W, Rühle K, Kienberger R and Paulus G G 2011 *Opt. Lett.* **36** 1–3
[22] Wang H, Li C, Tackett J, Mashiko H, Nakamura C M, Moon E and Chang Z 2007 *Appl. Phys.* B **89** 275–9
[23] Tong X M and Lin C D 2005 *J. Phys. B: At. Mol. Opt. Phys.* **38** 2593–600
[24] Ammosov M V, Delone N B and Krainov V P 1986 *Sov. Phys.—JETP* **64** 1191–4
[25] Perelomov A M, Popov V S and Terent'ev M V 1966 *Sov. Phys.—JETP* **23** 924–34

7.3. Publication III

M. Kübel, N. G. Kling, K. J. Betsch, N. Camus, A. Kaldun, U. Kleineberg, I. Ben-Itzhak, R. R. Jones, G. G. Paulus, T. Pfeifer, J. Ullrich, R. Moshammer, M. F. Kling, and B. Bergues, Nonsequential double ionization of N_2 in a near-single-cycle laser pulse. *Phys. Rev. A* **88**, 023418 (2013).

Having measured very similar correlation spectra for NSDI of Ar and N_2, we subjected both targets to a direct comparison. In this experiment, which ran for a staggering 69 hours, both particles were exposed to the same laser focus, alternating between the two gases approximately 20 times during the experiment. In all experiments for the paper, I was one of the leading experimentalists, performed the data analysis and simulations and contributed to the data interpretation and the writing of the manuscript.

Nonsequential double ionization of N_2 in a near-single-cycle laser pulse

M. Kübel,[1] Nora G. Kling,[1,2] K. J. Betsch,[1,2,3] N. Camus,[4] A. Kaldun,[4] U. Kleineberg,[5] I. Ben-Itzhak,[2] R. R. Jones,[3] G. G. Paulus,[6,7] T. Pfeifer,[4] J. Ullrich,[4,8] R. Moshammer,[4] M. F. Kling,[1,2,*] and B. Bergues[1,†]

[1]*Max-Planck-Institut für Quantenoptik, D-85748 Garching, Germany*
[2]*J. R. Macdonald Laboratory, Physics Department, Kansas State University, Manhattan, Kansas 66506, USA*
[3]*Department of Physics, University of Virginia, Charlottesville, Virginia 22904, USA*
[4]*Max-Planck-Institut für Kernphysik, D-69117 Heidelberg, Germany*
[5]*Department für Physik, Ludwig-Maximilians-Universität, D-85748 Garching, Germany*
[6]*Institut für Optik und Quantenelektronik, Friedrich-Schiller-Universität, D-07743 Jena, Germany*
[7]*Helmholtz Institut Jena, D-07743 Jena, Germany*
[8]*Physikalisch-Technische Bundesanstalt, D-38116 Braunschweig, Germany*

(Received 14 March 2013; published 22 August 2013)

We present a comparative study of nonsequential double ionization (NSDI) of N_2 and Ar exposed to near-single-cycle laser pulses. The NSDI process is investigated using carrier-envelope-phase-tagged electron-ion coincidence spectroscopy. The measured NSDI spectra of N_2 and Ar exhibit a striking resemblance. In particular, the correlated two-electron momentum distribution arising from NSDI of N_2 also displays a cross-shape very similar to that reported for Ar [Bergues *et al.*, Nat. Commun. **3**, 813 (2012)]. We interpret our results in terms of recollision-excitation with subcycle depletion and discuss how this mechanism accounts for the observed similarities and differences in the ionization behavior of the two species.

DOI: 10.1103/PhysRevA.88.023418 PACS number(s): 33.80.Rv, 32.80.Rm, 32.80.Wr, 33.80.Wz

I. INTRODUCTION

In nonsequential double ionization (NSDI) of an atom or molecule exposed to a strong laser field, the ionization acts of the first and second electrons are not independent from each other. Because it represents a prototypical example of multielectron dynamics driven, steered, and potentially controlled by an external field, NSDI of atoms and molecules has received considerable attention over the past four decades (for a recent review see [1]). Among different experimental techniques, including intensity-dependent ion-yield measurements [2,3], charge-state-resolved electron time-of-flight spectroscopy [4], and recoil-ion momentum spectroscopy [5], coincidence electron-ion recoil-momentum spectroscopy, where the momenta of electrons and ions are measured in coincidence [6], provides the most detailed information about the process. Besides NSDI in a strong field reported here, the study of NSDI has been extended to the extreme-ultraviolet-wavelength regime at free-electron lasers [7,8] and, recently, using time-resolved two-XUV-photon ionization spectroscopy with XUV radiation generated from a tabletop high-harmonic source [9].

While it is now well established that in NSDI the emission of the second electron is facilitated by the laser-driven recollision of the first electron with its parent ion, the exact mechanisms governing this recollision-induced ionization are not yet fully understood. One of the reasons is that in multicycle laser pulses, NSDI may involve multiple recollisions, which hamper the interpretation of experimental results and represent a great challenge for theoretical description. Owing to the advances in the production of ultrashort laser pulses [10–12], the problem of multiple recollisions can be largely avoided by driving NSDI with a carrier-envelope-phase (CEP) controlled near-single-cycle laser pulse to essentially confine the process to a single recollision event. While active CEP stabilization has allowed for recording the recoil-ion momentum spectrum of doubly charged Ar ions at various CEPs [13], measurements of the more instructive CEP-resolved electron correlation spectra were hindered in the past by the difficulty to keep the laser CEP stable over the entire acquisition time (on the order of 24 h) of such an experiment. The use of single-shot CEP tagging [14,15] has recently permitted overcoming those limitations and enabled the detailed investigation of NSDI of Ar in the near-single-cycle [16] and the few-cycle [17] regimes.

In the present study, we pioneer NSDI in a single laser cycle for diatomic molecules, where N_2 serves as a test case. The first and second ionization potentials of N_2 ($I_P^I = 15.58$ eV and $I_P^{II} = 27.12$ eV) are very close to those of Ar ($I_P^I = 15.76$ eV and $I_P^{II} = 27.63$ eV), and similarities in the ionization behavior, particularly NSDI, of the two species have been reported in numerous studies [18–22]. The fact that those similarities are not observed for all atom-molecule pairs with nearly equal ionization potentials (such as, for instance, Xe and O_2) [19–21] provides evidence, however, that this criterion is not sufficient to explain the resemblance in the ionization behavior.

Only a few studies so far have addressed this question for N_2 and Ar using highly differential experimental methods [23]. Coincidence spectra of Ar and N_2 have been recorded in the multicycle regime by Eremina *et al.* in Refs. [24,25], respectively. In both measurements, electrons were preferentially emitted with the same kinetic energy. While for most of the electron pairs the momenta point in the same direction, in a small part of the signal, the electrons are emitted with anticorrelated momenta. In a study with similar laser parameters, Zeidler *et al.* demonstrated that the ratio of anticorrelated to correlated electrons can be controlled to some extent via the molecular alignment [26].

*matthias.kling@mpq.mpg.de
†boris.bergues@mpq.mpg.de

It was shown recently that for NSDI of Ar, the transition to the single-cycle regime leads to dramatically different correlation spectra. There, the two electrons exhibit totally asymmetric rather than totally symmetric energy sharing, resulting in a characteristic cross-shaped pattern in the correlation momentum spectrum [16]. The theoretical interpretation of this experiment involves electron impact excitation of the Ar^+ ion [16]. Since the excited-state spectra of Ar^+ and N_2^+ are significantly different from each other (the lowest excited energy of Ar^+ is 13.5 eV above the ground state, while N_2^+ has several excited states at much lower energy; see, e.g., [27,28]), there is no obvious reason to expect strong similarities between the two-electron momentum distributions of both species. In fact, recent predictions from quantum-mechanical [29,30] as well as classical-ensemble [31] calculations indicate that, in contrast to Ar [32,33], symmetric energy sharing between the electrons should be expected for NSDI of N_2 in a near-single-cycle laser pulse (for a recent review about theoretical approaches to NSDI see [34]). Here, we elucidate this question experimentally and show that, in spite of the significant differences in the excited-state spectra of the Ar^+ and N_2^+ ions, the CEP-resolved electron correlation spectra of Ar and N_2 exhibit striking similarities.

II. EXPERIMENTAL SETUP

A detailed description of the experimental setup has been given in earlier publications [16,35]. Briefly, near-single-cycle, linearly polarized laser pulses with a central wavelength of 750 nm are generated at a repetition rate of 3 kHz by a short-pulse laser system [36]. The laser beam is split into two parts. The first part is focused into a cold supersonic gas jet inside a reaction microscope (REMI) [37], where the momenta of ions and electrons arising from ionization of a target atom (or molecule) in the laser focus are measured in coincidence. The second part of the laser beam is sent to a single-shot stereo-ATI phase meter [14,15], facilitating the CEP tagging of the data recorded with the REMI as detailed in Ref. [38].

III. RESULTS AND DISCUSSION

In order to provide a solid basis for the comparison of the NSDI process in Ar and N_2, we alternately exposed both targets to the same laser focus and recorded the CEP-dependent recoil-ion momentum spectra of singly and doubly charged ions generated in the interaction region. The peak intensity in the focus was determined to be $I_0 = 3.6 \times 10^{14}$ W cm^{-2} by fitting the measured recoil-ion momentum distributions of Ar^+ with the semiclassical model described below. The yield ratios of Ar^{2+} to Ar^+ and N_2^{2+} to N_2^+ were 0.26% and 0.07%, respectively. This difference cannot be explained by double-ionization events occurring via dissociative channels alone since these represent less than 20% of the N_2^+ count, as estimated from the recorded N^+ fragments. The CEP-dependent modulations of the NSDI yield relative to the CEP-averaged yield (as defined in Ref. [38]) were 5.1% ± 0.5% and 4.2% ± 0.4% for Ar and N_2, respectively.

The CEP-dependent momentum spectrum of the Ar^{2+} and N_2^{2+} ions along the polarization axis are shown in Figs. 1(a) and 1(b), respectively. Both spectra exhibit a pronounced CEP-dependent asymmetry in the emission direction of the doubly charged ions and are hardly distinguishable from each other. Only a closer inspection shows that the islands in the N_2^{2+} spectrum extend slightly further towards smaller momentum values than the corresponding Ar^{2+} islands.

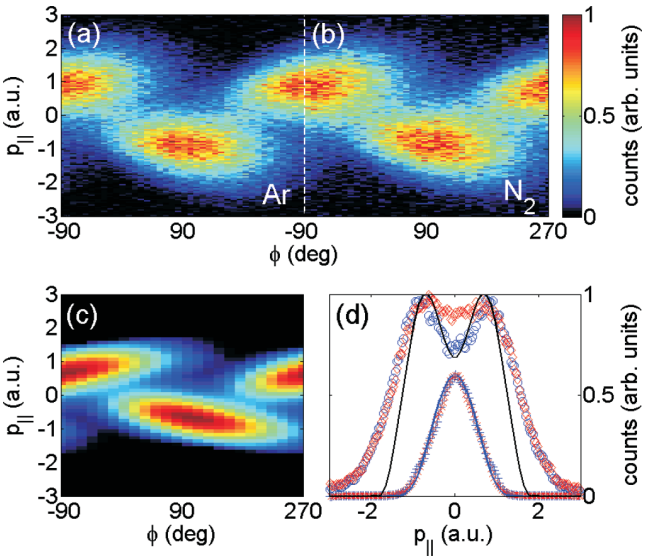

FIG. 1. (Color online) Measured CEP dependence of the recoil-ion momentum distribution along the laser polarization axis: (a) for Ar^{2+} and (b) for N_2^{2+}. The ions were generated in the same laser focus at a peak intensity of $I_0 = 3.6 \times 10^{14}$ W cm^{-2}. Invariance under the symmetry transformation $(p,\phi) \rightarrow (-p,\phi+\pi)$ was used to symmetrize the experimental images. (c) Calculated CEP-dependent $p_{||}$ distributions of Ar^{2+} using the semiclassical model described in the text. The undetermined CEP offset in the experimental data was chosen such that measured and calculated doubly charged ion spectra oscillate in phase. (d) Measured momentum spectra of Ar^+ (blue pluses), N_2^+ (red crosses), Ar^{2+} (blue circles), and N_2^{2+} (red diamonds), averaged over CEP, shown together with predictions for the Ar^+ spectrum [blue (gray) solid line] and the Ar^{2+} spectrum (black solid line). The maxima of the doubly charged ion spectra are normalized to 1, and the spectra of the singly charged ions are normalized to 0.6 for visual convenience. The statistical uncertainty of the measured data is of the order of the marker size.

For the discussion of the mechanisms that govern NSDI of N_2 and Ar, it is instructive to compare the experimental results to predictions of a semiclassical NSDI model for Ar. The model, which was described in detail in Ref. [16], builds on recollisional excitation with subsequent ionization (RESI) [39,40]. In RESI, the recolliding electron excites the parent ion, which is then further ionized by the laser field. In the calculation we assume that the main contribution comes from RESI via the lowest-lying excited state of Ar. Just after the recollision, the magnitude of the momentum of the recolliding electron is determined by energy conservation, while its direction, i.e., the angle between the momentum vectors just before and just after the recollision, is described by a free parameter, β, in our model. The dependence of the simulation results on β was discussed in Ref. [16]. The best agreement is found for $\beta = 25°$. Depletion of the bound-state population as well as the intensity distribution over the focal volume are taken into account in the calculations.

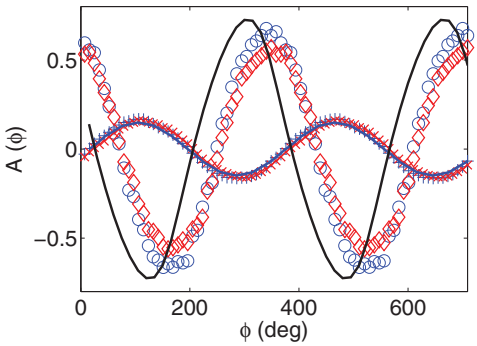

FIG. 2. (Color online) CEP-dependent asymmetries for Ar^+ (blue pluses), N_2^+ (red crosses), Ar^{2+} (blue circles), and N_2^{2+} (red diamonds), shown together with predictions for the Ar^+ asymmetry [blue (gray) solid line] and the Ar^{2+} asymmetry (black solid line). The undetermined CEP offset in the experimental data was chosen such that the asymmetries of the measured and the calculated Ar^+ spectra oscillate in phase. The statistical uncertainty of the measured data is of the order of the marker size.

The calculated CEP-resolved momentum spectrum of Ar^{2+} is displayed in Fig. 1(c). While the simulation qualitatively reproduces the experimental result, the signal in the measured Ar^{2+} spectrum extends to somewhat higher momenta than in its calculated counterpart. As discussed in Ref. [16], this is probably due to small contributions from higher excited states of Ar^+ that are neglected in the present model. To compare the spectra more quantitatively, in Fig. 1(d) we plot the CEP-averaged Ar^{2+} and N_2^{2+} spectra together with the CEP-averaged spectra of the simultaneously recorded Ar^+ and N_2^+ ions and the predictions of the model for Ar. Within the resolution of the measurement (of about 0.1 a.u.), the Ar^+ and N_2^+ spectra lie essentially on top of each other. The Ar^{2+} and N_2^{2+} momentum distributions, in contrast, differ by about 10%, around $p_{||} = 0$. The measured and calculated Ar^{2+} spectra have a pronounced dip, while the central part of the N_2^{2+} spectrum is rather flat.

In order to discuss the CEP dependence in more detail, the CEP-dependent asymmetries in the singly and doubly charged ion spectra of Ar and N_2 are compared in Fig. 2. The asymmetry $A(\phi)$ is defined as $A(\phi) = [N_+(\phi) - N_-(\phi)]/[N_+(\phi) + N_-(\phi)]$, where, for a given CEP ϕ, $N_-(\phi)$ $[N_+(\phi)]$ are the number of ions with a negative (positive) momentum component along the polarization axis. The CEP-dependent asymmetry can be approximated by $A(\phi) = A_0 \sin(\phi + \phi_0)$, where A_0 is the asymmetry amplitude and ϕ_0 is an offset phase. Since all the ions were recorded simultaneously, the phase shifts between the different asymmetry curves are meaningful quantities. Note that this is not the case for data recorded in separate experiments since the CEP is measured up to a constant but unknown offset, which depends on the specific conditions of the experiment. One can see that the asymmetry curves of Ar^+ and N_2^+ coincide perfectly in amplitude and phase. While those for Ar^{2+} and N_2^{2+} oscillate in phase with each other, the amplitude of the N_2^{2+} asymmetry curve is slightly smaller than for the case of Ar^{2+}. While the measured asymmetry amplitude for Ar^+ is well reproduced by the semiclassical model, the asymmetry for Ar^{2+} is overestimated by 10%. The predicted phase shift of 165° between the Ar^{2+} and Ar^+ asymmetry curves differs from the measured value of 125°. As discussed in Ref. [16], quantitative agreement would require a more sophisticated theory.

In order to measure electron correlation spectra of NSDI of N_2, data were collected over 48 hours at a focal peak intensity

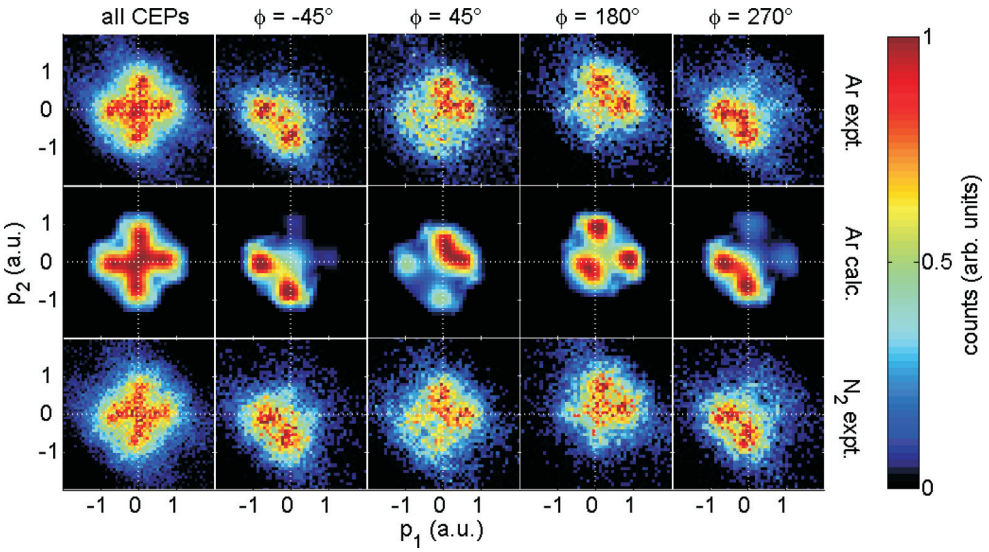

FIG. 3. (Color online) Experimental two-electron momentum distributions showing the correlated momenta along the laser polarization axis of the first (p_1) and second (p_2) electrons emitted from Ar^{2+} (top row) or N_2^{2+} (bottom row) and the corresponding predictions for Ar (middle row) at the peak intensity $I_0 = 3.2 \times 10^{14}$ W cm^{-2}. The CEP-averaged results are displayed in the left column. In the second through fifth columns, the correlation spectra are shown for CEP values of −45°, 45°, 180°, and 270°, respectively. The signal in each image is averaged over a CEP range of ±22.5° and normalized to its maximum value. The undetermined CEP offset in the experimental data was chosen such that measured and calculated doubly charged ion spectra oscillate in phase. Invariance under the symmetry transformation $(p,\phi) \rightarrow (-p,\phi + \pi)$ and the symmetry with respect to the $p_2 = p_1$ diagonal were used to symmetrize the experimental images.

of $I_0 = 3.2 \times 10^{14}$ W cm^{-2}. The total count rate was kept low (0.2 ions per laser shot) in order to decrease the contribution of false coincidences to less than 15% of the measured signal. Under the experimental conditions of this measurement, the ratio of the measured yields of N_2^{2+} and N_2^+ ions was 0.05%. The data are compared to correlation spectra of NSDI of Ar recorded in a separate experiment under similar conditions and at essentially the same peak intensity. The ratio of the Ar^{2+} and Ar^+ yields in this measurement was 0.13%.

The measured two-electron momentum distributions from NSDI of Ar and N_2 are presented in Fig. 3 together with the predictions of the NSDI model for Ar. The experimental correlation spectra are generated by considering the laser shots where at least one electron and one Ar^{2+} (or N_2^{2+}) ion were detected. Since one of the two NSDI electrons is frequently missing because of the limited single-particle detection efficiency of about 50%, the momentum of the missing electron is calculated as the negative momentum sum of the dication and the detected electron. All the measured and the simulated CEP-averaged correlation spectra shown in Figs. 3(a), 3(b), and 3(c) exhibit a fairly similar crosslike structure. The dependence of the two-electron momentum distributions on the CEP is shown in the second through fifth columns for CEP values of 135°, 225°, 0°, and 90°, respectively. Here, again, it can be seen that all three series of spectra exhibit qualitatively the same features.

The comparison of the measured and simulated correlation spectra for Ar confirms the results of Ref. [16] that were obtained at a slightly lower intensity. The pronounced maxima along the momentum axes at ±0.7 a.u. are well reproduced by the calculation. The essentially asymmetric energy sharing observed in the measured correlation spectra of N_2 [Fig. 3(c)] strongly contrasts with the results reported in previous experimental studies using longer pulses [25,26]. Although it is very similar to the measured correlation spectrum of Ar [Fig. 3(a)], the correlation spectrum of N_2 slightly differs by contributions of low-energy anticorrelated electrons, leading to the flat top of the N_2^{2+} spectrum. Together with the disparity in the measured double- to single-ionization yield ratios, this constitutes the main difference observed between NSDI of Ar and N_2.

The reason for the asymmetric energy sharing of NSDI electrons in Ar was discussed in detail in Ref. [16]. Subcycle depletion of the excited-state population in the course of the RESI process was shown to govern the moment of the second-electron release on a subcycle time scale. The instant of emission, in turn, determines the momentum that the electron gains in the laser field. The strong resemblance between the correlation spectra of Ar and N_2 suggests that the same mechanism should also apply for NSDI of N_2. A crucial difference between recollision excitation of Ar and N_2, however, is the existence of excited states in N_2^+ with energies ranging well below that of the lowest excited state of Ar^+.

In order to investigate the role of such lower-lying excited states, we considered in our model for Ar the contribution

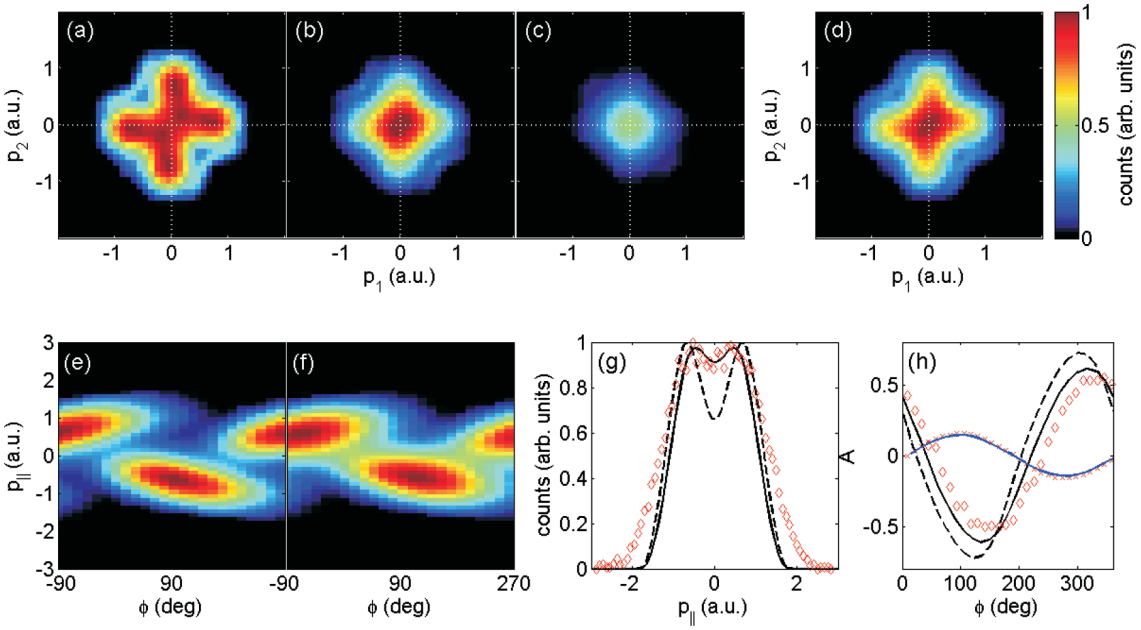

FIG. 4. (Color online) Contribution of (a) the lowest excited state of Ar^+ with an excitation energy of 13.5 eV and two additional fictitious states with excitation energies of (b) 11.5 and (c) 9.5 eV to the correlation spectrum. (d) Sum of the contributions in (a), (b) and (c) normalized to 1. The excitation probability by an electron with a kinetic energy greater than the excitation energy is assumed to be equal for all three states. Comparison of the calculated CEP-resolved momentum spectra of the doubly charged ions (e) without and (f) with the contribution of the two lower-lying states. The corresponding CEP-averaged spectra and the asymmetry curves of singly and doubly charged ions are compared in (g) and (h) to the measured N_2^{2+} data (red diamonds). The black solid (dashed) lines in (g) and (h) are the calculation results obtained with (without) inclusion of the lower-lying states. The blue (gray) solid line and the red crosses in (h) denote, respectively, the calculated and measured asymmetry curves of the singly charged ions. Here, the undetermined CEP offset in the experimental data was chosen such that the asymmetries of the measured and the calculated Ar^+ spectra oscillate in phase.

of two additional fictitious states with excitation energies of 9.5 and 11.5 eV. The calculation results are summarized in Fig. 4. Due to the decreasing tunneling probability, the NSDI yields from states with energies below the first excited state of Ar rapidly decrease with decreasing excitation energy and thus constitute just a small correction. In particular, it can be seen in Figs. 4(a)–4(d) that these lower-lying states add a small contribution of low-energy anticorrelated electrons in the correlation spectrum that leads to a slight merging of the islands in the CEP-resolved momentum spectrum of the doubly charged ions, as can be seen in Figs. 4(e) and 4(f). This feature, which is consistent with the experimental observations, flattens the dip in the corresponding CEP-averaged spectrum presented in Fig. 4(g). Finally, one can see from Fig. 4(h) that the agreement between the measured and calculated asymmetry curves is also improved. In spite of the good agreement, we would like to point out that the contribution of lower-lying excited states is considered only qualitatively in the present analysis. Rather than a quantitative description, our approach may provide a basis for a more detailed treatment taking into account exact electron-impact excitation cross sections for the relevant molecular states.

IV. CONCLUSIONS

We have performed a direct comparison of NSDI of Ar and N_2 triggered by a single recollision event. A remarkably high degree of similarity was observed in the CEP-resolved correlation spectra, which both exhibit totally asymmetric energy sharing between the electrons. We have shown that not only the striking similarities but also the differences in NSDI of the two studied species can be understood in terms of RESI with subcycle depletion of the excited-state population. The development of quantitative models for NSDI in molecules should benefit from both the many constraints imposed by our highly differential experimental data and the fact that a rigorous theoretical treatment of NSDI is significantly easier for an isolated recollision event than for the more complex long-pulse dynamics involving multiple recollisions.

ACKNOWLEDGMENTS

We appreciate fruitful discussions with Carla Figueira de Morisson Faria, Tahir Shaaran, Joachim Kübel, and Hartmut Schröder. We thank Ferenc Krausz for his support and for making specialized equipment available to us. B.B. acknowledges additional support from Laszlo Veisz. We are grateful for support from the Max Planck Society and the DFG via Grants No. Kl-1439/3 and No. Kl-1439/5 and the Cluster of Excellence: Munich Center for Advanced Photonics (MAP). JRML personnel acknowledge support from the Chemical Sciences, Geosciences, and Biosciences Division, Office of Basic Energy Sciences, Office of Science, US Department of Energy under Grant No. DE-FG02-86ER13491 and the National Science Foundation under Grant No. CHE-0822646. K.J.B. and R.R.J. acknowledge support from the US Department of Energy under Grant No. DE-FG02-00ER15053.

[1] C. Figueira de Morisson Faria and X. Liu, J. Mod. Opt. **58**, 1076 (2011).
[2] V. V. Suran and I. P. Zapesochnyi, Sov. Tech. Phys. Lett. **1**, 420 (1975).
[3] A. L'Huillier, L. A. Lompré, G. Mainfray, and C. Manus, Phys. Rev. Lett. **48**, 1814 (1982).
[4] B. Witzel, N. A. Papadogiannis, and D. Charalambidis, Phys. Rev. Lett. **85**, 2268 (2000).
[5] R. Moshammer *et al.*, Phys. Rev. Lett. **84**, 447 (2000).
[6] Th. Weber, H. Giessen, M. Weckenbrock, G. Urbasch, A. Staudte, L. Spielberger, O. Jagutzki, V. Mergel, M. Vollmer, and R. Dörner, Nature (London) **405**, 658 (2000).
[7] R. Moshammer *et al.*, Phys. Rev. Lett. **98**, 203001 (2007).
[8] A. Rudenko *et al.*, Phys. Rev. Lett. **101**, 073003 (2008).
[9] P. Tzallas, E. Skantzakis, L. A. A. Nikolopoulos, G. D. Tsakiris, and D. Charalambidis, Nat. Phys. **7**, 781 (2011).
[10] M. Hentschel, R. Kienberger, Ch. Spielmann, G. A. Reider, N. Milosevic, T. Brabec, P. Corkum, U. Heinzmann, M. Drescher, and F. Krausz, Nature (London) **414**, 509 (2001).
[11] A. Baltuška *et al.*, Nature (London) **421**, 611 (2003).
[12] F. Krausz and M. Ivanov, Rev. Mod. Phys. **81**, 163 (2009).
[13] X. Liu *et al.*, Phys. Rev. Lett. **93**, 263001 (2004).
[14] T. Wittmann, B. Horvath, W. Helml, M. G. Schätzel, X. Gu, A. L. Cavalieri, G. G. Paulus, and R. Kienberger, Nat. Phys. **5**, 357 (2009).
[15] T. Rathje, Nora G. Johnson, M. Möller, F. Süßmann, D. Adolph, M. Kübel, R. Kienberger, M. F. Kling, G. G. Paulus, and A. M. Sayler, J. Phys. B **45**, 074003 (2012).
[16] B. Bergues *et al.*, Nat. Commun. **3**, 813 (2012).
[17] N. Camus *et al.*, Phys. Rev. Lett. **108**, 073003 (2012).
[18] G. N. Gibson, R. R. Freeman, and T. J. McIlrath, Phys. Rev. Lett. **67**, 1230 (1991).
[19] F. Grasbon, G. G. Paulus, S. L. Chin, H. Walther, J. Muth-Böhm, A. Becker, and F. H. M. Faisal, Phys. Rev. A **63**, 041402 (2001).
[20] A. Talebpour, C.-Y. Chien, and S. L. Chin, J. Phys. B **29**, L677 (1996).
[21] C. Guo, M. Li, J. P. Nibarger, and G. N. Gibson, Phys. Rev. A **58**, R4271 (1998).
[22] C. J. G. J. Uiterwaal, C. R. Gebhardt, H. Schröder, and K.-L. Kompa, Eur. Phys. J. D **30**, 379 (2004).
[23] R. Dörner, Th. Weber, M. Weckenbrock, A. Staudte, M. Hattass, H. Schmidt-Böcking, R. Moshammer, and J. Ullrich, Adv. At. Mol. Opt. Phys. **48**, 1 (2002).
[24] E. Eremina *et al.*, J. Phys. B **36**, 3269 (2003).
[25] E. Eremina, X. Liu, H. Rottke, W. Sandner, M. G. Schätzel, A. Dreischuh, G. G. Paulus, H. Walther, R. Moshammer, and J. Ullrich, Phys. Rev. Lett. **92**, 173001 (2004).
[26] D. Zeidler, A. Staudte, A. B. Bardon, D. M. Villeneuve, R. Dörner, and P. B. Corkum, Phys. Rev. Lett. **95**, 203003 (2005).
[27] J. R. Stallcop, J. Chem. Phys. **54**, 2602 (1971).

[28] D. C. Cartwright and T. H. Dunning, Jr., J. Phys. B. **8**, L100 (1975).
[29] T. Shaaran, B. B. Augstein, and C. Figueira de Morisson Faria, Phys. Rev. A **84**, 013429 (2011).
[30] T. Shaaran and C. Figueira de Morisson Faria (private communication).
[31] Y. Zhou and P. Lu, Front. Optoelectron. China **3**, 184 (2010).
[32] C. Figueira de Morisson Faria, T. Shaaran, and M. T. Nygren, Phys. Rev. A **86**, 053405 (2012).
[33] C. Huang, Y. Zhou, Q. Zhang, and P. Lu, Opt. Express **21**, 11382 (2013).
[34] W. Becker, Rev. Mod. Phys. **84**, 1011 (2012).
[35] N. G. Johnson *et al*., Phys. Rev. A **83**, 013412 (2011).
[36] M. Schultze *et al*., J. Electron Spectrosc. **184**, 68 (2011).
[37] J. Ullrich, R. Moshammer, A. Dorn, R. Dörner, L. Ph. H. Schmidt, and H. Schmidt-Böcking, Rep. Prog. Phys. **66**, 1463 (2003).
[38] M. Kübel, K. J. Betsch, Nora G. Johnson, U. Kleineberg, R. Moshammer, J. Ullrich, G. G. Paulus, M. F. Kling, and B. Bergues, New J. Phys. **14**, 093027 (2012).
[39] R. Kopold, W. Becker, H. Rottke, and W. Sandner, Phys. Rev. Lett. **85**, 3781 (2000).
[40] B. Feuerstein *et al*., Phys. Rev. Lett. **87**, 043003 (2001).

7.4. Publication IV

M. Kübel, K. J. Betsch, N. G. Kling, A. S. Alnaser, J.Schmidt, U. Kleineberg, Y.Deng, I. Ben-Itzhak, G. G. Paulus, T. Pfeifer, J. Ullrich, R. Moshammer, M. F. Kling, and B. Bergues, Nonsequential double ionization of Ar: from the single- to the many-cycle regime. *New J. Phys.* **16**, 033008 (2014).

This experiment was motivated by the observation that the NSDI dynamics in the single-cycle regime differ strongly from those induced by multi-cycle pulses. By recording correlation spectra for pulse durations in the range from 4 to 30 fs we showed that the transition in the NSDI dynamics occurs rather abruptly in the few-cycle regime. I performed the experiments and data analysis, as well as a large part of the data interpretation and writing of the manuscript. This project is our first one that was entirely carried out in the LMU laboratory, where I invested a tremendous amount of work on improving the laser to produce near-single-cycle pulses.

New Journal of Physics
The open access journal at the forefront of physics
Deutsche Physikalische Gesellschaft DPG | IOP Institute of Physics

Non-sequential double ionization of Ar: from the single- to the many-cycle regime

M Kübel[1,2], K J Betsch[1,3], Nora G Kling[1,3], A S Alnaser[1,4,5], J Schmidt[2], U Kleineberg[2], Y Deng[6], I Ben-Itzhak[3], G G Paulus[7,8], T Pfeifer[9], J Ullrich[9,10], R Moshammer[9], M F Kling[1,2,3] and B Bergues[1]

[1] Max-Planck-Institut für Quantenoptik, D-85748 Garching, Germany
[2] Department für Physik, Ludwig-Maximilians-Universität, D-85748 Garching, Germany
[3] J R Macdonald Laboratory, Physics Department, Kansas State University, Manhattan, KS 66506, USA
[4] Physics Department, American University of Shariah, PO Box 26666, Shariah, UAE
[5] Physics and Astronomy Department, King-Saud University, Riyadh 11451, Saudi Arabia
[6] Fritz-Haber-Institut der Max-Planck-Gesellschaft, D-14195 Berlin, Germany
[7] Institut für Optik und Quantenelektronik, Friedrich-Schiller-Universität, D-07743 Jena, Germany
[8] Helmholtz Institut Jena, D-07743 Jena, Germany
[9] Max-Planck-Institut für Kernphysik, D-69117 Heidelberg, Germany
[10] Physikalisch-Technische Bundesanstalt, D-38116 Braunschweig, Germany
E-mail: boris.bergues@mpq.mpg.de

Received 21 October 2013, revised 19 December 2013
Accepted for publication 19 December 2013
Published 5 March 2014

New Journal of Physics **16** (2014) 033008

doi:10.1088/1367-2630/16/3/033008

Abstract

The transition from the near-single to the multi-cycle regime in non-sequential double ionization of argon is investigated experimentally. Argon atoms are exposed to intense laser pulses with a center wavelength around 790 nm and the momenta of electrons and ions generated in the double ionization process are measured in coincidence using a reaction microscope. The duration of the near transform-limited pulses is varied from 4 to 30 fs. We observe an abrupt collapse of the cross-shaped two-electron momentum distribution [17] in the few-cycle regime. The transition to longer pulses is further accompanied by a strong increase in the fraction of anti-correlated to correlated electrons.

Keywords: non-sequential double ionization, coincidence spectroscopy, strong field physics

Non-sequential double ionization (NSDI) is characterized by the correlated emission of two electrons from an atom or molecule in a strong laser field. This phenomenon, which cannot be explained within the framework of the single-active-electron approximation, was discovered more than 30 years ago [1, 2], when a knee-shaped enhancement was observed in the intensity dependent yield curve of doubly charged ions. Since then, NSDI has been the subject of numerous studies (for recent reviews see e.g. [3, 4]). In particular, it was suggested that NSDI is a manifestation of the rescattering process [5, 6]. The observation of the characteristic double hump structure in the recoil-ion momentum spectra of doubly and multiply charged ions provided clear evidence that the emission of the second electron is triggered by the laser-driven recollision of the first electron with its parent ion [7].

A deeper insight into the NSDI process was provided by kinematically complete experiments where the correlated two-electron momentum distributions (briefly, two-electron spectrum) were measured. In particular, such measurements permit one to distinguish between (positively) correlated [8] and anti-correlated [9] electron emission, as illustrated in figure 1.

Correlated electron emission, in which the two electrons are ejected in the same direction (i.e., equal sign momenta), is usually attributed to direct electron impact ionization [10]. Anti-correlated electron emission, where the two electrons are ejected in opposite directions (i.e., opposite sign momenta), is ascribed to recollisional excitation and subsequent ionization [9]. Further studies revealed that the fraction of anti-correlated electrons to the total yield increases with decreasing laser intensity [11] and can even dominate at low intensity [12]. Classical-ensemble calculations [13] suggest that multiple recollisions of the electron with the parent core play a major role in the production of anti-correlated electrons [12].

Owing to the great advances in ultra-fast laser technology [14, 15], two-electron spectra could recently be measured using few-cycle [16] and near-single-cycle [17] pulses with known carrier-envelope phase (CEP). This has allowed the study of NSDI of Ar and N_2 in the extreme limit of a single recollision event [17, 18]. When averaged over CEP, the two-electron spectra were found to exhibit a cross-like shape. This feature, which is distinctively different from all previous experimental results obtained with longer pulses could be well reproduced by a semi-classical model based on recollision excitation with sub-cycle depletion [17].

The goal of the present study is to investigate the transition from single- to multi-cycle NSDI by recording correlated two-electron momentum distributions for laser-pulse durations ranging from 4 to 30 fs. We demonstrate that for a fixed intensity, the characteristic cross-shaped structure observed for 4 fs near Fourier-transform-limited pulses [17] quickly changes when the pulse duration is increased. This is accompanied by a rise in the yield ratio of anti-correlated to correlated electrons and associated with significant changes in the single-ionization dynamics.

The experimental setup has been outlined previously [17, 19]. Briefly, linearly polarized laser pulses with a central wavelength of 790 nm are generated at a repetition rate of 10 kHz in a chirped-pulse amplification (CPA) Ti:Sapphire laser-system and focused into a hollow-core fiber for spectral broadening. The laser pulse duration is varied by clipping the edges of the spectrum in the prism compressor of the CPA-laser system and adjusting the gas pressure in the hollow-core fiber. After the fiber, the pulses are compressed to near-Fourier-limited pulses using

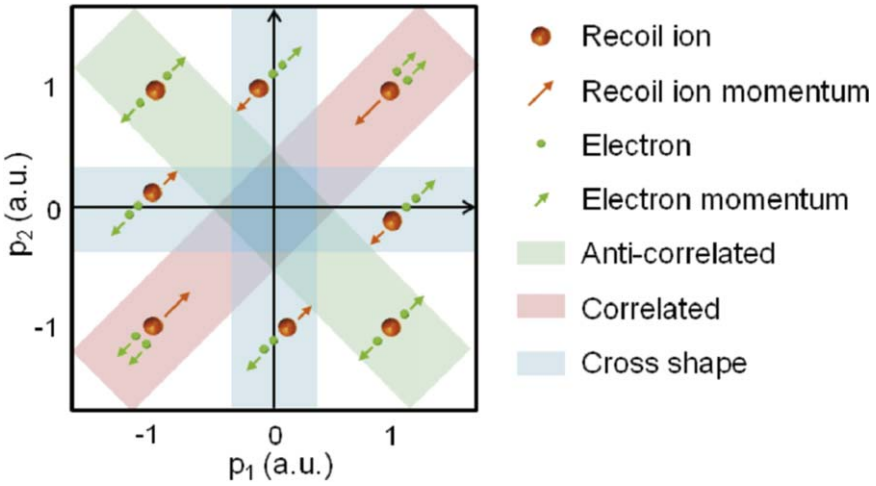

Figure 1. Illustration of the momentum sharing between the two electrons (green spheres) and the ion (orange sphere) after double ionization. Events in the red area in the first and third quadrants correspond to correlated electron emission (i.e. the momentum vectors of the two electrons point to the same direction). Events in the green area in the second and fourth quadrants correspond to anti-correlated electrons emission (i.e. the momentum vectors of the two electrons point to opposing directions). The blue cross-shaped area corresponds to events with totally asymmetric kinetic-energy sharing of the electrons along the laser polarization direction (i.e. one of the two electrons carries most of the kinetic energy).

chirped mirrors and fused silica wedges. The pulse duration is measured by fringe-resolved autocorrelation. The retrieved pulse durations are found to agree with those of the Fourier-limited pulses calculated from the measured laser spectra, suggesting a minimal chirp. We estimate the accuracy of the pulse-duration measurement to be on the order of 15%. The laser pulses are focused into a cold supersonic argon jet inside a reaction microscope (REMI) [20] in which the momenta of ions and electrons generated in the laser focus are measured in coincidence. The peak intensity is controlled using an iris aperture at the entrance of the REMI. Its value of about 1.0×10^{14} W cm^{-2} is estimated from the 10 U_p cut-off of the simultaneously measured single-ionization photoelectron spectra of Ar.

The two-electron spectra are generated by selecting all events in which at least one electron and one Ar^{2+} ion were detected. The second electron momentum is calculated as the negative momentum sum of the detected ion and the first electron. In order to reduce the effect of false coincidences, only events with a positive Ar^{2+} momentum (i.e. a momentum directed towards the ion detector) are considered. The total number of events in a two-electron spectrum is typically of the order of 10 000 and the estimated fraction of false coincidences to the total signal is smaller than 7%. The two-electron spectra are symmetrized with respect to the $p_2 = -p_1$ diagonal. Because the first and second electron are experimentally not distinguishable, the signal is also symmetrized with respect to the $p_2 = p_1$ diagonal.

In figure 2(a) we show the distributions of momenta $p_{\|}$ of Ar^+ and Ar^{2+} that were recorded for pulse durations of 4, 8, 16 and 30 fs ($p_{\|}$ denotes the momentum component parallel to the laser polarization direction). The widths of the Ar^+ spectra match fairly well, indicating that the peak intensity values for the different pulse durations were kept constant within an accuracy of

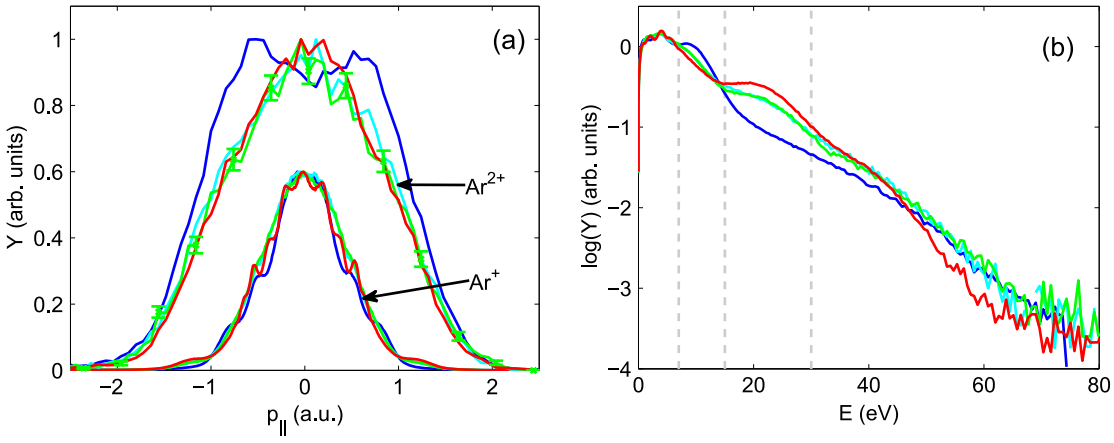

Figure 2. (a) Measured recoil-momentum distributions of Ar^+, and Ar^{2+} ions generated by 4 fs (blue), 8 fs (cyan), 16 fs (green), and 30 fs (red) pulses at a peak intensity of 1.0×10^{14} W cm^{-2}. For visual convenience the maxima of the momentum distributions of Ar^{2+} and Ar^+ are normalized to 1 and 0.6, respectively. Representative statistical error bars are shown for the Ar^{2+} signal generated with a 16 fs pulse. For the Ar^+ signal, the statistical error bars are on the order of the line thickness. (b) Single-ionization photoelectron energy spectra obtained via momentum conservation from the Ar^+ momentum distributions shown in (a). Each curve is normalized to its integral and the color coding is the same as in (a). The gray dashed lines mark the energy ranges $E = 7$–12 eV, and $E = 12$–30 eV, in which the pulse-duration dependence is most pronounced.

15%. Despite their similar widths, the Ar^+ spectra exhibit different features for different pulse durations. While the spectra are rather smooth for the intermediate pulse durations (8 and 16 fs), clear modulations originating from intra-cycle interferences [21–23] are visible for 4 fs and inter-cycle interferences resulting in the above threshold ionization (ATI) peaks can be seen at 30 fs. Due to the limited ion momentum resolution of about 0.1 au, the ATI peaks can only be resolved at low momenta where they are spaced sufficiently apart.

The single ionization photoelectron spectra shown in figure 2(b) exhibit a strong pulse-duration dependence in the energy range between 7 and 30 eV. In the region between 7 and 12 eV, the drop of the signal with increasing energy is considerably faster for longer pulses than for short ones. In the low-energy plateau region (from 15 to 30 eV), in contrast, the situation is reversed, giving rise to the ATI-enhancement reported in [24]. Quantum mechanical models [25], as well as semi-classical considerations [26] invoke multiple recollisions to explain this feature and its pulse duration dependence [28]. Its absence in the near single-cycle regime, for which multiple recollisions are fully suppressed, provides further evidence for the essential role of the latter in the build-up of the ATI enhancement.

As can be seen in figure 2(a), the shapes of the Ar^{2+} spectra generated with multi-cycle pulses (8, 16 and 30 fs) do not significantly differ from each other. They exhibit a maximum at zero momentum, in contrast to the Ar^{2+} spectrum generated with a 4 fs pulse, which exhibits a pronounced dip around $p_{\parallel} = 0$. This is consistent with previous observations by Rudenko *et al* [27] who reported the appearance of a similar dip when decreasing the pulse duration from 25 to 7 fs.

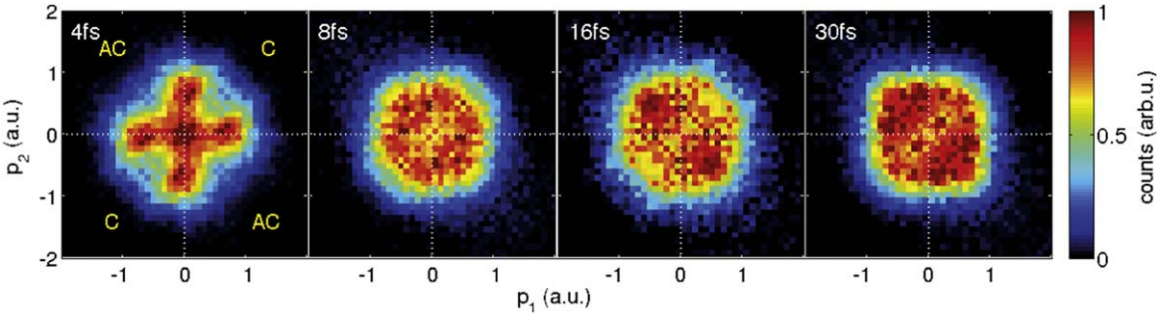

Figure 3. CEP-averaged two-electron spectra emerging from NSDI of Ar for different laser pulse durations at a peak intensity of 1.0×10^{14} W cm^{-2} as indicated in the figures. p_1 and p_2 denote the photoelectron momenta along the laser polarization. Invariance with respect to the $p_2 = p_1$ and $p_2 = -p_1$ diagonals were used to symmetrize the spectra. The labels C and AC in the first panel denote the quadrants with correlated and anti-correlated electron emission, respectively.

A more detailed understanding of the sudden change in the NSDI dynamics accompanying the transition into the few-cycle regime can be gained from the measured two-electron spectra. As shown in figure 3, the shapes of the two-electron spectra for 4 and 8 fs are qualitatively different. Starting from a cross shape for near-single-cycle pulses, the signal is more homogeneously distributed over the four quadrants of the two-electron spectrum for the longer pulse durations. At first sight, the 8 fs results are reminiscent of the uncorrelated momentum distribution that is expected for sequential double ionization [8]. Although the rate of sequential ionization increases with the pulse duration, such a rapid transition from NSDI to sequential ionization would be rather astonishing. As a matter of fact, a significant contribution of sequential double ionization can be ruled out for the following reasons: (i) the yield ratio of Ar^{2+} and Ar^{+} was less than 0.3% in all measurements presented in figure 3. Comparison of this ratio with the results of previous studies [29] indicates that the intensity used in our experiment was too low for the sequential ionization mechanism to dominate double ionization. (ii) As will be shown in figure 5, two-electron spectra recorded at higher intensity exhibit predominantly positively correlated electron momenta. This finding, which is consistent with the results of previous studies performed in the many-cycle regime (see for instance [8]), yields further evidence that the data shown in figure 3 were recorded at intensities well below the onset of sequential ionization. For a pulse duration of 8 fs, NSDI thus results in approximately equal contributions of positively correlated and anti-correlated electron emission.

With increasing pulse duration, however, significant deviations from an uncorrelated momentum distribution can be identified. Between 8 and 30 fs, the two-electron spectra exhibit a clear trend towards increasing anti-correlated electron emission. For two-electron spectra recorded at 16 and 30 fs the signal of anti-correlated electrons is stronger and extends to slightly higher momenta as compared to the result obtained with 8 fs pulses. The magnitude of the enhancement of anti-correlated electron emission with increasing pulse duration is quantified by plotting the ratio N_{AC}/N_C in figure 4. Here, N_C (N_{AC}) is the integrated signal in the first ($p_1, p_2 > 0$) and third ($-p_1, -p_2 > 0$) (second ($-p_1, p_2 > 0$) and fourth ($p_1, -p_2 > 0$)) quadrants. It can be seen that the relative contribution of anti-correlated electron emission tends to saturate for $\tau \gtrsim 8$ fs. This suggests that the observed transition in the NSDI dynamics originates from

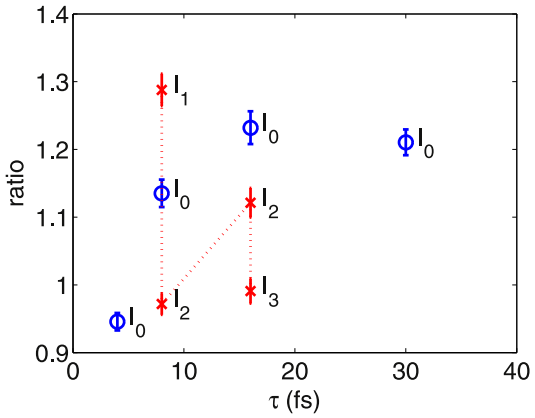

Figure 4. Dependence of the yield ratio of anti-correlated to correlated electrons N_{AC}/N_C on the pulse duration. The error bars include both statistical uncertainty and systematic errors due to false coincidences. Data points with blue circles and red crosses are obtained from the two-electron spectra of figures 3 and 5, respectively. The dotted red line serves as a guide to the order in which the data points are described in the text.

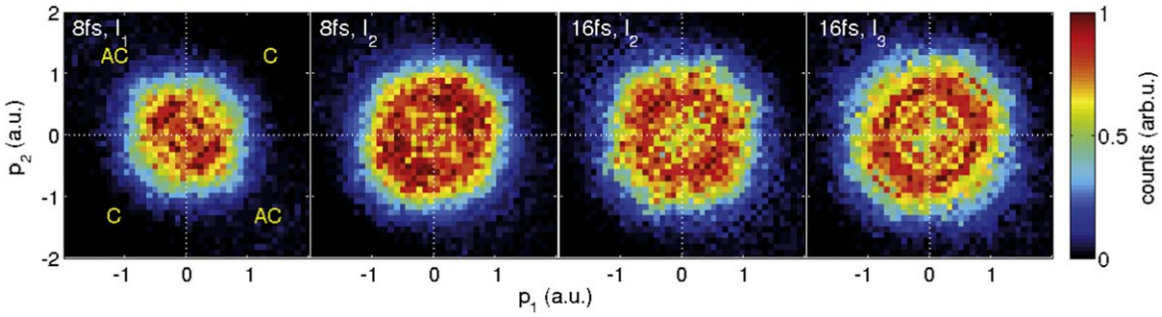

Figure 5. Two-electron spectra for NSDI of Ar recorded at different intensities $I_1 = 0.8 \times 10^{14}$ W cm^{-2}, $I_2 = 1.2 \times 10^{14}$ W cm^{-2}, $I_3 = 1.4 \times 10^{14}$ W cm^{-2} and pulse durations as indicated in the figure.

the contribution of only a small number of additional recollisions, confirming the exponential decay of the recollision probability described in [30].

In order to discuss the combined effect of intensity and pulse duration on NSDI, let us turn to the experimental results displayed in figure 5. The two-electron spectrum shown in the first panel was recorded at an intensity of $I_1 = 0.8 \times 10^{14}$ W cm^{-2} and for a pulse duration of 8 fs. For these laser parameters the emission of anti-correlated electrons is slightly favored. Increasing the intensity to $I_2 = 1.2 \times 10^{14}$ W cm^{-2}, while keeping the pulse duration fixed, results in the two-electron spectrum shown in the second panel, for which correlated electron emission is preferred. As shown in the third panel, this trend can be reversed simply by increasing the pulse duration to 16 fs while the intensity is kept constant. In the fourth panel the intensity is increased to $I_3 = 1.4 \times 10^{14}$ W cm^{-2} while the pulse duration is kept constant at 16 fs. Thereby some of the preferred emission of correlated electrons is recovered. The observed trends are quantified by plotting the yield ratio of correlated to anti-correlated electrons as red data points in figure 4. In summary, the above results support the following

conclusions: (i) increasing the pulse duration enhances anti-correlated electron emission and (ii) the observations that positively correlated electron emission increases with intensity [11, 12], is also valid in the few-cycle regime.

While the semi-classical model for recollision excitation with sub-cycle depletion [17, 18] performs well in the limiting case of single-cycle NSDI, an extension of this model to the case of multiple recollisions is demanding because of the large number of additional ad hoc assumptions required. Besides the more exact but also more challenging quantum mechanical computations [31–33], classical ensemble calculations [13, 34, 35] have proven to be a pragmatic and successful alternative route to describe NSDI. While they naturally account for multiple recollisions that lead to a repeated energy exchange between the electrons and the ionic core, these models could also explain the emission of anti-correlated electrons in longer pulses [36]. Very recently, Huang *et al* [37] were able to accurately describe our recent single-cycle NSDI experiment [17] using a classical ensemble model, suggesting that simulating the experimental results of the present study should be within reach.

In conclusion, we have investigated NSDI of Ar in the transition from the near-single-cycle to the many-cycle regime. We found that the main change in the dynamics occurs abruptly between 4 and 8 fs. In particular, the contribution of anti-correlated electron emission to NSDI strongly increases from 4 to 8 fs and tends to saturate soon beyond 8 fs, which suggests that only a few recollisions efficiently contribute to NSDI. Our results demonstrate that besides the peak intensity, the pulse duration provides a sensitive knob to control anti-correlated electron emission. More importantly, our data provide a solid basis for assessing the validity of different theoretical approaches and will hopefully contribute to the emergence of a coherent and quantitative theoretical description of NSDI from the single to the multi-cycle regime.

Acknowledgments

We appreciate fruitful discussions with Artem Rudenko. We thank Ferenc Krausz for his support and for making specialized equipment available to us. BB acknowledges additional support from Laszlo Veisz and ASA acknowledges support from the American University of Sharjah-UAE. We are grateful for support from the Max-Planck Society and the DFG via grants Kl-1439/3, Kl-1439/5 and the Cluster of Excellence: Munich Center for Advanced Photonics (MAP). JRML personnel acknowledges support from the Chemical Sciences, Geosciences, and Biosciences Division, Office of Basic Energy Sciences, Office of Science, US Department of Energy.

References

[1] Suran V V and Zapesochnyi I P 1975 *Sov. Tech. Phys. Lett.* **1** 420
[2] L'Huillier A, Lompré L A, Mainfray G and Manus C 1982 *Phys. Rev. Lett.* **48** 1814
[3] Figueira de Morisson F C and Liu X 2011 *J. Mod. Opt.* **58** 1076
[4] Becker W 2012 *Rev. Mod. Phys.* **84** 1011
[5] Krause J L, Schafer K J and Kulander K C 1992 *Phys. Rev. Lett.* **68** 3535
[6] Corkum P B 1993 *Phys. Rev. Lett.* **71** 1994
[7] Moshammer R *et al* 2000 *Phys. Rev. Lett.* **84** 447
[8] Weber Th *et al* 2000 *Nature* **405** 658

[9] Feuerstein B *et al* 2001 *Phys. Rev. Lett.* **87** 043003
[10] Kopold R, Becker W, Rottke H and Sandner W 2000 *Phys. Rev. Lett.* **85** 3781
[11] de Jesus V L B *et al* 2004 *J. Phys. B: At. Mol. Opt. Phys.* **37** L161
[12] Liu X *et al* 2008 *Phys. Rev. Lett.* **93** 263001
[13] Ho P J *et al* 2005 *Phys. Rev. Lett.* **94** 093002
[14] Hentschel M *et al* 2001 *Nature* **414** 509
[15] Baltuška A *et al* 2003 *Nature* **421** 611
[16] Camus N *et al* 2012 *Phys. Rev. Lett.* **108** 073003
[17] Bergues B *et al* 2012 *Nat. Commun.* **3** 813
[18] Kübel M *et al* 2013 *Phys. Rev.* A **88** 023418
[19] Johnson N G *et al* 2011 *Phys. Rev.* A **83** 013412
[20] Ullrich J *et al* 2003 *Rep. Prog. Phys.* **66** 1463
[21] Bergues B *et al* 2007 *Phys. Rev.* A **75** 063415
[22] Arbó D G *et al* 2010 *Phys. Rev.* A **81** 021403
[23] Gopal R *et al* 2009 *Phys. Rev. Lett.* **103** 053001
[24] Hertlein M P 1997 *J. Phys.* B **30** L197
[25] Muller H G and Kooiman F C 1998 *Phys. Rev. Lett.* **81** 1207
[26] Paulus G G *et al* 2001 *Phys. Rev.* A **64** 021401R
[27] Rudenko A *et al* 2004 *Phys. Rev. Lett.* **93** 253001
[28] Grasbon F *et al* 2004 *Phys. Rev. Lett.* **91** 173003
[29] Guo C *et al* 1998 *Phys. Rev.* A **58** R4271
[30] Ho Phay and Eberly J 2005 *Phys. Rev. Lett.* **95** 193002
[31] Shaaran T, Nygren M T and Figueira de Morisson F C 2010 *Phys. Rev.* A **81** 063413
[32] Parker J S *et al* 2006 *Phys. Rev. Lett.* **96** 133001
[33] Ruiz C *et al* 2006 *Phys. Rev. Lett.* **96** 053001
[34] Mauger F *et al* 2012 *Phys. Rev. Lett.* **108** 063001
[35] Emmanouilidou A and Staudte A 2009 *Phys. Rev.* A **80** 053415
[36] Haan S L, Smith Z S, Shomsky K N and Plantinga P W 2008 *J. Phys. B: At. Mol. Opt. Phys.* **41** 211002
[37] Huang C *et al* 2013 *Opt. Express* **21** 11382

7.5. Publication V

M. Kübel, A. S. Alnaser, B. Bergues, T. Pischke, J. Schmidt, Y. Deng, C. Jedrzejewski, J. Ullrich, G. G. Paulus, A. M. Azzeer, U. Kleineberg, R. Moshammer, and M. F. Kling, Strong-field control of the dissociative ionization of N_2O with near single-cycle pulses *New J. Phys.*, accepted.

The idea to apply the phase-tagged REMI to investigate the control of molecular dissociation by near-single-cycle pulses existed from the beginning of the REMI project on. To disentangle the CEP-dependencies of the large number of different ionization and dissociation channels of a polyatomic molecule such as N_2O, the coincident detection capabilities of the REMI have proven very useful. I contributed to the experimental work, analyzed and interpreted the data and wrote a large share of the manuscript.

7.6. Publication VI

A.S. Alnaser, M. Kübel, R. Siemering, B. Bergues, Nora G. Kling, K. J. Betsch, Y. Deng, J. Schmidt, Z. A. Alahmed, A. M. Azzeer, J. Ullrich, I. Ben-Itzhak, R. Moshammer, U. Kleineberg, F. Krausz, R. de Vivie-Riedle, and M. F. Kling, Sub-femtosecond Steering of Hydrocarbon Deprotonation *Nature Commun.* **5**, 3800 (2014).

C_2H_2 is a prototype molecule for the study of photo-induced dynamics in hydrocarbons. These dynamics include deprotonation and hydrogen migration. While we have observed a clear influence of the CEP of the driving laser pulses on the proton emission direction, CEP-dependencies in the migration channel could not yet been proven. Our experimental findings on the deprotonation channel agree well with the predictions of a new model suggested by the Vivie-Riedle group. My contribution involves experimental work and data analysis. I also assisted the preparation of the manuscript.

nature COMMUNICATIONS

ARTICLE

Received 21 Dec 2013 | Accepted 3 Apr 2014 | Published 8 May 2014

DOI: 10.1038/ncomms4800

Subfemtosecond steering of hydrocarbon deprotonation through superposition of vibrational modes

A.S. Alnaser[1,2,3], M. Kübel[4], R. Siemering[5], B. Bergues[2], Nora G. Kling[6], K.J. Betsch[2], Y. Deng[2], J. Schmidt[4], Z.A. Alahmed[3], A.M. Azzeer[3], J. Ullrich[7,8], I. Ben-Itzhak[6], R. Moshammer[7], U. Kleineberg[4], F. Krausz[2,4], R. de Vivie-Riedle[5] & M.F. Kling[2,4,6]

Subfemtosecond control of the breaking and making of chemical bonds in polyatomic molecules is poised to open new pathways for the laser-driven synthesis of chemical products. The break-up of the C-H bond in hydrocarbons is an ubiquitous process during laser-induced dissociation. While the yield of the deprotonation of hydrocarbons has been successfully manipulated in recent studies, full control of the reaction would also require a directional control (that is, which C-H bond is broken). Here, we demonstrate steering of deprotonation from symmetric acetylene molecules on subfemtosecond timescales before the break-up of the molecular dication. On the basis of quantum mechanical calculations, the experimental results are interpreted in terms of a novel subfemtosecond control mechanism involving non-resonant excitation and superposition of vibrational degrees of freedom. This mechanism permits control over the directionality of chemical reactions via vibrational excitation on timescales defined by the subcycle evolution of the laser waveform.

[1] Physics Department, American University of Sharjah, POB26666 Sharjah, UAE. [2] Max-Planck-Institut für Quantenoptik, D-85748 Garching, Germany. [3] Department of Physics & Astronomy, King-Saud University, Riyadh 11451, Saudi Arabia. [4] Department für Physik, Ludwig-Maximilians-Universität München, D-85748 Garching, Germany. [5] Department für Chemie und Biochemie, Ludwig-Maximilians-Universität München, 81377 München, Germany. [6] J. R. Macdonald Laboratory, Physics Department, Kansas-State University, Manhattan, Kansas 66506, USA. [7] Max-Planck-Institut für Kernphysik, D-69117 Heidelberg, Germany. [8] Physikalisch-Technische Bundesanstalt, D-38116 Braunschweig, Germany. Correspondence and requests for materials should be addressed to A.S.A. (email: aalnaser@aus.edu) or to M.F.K. (email: matthias.kling@lmu.de).

The nuclear kinematics that are responsible for making and breaking chemical bonds occur on femtosecond timescales[1]. The steering of chemical reactions has been demonstrated for a variety of systems in the gas and condensed phase using modulated light fields[2–6], with the amplitude, phase and polarization used as a control parameter. Breaking of the hydrogen bonds is one of the most important dynamic reactions in the chemistry related to biology, combustion and catalysis, motivating considerable efforts to monitor and ultimately control the process. It has been studied in great detail, where efficient strong-field-induced proton ejection was reported[7–14]. Dynamic charge localization[11] and concerted fragmentation[12] scenarios were suggested to explain the origin of the high kinetic energies of the ejected protons. These studies corroborated the need for ultrashort light pulses, consisting of a few cycles, for steering the deprotonation process. As an additional challenge, the aforementioned control schemes do not provide means for a bond-specific manipulation of the deprotonation in symmetric hydrocarbons.

Few-cycle pulses with well-defined waveforms[15] offer a new quality of control on direct manipulation of the wavefunction of a molecular system[16]. Few-cycle waveforms with adjustable carrier-envelope-phase (CEP) have permitted control of charge localization in the ionization and dissociation of diatomic molecules on a subfemtosecond timescale[17–21]. The approach has also been successful in altering the yields of ionization and fragmentation in hydrocarbons[13]. Despite its relevance to stereochemistry, that is, the rearrangements of atoms in a molecule, full control of the deprotonation of hydrocarbons, including the directional steering of the emission of the protons, has, however, not been reported.

Here, we demonstrate the subfemtosecond control of the proton-ejection direction from acetylene molecules with the waveform of near-single-cycle laser pulses. On the basis of quantum dynamical calculations, we show that the demonstrated directional control does not originate from electronic motion effects considered so far[16]. Rather, the mechanism is based on the manipulation of the phases of individual components of the multi-mode vibrational wave packet by the laser field in the neutral molecule and cation. While control of vibrational superpositions and their phase after resonant excitation has been performed in the context of molecular vibrational qubits[22,23], the superposition between vibrational modes is formed through a non-resonant process in our study and is controlled on an attosecond timescale. The process described here constitutes a novel mechanism for steering the reactions of complex molecules.

Results

Laser-induced deprotonation of the acetylene dication. The electric field waveform of (transform-limited) few-cycle light pulses can be described as $E(t) = E_0(t)\cos(\omega t + \phi)$, where $E_0(t)$ is the amplitude envelope, ω the carrier angular frequency and ϕ is the CEP. The CEP offers a way to tailor the electric field waveform on subfemtosecond timescales and has proven to be a powerful parameter for steering electron motion[16].

In our present experimental studies on the CEP control of the deprotonation of acetylene, we employ CEP-tagged reaction microscopy (REMI)[24] (for details see the Methods section). The interaction of acetylene molecules with intense few-cycle pulses results in the dissociative ionization and isomerization of the molecule yielding a variety of reaction products[7]. One of the reactions that we concentrate on here is the deprotonation of acetylene after two consecutive ionization steps, see Fig. 1a, where a 1D cut of the potential energy surfaces (PES) is shown. After

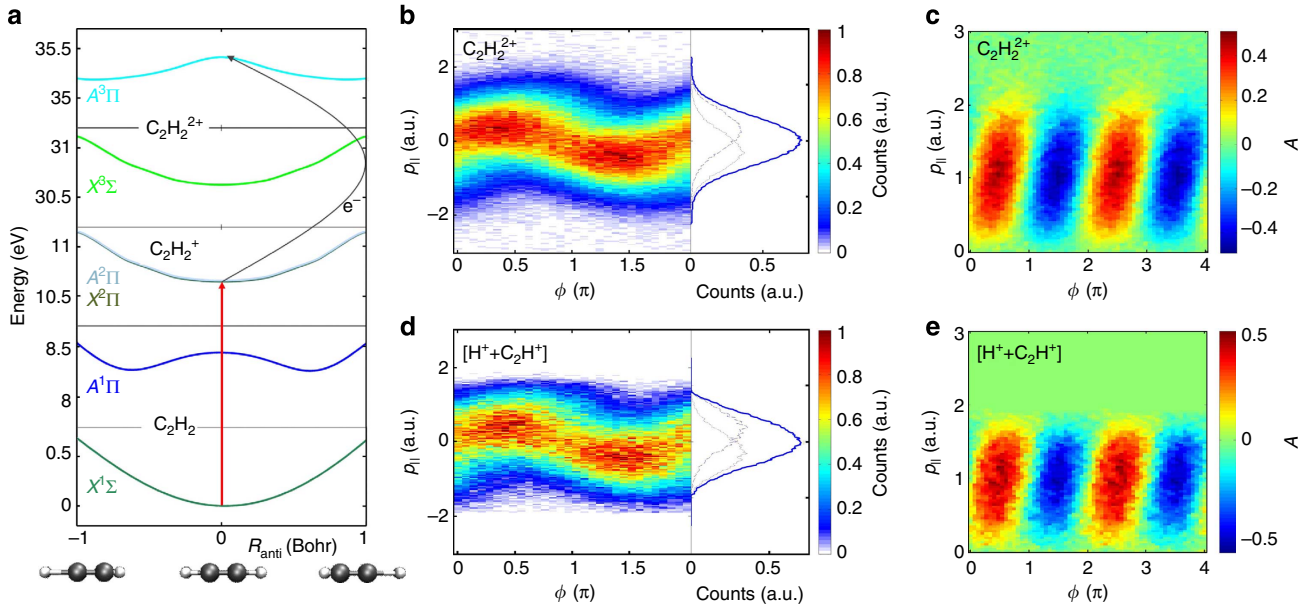

Figure 1 | Generation of the acetylene dication and the deprotonation fragments. (**a**) 1-D cut of potential energy curves of the considered states in the ionization and deprotonation: ground ($X^1\Sigma_g^+$) and first excited state ($A^1\Pi_u$) of the neutral molecule, the cation ground ($X^2\Pi_u$) and degenerate first excited state ($A^2\Pi_u$), and the dication ground ($X^3\Sigma_g^-$) and first excited state ($A^3\Pi_u$) along the anti-symmetric stretching coordinate R_{anti} at $R_{sym} = 0$. The red vertical line indicates the tunnelling ionization and the grey curved line marks the second ionization step by electron recollision. (**b**) Density plot of the acetylene dication longitudinal recoil momentum as a function of the experimental CEP, ϕ, for 4 fs pulses at an intensity of 2×10^{14} W cm^{-2}. CEP-integrated momenta are shown in the right panel. The dashed (dotted) lines shown correspond to CEP's with maximum positive (negative) asymmetry in the ion emission, respectively. (**c**) Density plot for the asymmetry parameter, $A(p_{||},\phi)$, for $C_2H_2{}^{2+}$ ions. (**d**) Density plot of the vector momentum sum of the recoil of the two (H^+,C_2H^+) deprotonation fragments. (**e**) Density plot of the asymmetry parameter for the momentum sum of the deprotonation fragments (H^+,C_2H^+).

population of the first excited state of $C_2H_2^{2+}$, the dication breaks up into H^+ and C_2H^+ fragments, which are detected with the REMI in coincidence.

To confirm the population scenario of the dication, which involves ionization by the laser field followed by subsequent recollisional ionization and excitation (Fig. 1a), high-resolution spectra of the longitudinal (along the laser polarization axis) momentum $p_{||}$ for the doubly charged $C_2H_2^{2+}$ recoil ions as a function of the CEP for 4-fs laser pulses at a peak intensity of 2×10^{14} W cm^{-2} were recorded and are shown in Fig. 1b. Clear modulation of the dication's momentum with the CEP is visible.

To enhance the visibility of CEP-effects, it is useful to define an asymmetry parameter, $A(p_{||},\phi)$, as

$$A(p_{\parallel},\phi) = \frac{N_{\mathrm{pos}}(p_{\parallel},\phi) - N_{\mathrm{neg}}(p_{\parallel},\phi)}{N_{\mathrm{pos}}(p_{\parallel},\phi) + N_{\mathrm{neg}}(p_{\parallel},\phi)} \quad (1)$$

with $N_{\mathrm{pos}}(p_{||}, \phi)$ and $N_{\mathrm{neg}}(p_{||}, \phi)$ representing the yields for positive and negative momentum components $p_{||}$, respectively. The 2-dimensional map in Fig. 1c for the dication shows high-amplitude asymmetry. Corroborated by previous studies on atoms[25] and diatomic molecules[26], the dependence of the recoil-ion momentum on the CEP indicates that the doubly charged ion, at this laser intensity, is formed via an electron recollision process. Here, the free electron created in the first tunnelling event is guided by the laser field, and, for certain CEPs, the electron will return with sufficient energy to ionize the $C_2H_2^+$ ion. Because of momentum conservation during ionization, the momentum sum of the two ionized electrons is equal and opposite to the measured recoil momentum of the $C_2H_2^{2+}$ ion (neglecting the small momentum contribution of the absorbed photons).

The data in Fig. 1b,c indicate that—for the near-single cycle pulses used in the experiment—the electron recollision and the corresponding double ionization and excitation of $C_2H_2^{2+}$ are controlled by the light waveform. This is analogous to previous findings on the non-sequential double ionization of argon with 4-fs pulses[25], where it was shown that electron recollision can be limited to a single event by using sufficiently short, CEP-controlled laser pulses.

Exploiting the applied coincident multi-particle detection scheme, the deprotonation channel has been identified by the coincidence of the H^+ and C_2H^+ fragments following the dissociation of the dication. We can investigate the dependence of their yield on the CEP. Figure 1d,e shows the CEP-dependent momentum sum, p_{sum}, of the coincident H^+ and C_2H^+ fragments parallel to the laser field and the asymmetry that is derived from these data.

A clear CEP dependence is visible in Fig. 1d,e exhibiting the same oscillatory behaviour as seen for the dication. The similarity of the two plots indicates that the recollision process is responsible for the recoil momentum of both the dication and the centre of mass motion of the reaction products after deprotonation.

Directional laser-waveform control of the deprotonation. As a signature of the deprotonation we investigate H^+ fragments from coincident creation of H^+ and C_2H^+ upon the break-up of the dication. Figure 2a,b shows the momentum and asymmetry for H^+ ions. The directional control of the deprotonation reaction becomes visible when analysing the asymmetry of the H^+ emission, which is shown in Fig. 2b. Figure 2c shows the asymmetry parameter $A(\phi)$ that has been integrated over all momenta of the H^+ fragments. The observed preferential CEP-dependent ejection of protons to the left and right of the laser polarization axis illustrates the subfemtosecond steering of the hydrogen ejection.

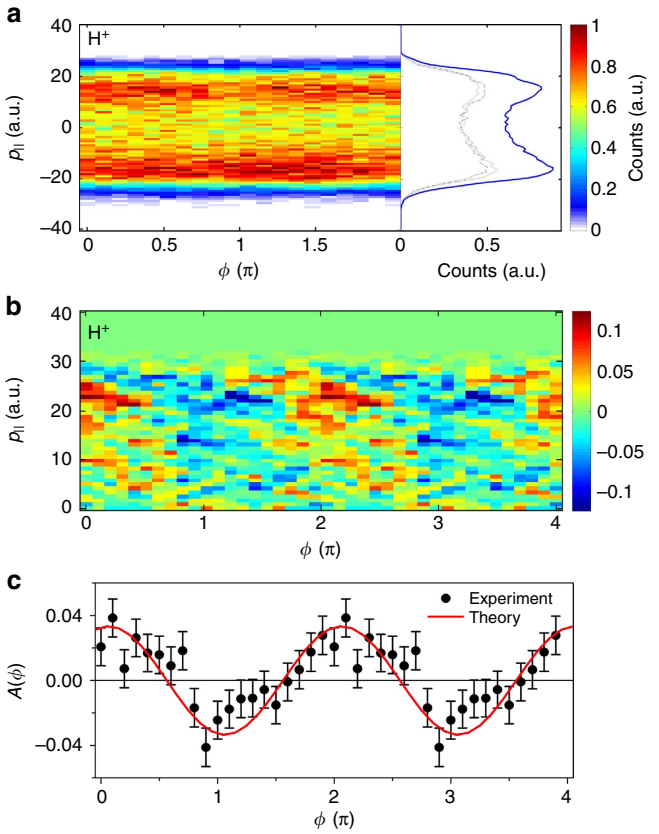

Figure 2 | Subfemtosecond directional control of deprotonation. (**a**) Density plot of the momentum of H^+ fragments as a function of CEP. CEP-integrated momenta are shown in the right panel. The dashed (dotted) lines shown correspond to CEP with maximum positive (negative) asymmetry in the ion emission, respectively. (**b**) Density plot for the asymmetry parameter, $A(p_{||},\phi)$, for the H^+ fragments. (**c**) The asymmetry parameter, $A(\phi)$, integrated over all momenta for H^+ ions. The error bars were derived via error propagation using the s.d. in the ion yields with positive and negative momenta. The clear oscillation in the asymmetry for the directional emission of H^+ fragments as a function of CEP under the given laser conditions demonstrates the CEP-control of the hydrogen emission direction. Also shown is the calculated asymmetry (solid red line) obtained from our quantum dynamical calculations (see text for details), which has been shifted in absolute CEP for best overlap with the experimental data since the absolute CEP is not known from the experiment.

Discussion

To account for the asymmetric deprotonation, the well-known Tannor-Rice control scheme exploiting excited state dynamics[27] might appear to be a first candidate. However, for the current case, where the involved electronic state potentials are symmetric with respect to the deprotonation direction, an additional asymmetry has to be introduced by the laser field. We have performed quantum dynamical calculations to model the relevant molecular dynamics. The details of our calculations are given in the Methods section. The deprotonation of the dication is described in the basis of the symmetric $|0m>$ and anti-symmetric C-H stretching $|n0>$ modes with m, n being the number of vibrational quanta, and $|0m>$ and $|n0>$ implicitly including the respective time evolution factor $e^{-i\frac{E_{m(n)}}{\hbar}t}$. Around the minimum of PES, these modes correspond to the normal modes and their respective overtones. A linear combination of these modes, $1/\sqrt{2}(|0m\rangle \pm |n0\rangle)$, will induce a wave packet

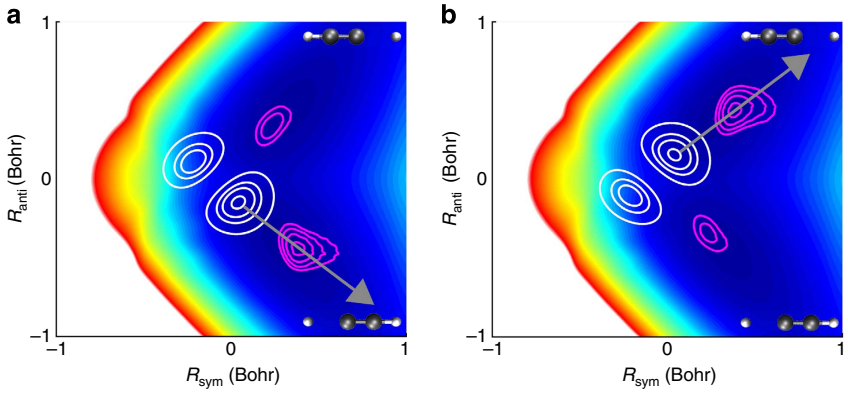

Figure 3 | The relevant first excited state of the dication for deprotonation. The state ($A^3\Pi_u$) is shown as a 2D-surface plotted against the symmetric and anti-symmetric stretching coordinates. The arrows in **a** and **b** indicate the two directions, into which protons can be emitted. To illustrate the control process, we plotted two wave packets representing the ideal superposition of $1/\sqrt{2}(|01\rangle - |10\rangle)$ (**a**) and $1/\sqrt{2}(|01\rangle + |10\rangle)$ (**b**). The initial wave packets are shown by white topographic lines, a snapshot of the same wave packet after 2.4 fs in magenta. The negative superposition (**a**) yields dominant cleavage of the left C-H bond, while the positive superposition (**b**) yields dominant cleavage of the right C-H bond.

motion along either one of the C-H stretching coordinates. When such a wave packet experiences a repulsive potential either the deprotonation of the left or the right H-atom is initiated. Two-dimensional (2D) PES along the normal mode coordinates (R_{sym}, R_{anti}) are calculated for the neutral, cationic, dicationic ground and excited states. The first excited state, the $A^3\Pi_u$ state, of the dication turns out to be the important state for the reaction (see Fig. 1a and Methods section) and its 2D surface is shown in Fig. 3.

From the stretching modes, only the anti-symmetric mode $|10>$ is IR-active, and the incident light field is not resonant with the vibrational transitions. To prepare the required superposition, it is sufficient to address and control only the anti-symmetric $|10>$ mode, via IR transitions. For the given light field, this happens in the neutral and cation. The symmetric mode contributions in the vibrational wave packet occur solely due to the ionization steps. The time-dependent population of the anti-symmetric mode $|10>$ follows the electric field evolution of the few-cycle pulse (see Methods section). The CEP of the pulse imprints a certain phase (φ_{CEP}) on the addressed anti-symmetric mode $|10>(|10>e^{-i\varphi_{CEP}t})$. When the few-cycle pulse is able to modify the phase of the anti-symmetric stretching mode, the sign in the superposition of the symmetric and anti-symmetric modes can be varied with the CEP and exhibits a modulation with a periodicity of 2π.

To mimic the effect of the second ionization including the recolliding electron, the cationic wave packet is projected onto the dication. During the second ionization step, the intensity of the remaining light field is too low to significantly enhance the control of the asymmetric stretching mode $|10>$ components. The main role of the recolliding electron is to provide the energy that is sufficient to reach the excited triplet state $A^3\Pi_u$. The energy of the recolliding electron can be evaluated for the given laser parameters to about 33 eV, corresponding to 3.17 U_p[28] with the ponderomotive potential $U_p = I/(4\omega^2)$ (in atomic units) that depends on the laser intensity I and the angular frequency ω. An electron energy of 25 eV is enough to reach the $A^3\Pi_u$ state of the dication. Because of the significant differences in the potential shape of the dicationic $A^3\Pi_u$ state and the cationic ground state (Fig. 1a), higher vibrational quanta ($|n0>$ and $|0m>$) up to the dissociation limit become now the dominant components of the vibrational wave packet and dissociation of the C-H bond can occur[13]. The preparation of the CEP-dependent features in the vibrational wave packet takes place in the neutral and cation, and is transferred to the dication in the second ionization. We observe that the propagation of the vibrational wave packet in the dication to either one of the dissociative channels ($H^+ + CCH^+$ and $HCC^+ + H^+$, see Fig. 3) can be manipulated by the CEP. Evaluation of the fraction of the wave packet correlating with the individual dissociation channels provides the theoretical asymmetry plotted in Fig. 2c. The theoretical curve shows excellent agreement with the experimental data, which lends support to the described novel subfemtosecond control mechanism.

The presented experimental and theoretical data support a new and very general coherent-control scheme, where the direction of proton ejection in a symmetric hydrocarbon is steered through manipulating the phases of the individual components of the vibrational wave packet. The CEP control-induced mechanism is substantially different from all previous studies, where electronic wave packets dominated the outcomes of the molecular dynamics[16], in the context of which the enhancement of the asymmetry through selection of vibrational states has been reported[29,30]. While in the current proof-of-principle experiment, the degree of control was rather limited, it can be enhanced by using near-single cycle waveforms that are resonant with the optically active mode. With the advent and current development towards the generation of ultrashort, phase-stable light pulses in the mid-infrared[31], substantial improvement of control is within reach. We expect the control scheme to be widely applicable to a variety of chemical processes, where the reactions of not only asymmetric but also symmetric molecules can be manipulated.

Methods

Experimental set-up. Linearly polarized laser pulses with a central wavelength of 750 nm, an energy of 150 μJ and a full width at half maximum of the temporal intensity envelope of 4 fs are generated at a repetition rate of 10 kHz in an amplified laser system. The laser intensity was kept stable on the level of 10%. The CEP of each laser pulse was recorded by sending a fraction of the laser beam (20 μJ) into a single-shot stereographic above-threshold ionization (Stereo-ATI) phase meter[32]. A detailed description of the CEP measurement and CEP tagging techniques can be found in ref. 33. In brief, the time-of-flight spectra of electrons emitted along both directions of the laser polarization axis are recorded on either side of the apparatus. For each laser shot, the CEP is inferred from the asymmetry between the left and the right TOF spectra. Note that the CEP is measured up to a constant offset in the phase meter.

In a recent study, we showed that slow drifts of the laser intensity can markedly affect the results of phase-tagged ionization yield measurements with long acquisition time[34]. To correct for any effects of small drifts of the laser parameters on the CEP measurement, we have applied the procedure outlined in ref. 34, which had been tested to give reliable phase-tagged ion yields for the non-sequential

double ionization of argon. The uncertainty in determining the CEP was on the order of 300 mrad during the entire measurement.

A fraction (up to 15 μJ) of the remaining part of the laser beam is focused with a spherical mirror ($f=25$ cm) into a well-localized (1 mm width) and cold supersonic gas jet of acetylene molecules in the centre of a REMI. Ions and electrons created in the laser focus (40 μm diameter) can be extracted by an electric field towards time- and position-sensitive MCP detectors at the left and right side of the instrument, respectively. In the current experiments, only ion signals were recorded. The ions' impact positions were determined utilizing a two-dimensional delay line anode mounted behind the MCP. Pulses from the ends of the x and y delay lines and a time signal from the microchannel plate were registered by a multi-hit time-to-digital converter and recorded in event mode. From these data, off-line analysis provided the 3D vector momentum of each ionic fragment at the instant of double ionization. The deprotonation fragments are identified and isolated from other fragments by applying tight momentum sum conditions using the coincidence high-resolution PIPICO (Photo-Ion Photo-Ion) spectra[7].

Statistical evaluation of the asymmetry data. To assess the statistical significance of the observed asymmetry, the data were subjected to a statistical test. Asymmetry curves were generated from the data for 1,000 different random re-orderings of the simultaneously recorded CEP values, that is, the CEP measured for an event was randomly associated with a different event before calculating the asymmetry. Any re-ordering should destroy the correlation of the data with the CEP, and those data can therefore be regarded as providing an upper limit for the noise of the measurement. The amplitude of the asymmetry oscillation was extracted from each test curve by a sinusoidal fit of the resulting asymmetry curve and plotted against the R^2 value in Fig. 4, which is defined as:

$$R^2 = 1 - \frac{\sum_i [A(\phi_i) - f(\phi_i)]^2}{\sum_i [A(\phi_i) - \bar{A}]^2} \quad (2)$$

where $\bar{A}$ denotes the mean value of the asymmetry over all bins and $f(\phi_i)$ the fitted asymmetry for bin i. The point corresponding to the true experimental data (non-randomized CEP ordering) is displayed as a blue point indicated by an arrow. It can be seen that this point shows a significantly larger goodness of the fit compared with the randomized test data. Therefore, despite its small amplitude, we conclude that the observed directional emission of protons is statistically significant.

Quantum chemistry methods. PES for ground and excited states of the neutral, cation and dication states of acetylene were calculated on the CASSCF[10,10], [9,10] and [8,10] level of theory, respectively, using the program package MOLPRO[35] with the 6-311++G** basis set as well as the dipole moments and transition dipole moments. Two-dimensional PES were calculated along the symmetric and anti-symmetric stretching coordinate with a step size of 0.05 a.u.. The PES were interpolated to 256 × 256 points for the evaluation of the vibrational eigenstates and the propagation of the vibrational wave packets. In the neutral molecule, only the IR-transitions play a role since the first excited state is separated by 7.8 eV (vertically) or 6.2 eV (adiabatically) and does not influence the ground state wave packet.

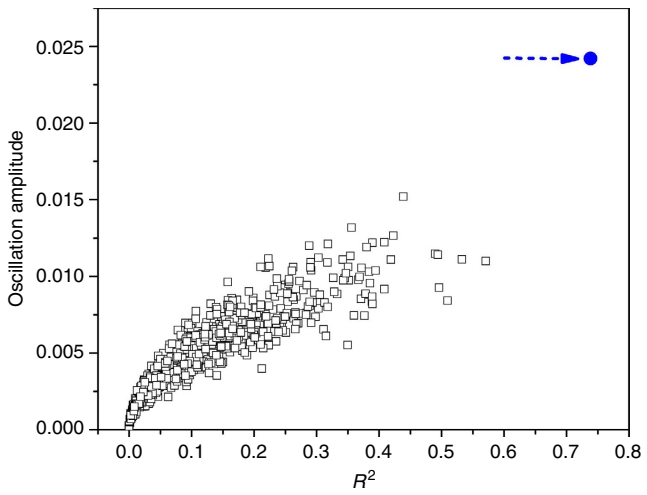

Figure 4 | Statistical evaluation of the asymmetry. In the measured data, the CEPs were randomized and the resulting asymmetry curve was fitted by a sinusoidal to extract the amplitude. This was repeated 1,000 times and the fitted amplitudes and R^2 values (see text) for each are plotted. The true experimental data are displayed as a blue point indicated by an arrow, demonstrating the statistical significance of the observed CEP-dependence.

Wave packet propagation. The Chebychev propagator was used to solve the time-dependent Schrödinger equation. The time-dependent Schrödinger equation for the neutral molecule under the influence of the light field reads:

$$(H_n + \mu_{nn}\varepsilon(t))\Psi_n(t) = \tilde{\Psi}_n(t) \quad (3)$$

with H_n the Hamiltonian of $X^1\Sigma_g^+$, μ_{nn} the associated dipole moment and $\varepsilon(t)$ the near-single cycle laser field.

The light field $\varepsilon(t)$ was included in the dipole approximation:

$$\varepsilon(t) = E_0 \exp\left[-2\left(\frac{t-t_1}{\mathrm{FWHM}/\sqrt{2\ln 2}}\right)^2\right]\cos(\omega_0(t-t_1)) \quad (4)$$

and was characterized by a full width at half maximum of 4 fs with a cycle-averaged intensity of 2×10^{14} W cm^{-2}. The light field was discretized with a time step of 0.024 fs. The part of the laser interaction experienced by the neutral molecule has a duration of 4.8 fs (200 time steps) in correspondence to the time when the intensity maximum is reached and the system is ionized. During that period, the initial superposition is formed. All ionization steps are approximated by setting the vibrational wave packet onto the corresponding ionic state.

In the first ionization step, the vibrational wave packet of the neutral molecule is transferred to the lowest cation states. The first two electronic states ($X^2\Pi_u$ and $A^2\Pi_u$) in the cation are nearly degenerate and we assume an equal distribution over both states in the ionization of the neutral molecule. A second type of interaction with the laser field via electronic transitions back and forth between the states is possible and included for completeness in the total Hamiltonian given below. However, the transition dipole moment between those states is almost non-existent along the deprotonation modes and its effect is negligible. The time-dependent Schrödinger equation for the cation reads:

$$\begin{pmatrix} H_1 + \mu_{11}\varepsilon(t) & -\mu_{12}\varepsilon(t) \\ -\mu_{21}\varepsilon(t) & H_2 + \mu_{22}\varepsilon(t) \end{pmatrix}\begin{pmatrix} \Psi_1(t) \\ \Psi_2(t) \end{pmatrix} = \begin{pmatrix} \tilde{\Psi}_1(t) \\ \tilde{\Psi}_2(t) \end{pmatrix} \quad (5)$$

with H_1, H_2 the Hamiltonians of $X^2\Pi_u$, $A^2\Pi_u$ of the cation, μ_{11}, μ_{22} the associated dipole moments, and μ_{12} the almost zero transition dipole moment.

The dissociation of the wave packet in the excited triplet state $A^3\Pi_u$ of the dication was propagated for 480 fs with time steps of 0.24 fs. The part of the wave packet leaving the PES (Fig. 3) on the top/bottom corresponds to the right/left deprotonation. Its amount is quantified by summing up all parts during the propagation

Mechanism of the CEP control. The neutral molecule experiences the part of the light field from time t_0 to t_1 (see Fig. 5a). The population of, for example, the

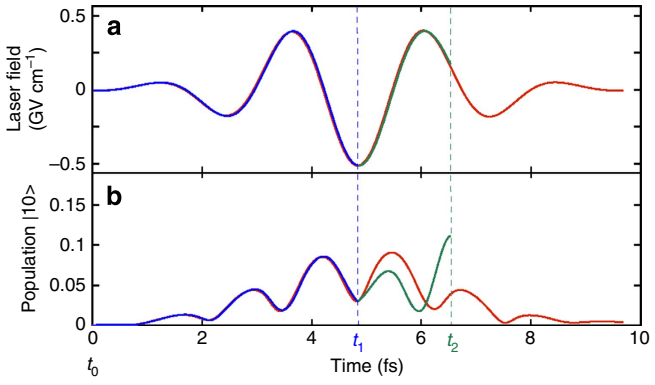

Figure 5 | Laser-field control of asymmetric hydrogen bond breaking. (**a**) Electric field waveform of the near-single-cycle laser pulse used in the calculations (red line). The parts of the field that act on the neutral and cation are displayed as blue and green lines, respectively. (**b**) Population of the IR-active mode |10>. The population induced in the neutral molecule is shown as blue line. At the peak of the laser field (t_1), the |10> population is transferred to the cation and its evolution is shown as the green line. Recollisional excitation, 1.7 fs (t_2) later, transfers the population to the $A^3\Pi_u$ state of the dication, from where dissociation can occur. Now the eigenfunctions constituting the vibrational wave packet are continuum wavefunctions. Without ionization, interaction with the entire field would induce only a transient population shown as red line, which vanishes with the end of the laser pulse.

anti-symmetric mode $|10>$ (Fig. 5b) follows the electric field of the few-cycle pulse. The CEP of the few-cycle pulse imprints a certain phase (φ_{CEP}) on the eigenfunction of $|10>(|10>e^{-i\varphi_{CEP}t})$, which leads through superposition with the $|01>$ mode (populated in the ionization) to the directional deprotonation. Ionization is assumed to happen at maximal field strength (see blue line at t_1 in Fig. 5b). From the evolution of the $|10>$ population, it becomes obvious that the ionization step is crucial to populate the $|10>$ mode as the interaction with the complete non-resonant light field would induce neither population (shown in red) nor phase information transfer. The first ionization transfers the vibrational wave packet to the cation. The major part of the wave packet is still the $|00>$ component with no directional preference. However, because of the slight difference in the shape of the neutral and cationic potential energy curves now also the IR inactive mode $|01>$ is slightly populated with a system dependent, but uncontrollable phase $e^{-i\frac{E_{01}}{\hbar}t}$. The population of the IR-active mode $|10>$ is further increased by the interactions with the remaining light field (Fig. 5b, green line) and the imprinted phase in the superposition, defining the direction of the wave packet oscillation, is strengthened. The cation experiences the part of the light field from time t_1 to t_2 (Fig. 5a). Contributions from higher vibrational quantum numbers may occur, but play a minor role. The prepared wave packet retains the memory of direction, when transferred to the dication in the final step.

References

1. Zewail, A. H. Laser femtochemistry. *Science* **242,** 1645–1653 (1988).
2. Brixner, T. & Gerber, G. Quantum control of gas-phase and liquid-phase femtochemistry. *ChemPhysChem.* **4,** 418–438 (2003).
3. Brif, C., Chakrabarti, R. & Rabitz, H. Control of quantum phenomena: past, present and future. *New J. Phys.* **12,** 075008 (2010).
4. Judson, R. S. & Rabitz, H. Teaching lasers to control molecules. *Phys. Rev. Lett.* **68,** 1500–1503 (1992).
5. Assion, A. *et al.* Control of chemical reactions by feedback-optimized phase-shaped femtosecond laser pulses. *Science* **282,** 919–922 (1998).
6. Daniel, C. *et al.* Deciphering the reaction dynamics underlying optimal control laser fields. *Science* **299,** 536–539 (2003).
7. Alnaser, A. S. *et al.* Momentum-imaging investigations of the dissociation of D_2^+ and the isomerization of acetylene to vinylidene by intense short laser pulses. *J. Phys. B* **39,** S485–S492 (2006).
8. Hoshina, K., Furukawa, Y., Okino, T. & Yamanouchi, K. Efficient ejection of H_3^+ from hydrocarbon molecules induced by ultrashort intense laser fields. *J. Chem. Phys.* **129,** 104302 (2008).
9. Itakura, R. *et al.* Two-body Coulomb explosion and hydrogen migration in methanol induced by intense 7 and 21fs laser pulses. *J. Chem. Phys.* **127,** 104306 (2007).
10. Xu, H., Okino, T., Nakai, K. & Yamanouchi, K. Ultrafast hydrogen migration in hydrocarbon molecules driven by intense laser fields. in *Progress in Ultrafast Intense Laser Science VII* 35–52 (Springer, 2011).
11. Markevitch, A. N., Romanov, D. A., Smith, S. M. & Levis, R. J. Coulomb explosion of large polyatomic molecules assisted by nonadiabatic charge localization. *Phys. Rev. Lett.* **92,** 063001 (2004).
12. Roither, S. *et al.* High energy proton ejection from hydrocarbon molecules driven by highly efficient field ionization. *Phys. Rev. Lett.* **106,** 163001 (2011).
13. Xie, X. *et al.* Attosecond-recollision-controlled selective fragmentation of polyatomic molecules. *Phys. Rev. Lett.* **109,** 243001 (2012).
14. Okino, T., Watanabe, A., Xu, H. & Yamanouchi, K. Ultrafast hydrogen scrambling in methylacetylene and methyl-d_3-acetylene ions induced by intense laser fields. *Phys. Chem. Chem. Phys.* **14,** 10640–10646 (2012).
15. Baltuška, A. *et al.* Attosecond control of electronic processes by intense light fields. *Nature* **421,** 611–615 (2003).
16. Kling, M. F., von den Hoff, P., Znakovskaya, I. & de Vivie-Riedle, R. (Sub-) femtosecond control of molecular reactions via tailoring the electric field of light. *Phys. Chem. Chem. Phys.* **15,** 9448–9467 (2013).
17. Kremer, M. *et al.* Electron localization in molecular fragmentation of H_2 by carrier-envelope phase stabilized laser pulses. *Phys. Rev. Lett.* **103,** 213003 (2009).
18. Betsch, K. J. *et al.* Controlled directional ion emission from several fragmentation channels of CO driven by a few-cycle laser field. *Phys. Rev. A* **86,** 063403 (2012).
19. Xu, H. *et al.* Carrier-envelope-phase-dependent dissociation of hydrogen. *New J. Phys.* **15,** 023034 (2013).
20. Sansone, G. *et al.* Electron localization following attosecond molecular photoionization. *Nature* **465,** 763–766 (2010).
21. Siu, W. *et al.* Attosecond control of dissociative ionization of O_2 molecules. *Phys. Rev. A* **84,** 063412 (2011).
22. Tesch, C. M. & de Vivie-Riedle, R. Quantum computation with vibrationally excited molecules. *Phys. Rev. Lett.* **89,** 157901 (2002).
23. de Vivie-Riedle, R. & Troppmann, U. Femtosecond lasers for quantum information technology. *Chem. Rev.* **107,** 5082–5100 (2007).
24. Johnson, N. G. *et al.* Single-shot carrier-envelope-phase-tagged ion-momentum imaging of nonsequential double ionization of argon in intense 4-fs laser fields. *Phys. Rev. A* **83,** 013412 (2011).
25. Bergues, B. *et al.* Attosecond tracing of correlated electron-emission in non-sequential double ionization. *Nat. Commun.* **3,** 813 (2012).
26. Kübel, M. *et al.* Non-sequential double ionization of N_2 in a near-single-cycle laser pulse. *Phys. Rev. A* **88,** 023418 (2013).
27. Tannor, D. J., Kosloff, R. & Rice, S. A. Coherent pulse sequence induced control of selectivity of reactions: exact quantum mechanical calculations. *J. Chem. Phys.* **85,** 5805 (1986).
28. Lein, M. Molecular imaging using recollision electrons. *J. Phys. B* **40,** R135–R173 (2007).
29. Anis, F. & Esry, B. D. Enhancing the intense field control of molecular fragmentation. *Phys. Rev. Lett.* **109,** 133001 (2012).
30. Lan, P., Takahashi, E. J., Liu, K., Fu, Y. & Midorikawa, K. Carrier envelope phase dependence of electron localization in the multicycle regime. *New J. Phys.* **15,** 063023 (2013).
31. Cerullo, G., Baltuška, A., Mücke, O. D. & Vozzi, C. Few-optical-cycle light pulses with passive carrier-envelope phase stabilization. *Laser & Photon. Rev.* **5,** 323–351 (2011).
32. Wittmann, T. *et al.* Single-shot carrier-envelope phase measurement of few-cycle laser pulses. *Nat. Phys.* **5,** 357–362 (2009).
33. Rathje, T. *et al.* Review of attosecond resolved measurement and control via carrier-envelope phase tagging with above-threshold ionization. *J. Phys. B* **45,** 074003 (2012).
34. Kübel, M. *et al.* Carrier-envelope-phase tagging in measurements with long acquisition times. *New J. Phys.* **14,** 093027 (2012).
35. Werner, H. J. *et al. Molpro, Version 2006.1, a Package of Ab-Initio Programs* (2006).

Acknowledgements

We are grateful for support by the DFG via the grant Kl-1439/3 and the Cluster of Excellence: Munich Center for Advanced Photonics (MAP). A.S.A. acknowledges support from the American University of Sharjah. N.G.K., I.B. and M.F.K. were partially supported by the Chemical Sciences, Geosciences, and Biosciences Division, Office of Basic Energy Sciences, Office of Science, U.S. Department of Energy under DE-FG02-86ER13491 and the NSF under CHE-0822646. We are also grateful for support from the King-Saud University in the framework of the MPQ-KSU-LMU collaboration and the visiting professorship program.

Author contributions

A.S.A. and M.F.K. conceived the experiment. A.S.A., M.K., N.G.K., K.J.B. and Y.D. carried out the measurements; the data analysis and interpretation were done by A.S.A., M.K., B.B, N.G.K., K.J.B., R.S., R.d.V.-R. and M.F.K.; R.S. and R.d.V.-R. performed the calculations; part of the REMI was provided by and used in cooperation with R.M. and J.U.; the 10-kHz laser system was provided by and used in cooperation with J.S. and U.K.; Z.A.A., A.M.A., I.B. and F.K. contributed to the discussion of the results; the manuscript was prepared by A.S.A., M.K., R.S., B.B., F.K., R.d.V.-R. and M.F.K, and was discussed among all authors.

Additional information

Competing financial interests: The authors declare no competing financial interests.

Reprints and permission information is available online at http://npg.nature.com/reprintsandpermissions/

How to cite this article: Alnaser, A. S. *et al.* Subfemtosecond steering of hydrocarbon deprotonation through superposition of vibrational modes. *Nat. Commun.* 5:3800 doi: 10.1038/ncomms4800 (2014).

7.7. Other publications

1. F. Süßmann, S. Zherebtsov, J. Plenge, N. Johnson, M. Kübel, A. M. Sayler, V. Mondes, C. Graf, E. Rühl, G. G. Paulus, D. Schmischke, P. Swrschek, and M. F. Kling, Single-shot velocity-map imaging of attosecond light-field control at kilohertz rate, *Rev. Sci. Instrum.* **82**, 093109 (2011)

2. N. Camus, B. Fischer, M. Kremer, V. Sharma, A. Rudenko, B. Bergues, M. Kübel, N. Johnson, M. F. Kling, T. Pfeifer, J. Ullrich, and R. Moshammer, Attosecond correlated dynamics of two electrons passing through a transition state, *Phys. Rev. Lett.* **108**, 073003 (2012)

3. T. Rathje, N. Johnson, M. Möller, F. Süßmann, D. Adolph, M. Kübel, R. Kienberger, M. F. Kling, G. G. Paulus, and A. M. Sayler, Review of attosecond resolved measurement and control via carrierenvelope phase tagging with above-threshold ionization, *J. Phys. B* **45**, 074003 (2012)

4. Ph. A. Korneev, S. V. Popruzhenko, S. P. Goreslavski, T.-M. Yan, D. Bauer, W. Becker, M. Kübel, M. F. Kling, C. Rödel, M. Wünsche, and G. G. Paulus, Interference carpets in above-threshold ionization: from the coulomb-free to the coulomb-dominated regime, *Phys. Rev. Lett.* **108**, 223601 (2012)

5. S. Zherebtsov, F. Süßmann, P. Peltz, J. Plenge, K.J. Betsch, I. Znakovskaya, A. Alnaser, N. Johnson, M. Kübel, A. Horn, V. Mondes, G. Graf, S. A. Trushin, A. M. Azzeer, M. J. J. Vrakking, G. G. Paulus, F. Krausz, E. Rühl, Th. Fennel, and M. F. Kling, Carrierenvelope phase-tagged imaging of the controlled electron acceleration from SiO2 nanospheres in intense few-cycle laser fields, *New J. Phys.* **14**, 075010 (2012)

6. M. Magrakvelidze, O. Herrwerth, Y. H. Jiang, A. Rudenko, M. Kurka, L. Foucar, K.-U. Kühnel, M. Kübel, N. Johnson, C.-D. Schröter, S. Düsterer, R. Treusch, M. Lezius, I. Ben-Itzhak, R. Moshammer, J. Ullrich, M. F. Kling, and U. Thumm, Tracing nuclear-wave-packet dynamics in singly and doubly charged states of N2 and O2 with XUV-pumpXUV-probe experiments, *Phys. Rev. A* **86**, 013415 (2012)

7. K.J. Betsch, N. Johnson, B. Bergues, M. Kübel, O. Herrwerth, A. Senftleben, I. Ben-Itzhak, G. G. Paulus, R. Moshammer, J. Ullrich, M. F. Kling, and R. R. Jones, Controlled directional ion emission from several fragmentation channels of CO driven by a few-cycle laser field, *Phys. Rev. A* **86**, 063403 (2012)

8. K. Schnorr, A. Senftleben, M. Kurka, A. Rudenko, L. Foucar, G. Schmid, A. Broska, T. Pfeifer, K. Meyer, D. Anielski, R. Boll, D. Rolles, M. Kübel, M. F. Kling, Y. H. Jiang, S. Mondall, T. Tachibana, K. Ueda, T. Marchenko, M. Simon, G. Brenner, R. Treusch, S. Scheit, V. Averbukh, J. Ullrich, C.-D. Schröter, and R. Moshammer, Time-resolved measurement of interatomic coulombic decay in Ne_2, *Phys. Rev. Lett.* **111**, 093402 (2013)

9. Nora G. Kling, K.J. Betsch, M. Zohrabi, S. Zeng, F. Anis, U. Ablikim, B. Jochim, Z. Wang, M. Kübel, M. F. Kling, K. D. Carnes, B. D. Esry, and I. Ben-Itzhak, Carrier-envelope phase control over pathway interference in strong-field dissociation of H_2^+, *Phys. Rev. Lett.* **111**, 163004 (2013)

10. T. Paasch-Colberg, A. Schiffrin, N. Karpowicz, S. Kruchinin, Ö. Saglam, S. Keiber, O. Razskazovskaya, S. Mühlbrandt, A. Alnaser, M. Kübel, V. Apalkov, D. Gerster, J. Reichert, T. Wittmann, J. Barth, M. I. Stockman, R. Ernstorfer, V. Yakovlev, R. Kienberger, and F. Krausz, Solid-state light-phase detector, *Nature Photon.* **8** (2014)

A. Comments on the scattering angle

In our semiclassical model for NSDI, the final momentum of the first electron is influenced by the scattering angle β, defined as the angle between the momentum vectors just before and just after recollision at time t_2. Scattering off at an angle β corresponds to a momentum change along the laser polarization axis of $\Delta p = p_r\,(1 - \cos(\beta))$, where p_r is the recollision momentum. This momentum change significantly influences the shape of the electron correlation spectrum, as exemplified in figure 7 of publication 7.1).

In our simulations we have used a fixed scattering angle, which is certainly a significant simplification of the recattering dynamics. In a real physical scenario, the scattering angle would be continuously distributed and certainly depend on the electron recollision energy E_r. A more realistic scattering, however, would require additional ad-hoc assumptions in our model where the electron-ion interaction in the continuum is not explicitly modeled. Compared to the alternative of assuming a scattering function $\beta(E_r)$, the use of a fixed scattering angle as a free parameter is a rather economical approach, regarding the number of free model parameters.

Such a scattering function $\beta(E_r)$ for *elastic scattering* is given by the well-known Rutherford formula

$$\beta = \sqrt{\frac{1 + \cos(E_{\mathrm{kin}} b)}{1 - \cos(E_{\mathrm{kin}} b)}}, \tag{A.1}$$

where E_{kin} is the electron kinetic energy and b is the impact parameter. Eventhough the Rutherford formula is probably not applicable to the *inelastic collisions* in NSDI, it has been tested as an alternative approach to model the scattering of the first electron. The energy E_{exc} required for exciting the parent ion was subtracted from the recollision energy, $E_{\mathrm{kin}} = E_r - E_{\mathrm{exc}}$, before calculation of the scattering angle. The impact parameter was calculated as $b = v_\perp(t_2 - t_1)$, where $v_\perp$ was retrieved from a Gaussian distribution of width $w_b = 0.05\,\mathrm{a.u.}$. Excitation of the parent ion was assumed to take place for electrons recolling with sufficient energy and an impact parameter $b \leq b_{\mathrm{max}}$.

While the calculated correlation spectrum presented in figure A.1 has the general shape of a cross, it also features a signal of strongly correlated electrons, as marked in figure A.1(b). Analyzing the corresponding electron trajectories reveals that this signal is produced by backscattering ($\beta > 90°$) of the first electron. Interestingly, the increased width due to this signal compares very well to the experimental results, without assuming the contribution of higher excited states (compare with section 4.4). A similar strongly-correlated signal can be identified in experimental correlation spectra, such as figure 4.8 (f).

Recently, Huang *et al.* [74] obtained very good agreement with our experimental data from publication 7.1 using a fully classical ensemble calculation. In particular, the authors retrieved the distribution of the scattering angle, similar to figure A.1 (a), in their *ab initio* calculations.

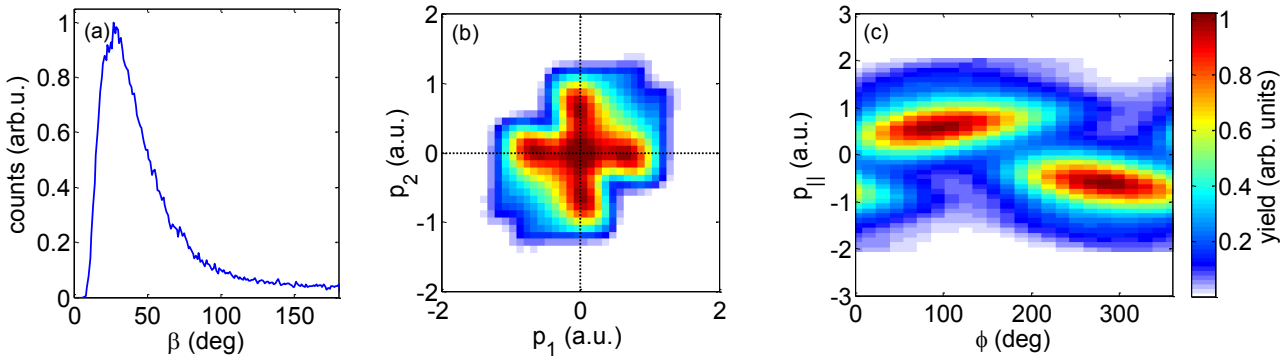

Figure A.1.: Results of an extendend version of the semi-classical NSDI model where the scattering angle for each trajectory was calculated according to Rutherford's scattering formula. See text for details. Shown are (a) the calculated probability density for the scattering angle β, (b) the electron correlation spectrum, and (c) the CEP-resolved ion momentum distribution.

They found a narrow distribution around $\beta = 20°$ for the parameters of our experiment, giving support to the assumptions made in our simulations.

B. Retrieval of the correlation spectra

The aim of the simulations of the retrieval of the correlation spectra is twofold: first, the impact of the data rate on the retrieved spectra can be analyzed and, second, it is possible to test the outcomes of different methods for generating the two-electron spectra from the measured data. In the first section, the simulation procedure is outlined. In the following two sections, it is shown how different methods lead to different artifacts in the correlation spectra, and the errors caused by false coincidences are quantified. False coincidences arise from the detection of background electrons, not originating from the ionization of a detected doubly-charged ion. The probability to detect a false coincidence depends on the count rate of background electrons, which mainly result from single ionization. The chapter closes with a discussion of the shape of the correlation spectrum induced by false coincidences.

B.1. Simulation of the measurement and retrieval of two-electron spectra

In the retrieval simulation, correlation spectra are generated from a list L of pairs of electron momenta $(p_{i,1}, p_{i,2})$, $(i = 1, 2, 3, ...)$. This list is required as input data. For the data processing, five more parameters are used: the detection efficiency $\epsilon \in (0, 1]$, the data rate r (being the number of background electrons per shot), the width of the momentum spectrum of the background electrons w, the detector deadtime t_d, and the spectrometer voltage V.

The simulation proceeds as follows. For every entry in L, the momentum of the doubly-charged ion is calculated as the negative momentum sum of the two electrons. In order to decide whether an electron is detected or not, a random number between 0 and 1 is generated for each electron and compared to ϵ. The electrons which are not detected are deleted. In addition to the detected electrons from L (zero, one or two), a random number of background electrons is generated according to a Poisson distribution with expectation value r. The momenta (in a.u.) of the background electrons are obtained from a Gaussian distribution with standard deviation w and mean value 0. For each detected electron (from L or background), the time-of-flight is calculated using the electron momentum and spectrometer voltage V. The TOF values are then tested for the dead time: after an electron has been detected, no electrons are considered during a time interval of t_d.

For each entry in L, the initially calculated ion momentum and the momenta of up to three detected electrons (including the background electrons) constitute a measured event. Using these events, correlation spectra are obtained using the methods described below.

B.2. Retrieval methods and simulation results

In figures B.1 and B.2, the correlation spectra retrieved by different methods from two different lists L are displayed. For figure B.1 electron momenta calculated with the semi-classical NSDI model are used, while for figure B.2 a hypothetical homogeneous square-shape distribution is assumed. In the following, all figure references relate to both, figures B.1 and B.2, if not otherwise specified. In each figure, the true correlation spectrum without background contributions is displayed in panel (a). The correlation spectra in panels (b-h) include background electrons and were obtained using the different methods described below.

In order to discuss the effect of the dead time on the retrieved correlation spectra we distinguish between two-particle coincidences, where a doubly-charged ion is detected together with one electron, and three-particle coincidences, where a doubly-charged ion is detected together with two electrons. The three-particle coincidences can be further divided into real coincidences, where the momenta of the three particles add up to zero, and false coincidences, where the momenta do not match.

Panel (b) displays the spectrum for two-particle coincidences only. In that case, the second electron momentum is calculated as $p_2 = -p_i - p_1$, where p_1 is the momentum of the detected electron and p_i is the measured ion momentum. The spectrum exhibits considerable artifacts. In particular, the signal around the $p_2 = p_1$ diagonal is excessive at the expense of the remainder of the spectrum. The cause of this artifact becomes clear when considering the spectrum retrieved from real three-particle coincidences (panel (c)), which contains no signal around the $p_2 = p_1$ diagonal. Clearly, the detector dead time is responsible for both artifacts. For two electrons impinging on the detector with a time-of-flight difference $\Delta t < t_d$, the detection of both electrons is prohibited by the dead time. Hence, panel (c) is not populated near the $p_2 = p_1$ diagonal while panel (b) exhibits excessive signal in the same region, because it represents an unrepresentative sample.

The spectrum in panel (d) corresponds to false three-particle coincidences. In these events at least one of the two electrons does not originate from the detected doubly-charged ion. For these events, one of the two electrons is selected and the second electron momentum is calculated as the negative momentum sum of the ion and the selected electron. Thus, the resulting spectrum contains at least 50% background contribution. It demonstrates in which way false coincidences may affect the experimental results. Clearly, false coincidences result in a broad triangular distribution in each of the halves of the correlation spectrum. The corners of these triangles reach far into the second and fourth quadrants and can be identified in the marked regions of the correlation spectra in figure B.1 as well as in experimental images (see for instance figure 4.8). The origin of the shape of the false coincidence correlation spectrum is further discussed in section B.4.

In order to suppress the impact of false coincidences, it may appear a solution to add the spectra from two- and real three-particle coincidences, i.e. the panels (b) and (c), and ignore the false three-particle coincidences of panel (d). This procedure results in the diagram shown in panel (e). Despite being largely clean of false coincidences, a gap around the $p_2 = p_1$ diagonal clearly remains in these spectra. While this is less obvious in figure B.1, it can be seen well in figure B.2. This indicates that ignoring false three-particle coincidences is an illegitimate selection of

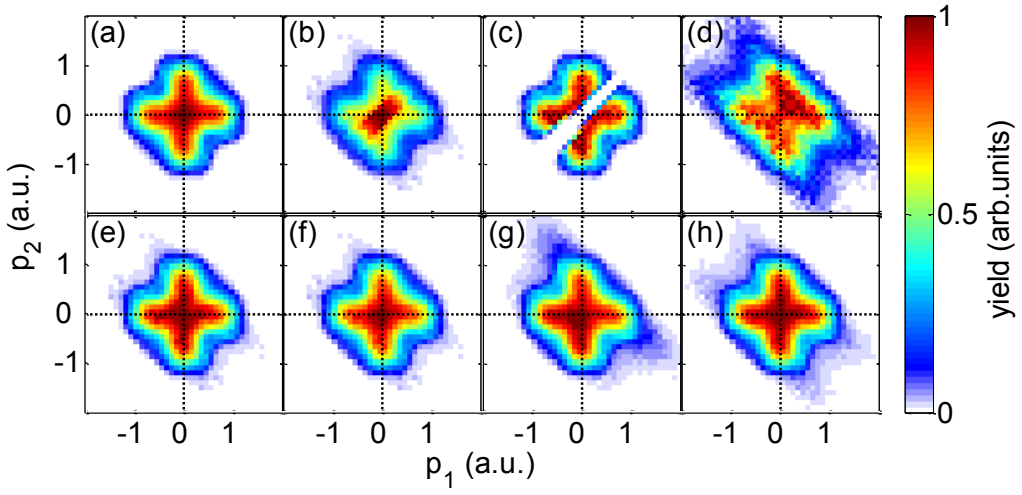

Figure B.1.: Simulation of the retrieval of a two-electron momentum distribution using a calculated dataset. Panel (a) displays the true correlation spectrum. The spectra in panels (b-h) were obtained using different analysis procedures outlined in the text. As can be seen, the different methods give rise to different artifacts and background contributions. The parameters (see text) used to generate this figure were $\epsilon = 0.5$, $t_d = 10\,\mathrm{ns}$, $r = 0.4$, and $V = 50\,\mathrm{V}$.

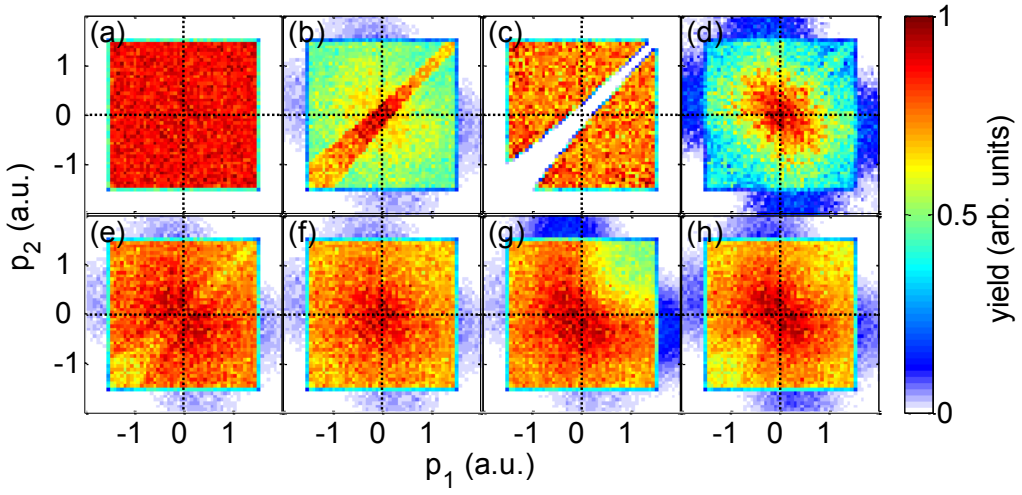

Figure B.2.: Same as figure B.1, but for a fictive distribution of electron momenta generating a homogeneous square pattern.

events.

The gap around the diagonal in panel (e) can be, in principle, compensated by weighting either one of the correlation spectra of panels (b) and (c) in such a way that in their sum the gap around the diagonal disappears and becomes smooth. This approach, that works well in theory, is demonstrated in panel (f). However, for experimental data, this approach could not be applied successfully due to the inhomogeneous distribution of false coincidences throughout the correlation spectrum.

Artifacts due to dead time can be avoided by using the following simple retrieval method. In any event where a doubly charged ion (momentum p_i) and at least one electron was detected, a second electron momentum is calculated as $p_2 = -p_i - p_1$, where p_1 is the momentum of the "first" electron. Note that, as opposed to the terminology used in previous chapters, here "first" electron denotes the electron with the shortest time of flight, in case more than one electron was detected. The correlation spectrum is filled using the momentum pairs (p_1, p_2), resulting in the spectrum shown in panel (g). This method is equivalent to using a detector that only allows one hit per laser shot. Note that this method is different from considering only events in which exactly one electron was detected (cf. panel (b)). Evidently, the results of panel (g) exhibit a pronounced inequality[1] of the bottom left half to the top right half of the correlation spectrum. The dependence of this inequality on the data rate is explained below. The bottom left half of the distribution is much cleaner than the top right-half, as can be seen by comparing it to the false-coincidence spectrum of panel (d).

The distribution of panel (h) is retrieved in a very similar way as (g). The methods differ for events where more than one electron is detected. Instead of choosing always the first electron, here, either the first or the second electron momentum is randomly chosen as p_1. Subsequently, p_2 is calculated and the correlation spectrum is generated as for panel (g). Because selecting a random electron spreads out the false coincidences over the bottom left and top right halves of the correlation spectrum, they are nearly equal in panel (h). However, the correlation spectrum lacks significant amount of signal in the bottom left and top right corner of the distribution. While this is not very obvious for the cross shape of figure B.1 it can be clearly seen for the square shape in figure B.2.

It is clear that the artifacts produced in either of the aforementioned analysis methods are a consequence of background electrons. Hence, the magnitude of the background electron count rate r is decisive for the accuracy of the retrieval of the correlation spectra. The dependence of this accuracy and the artificial inequality of the two halves of the correlation spectra on r is analyzed in the following section for the two methods of selecting the first or a random electron. Afterwards, a conclusion is drawn.

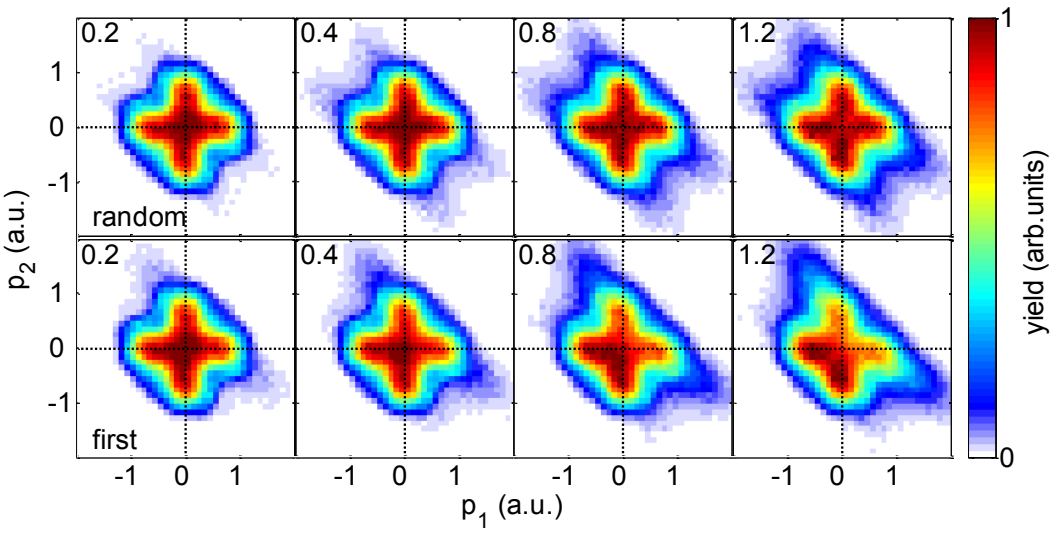

Figure B.3.: Simulation of the retrieved correlation spectra for different background electron rates as indicated in the figure panels. The results are shown for selecting either the first or a random electron, corresponding to the procedures shown in figures B.1(g) and (h).

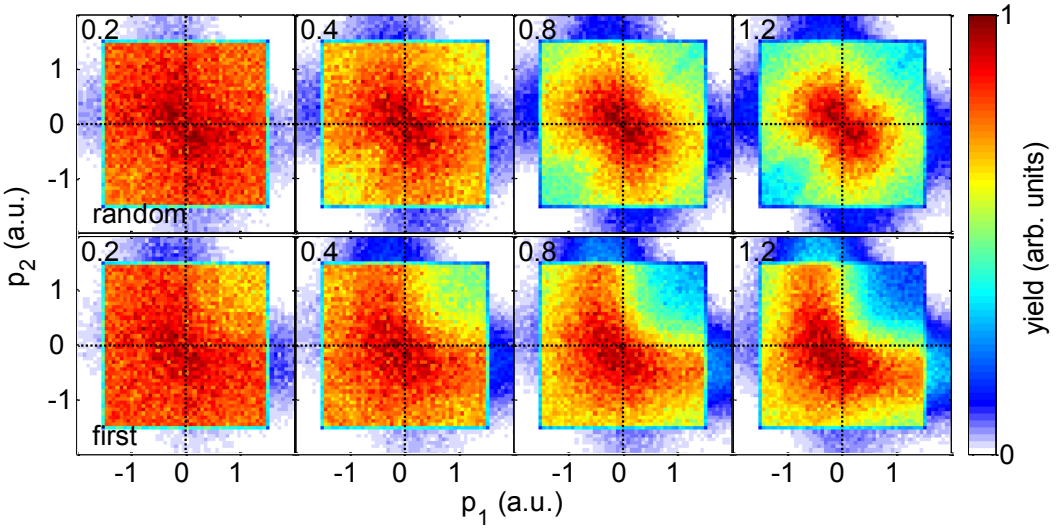

Figure B.4.: Same as figure B.3 but for a square shape distribution.

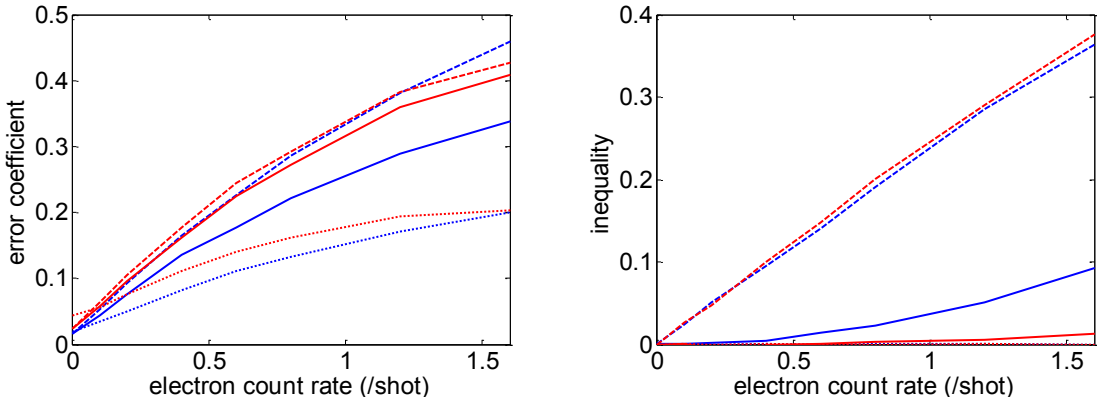

Figure B.5.: Simulation results for the accuracy of the retrieved spectra when either the first (dashed line) or a random electron (solid line) is selected. The dotted line corresponds to selecting the first electron and flipping the bottom left half (positive ion momenta) of the correlation spectrum to the top right half. The colors indicate two differently shaped distribution, a cross (blue, figure B.3) or a square (red, figure B.4). (a) Error coefficient as defined in the text, (b) left-right inequality induced by false coincidences. There is no inequality for the analysis of the left side only.

B.3. Impact of the count rate on the accuracy of the retrieval of the correlation spectra

In order to evaluate the dependence of the retrieved correlation spectra on the background electron count rate, the retrieval simulations were repeated for different numbers of background electrons per laser shot. The results are displayed in figures B.3 and B.4 for the cross and square shapes used above, and for selecting either the first electron or a random one (situations (g) and (h)).

As expected, the methods yield largely equivalent results for the low rate of 0.2 electrons per shot. At higher rates, however, the spectra retrieved by the two methods can be clearly distinguished. Most obviously, when the first electron is selected, the top right half of the spectrum develops severe errors. The situation is different in the bottom left half. Here, selecting the first electron yields rather reliable results even for rates around 1 electron per shot. When selecting a random electron, however, the error is spread out over both halves. Thus, it is advisable to consider only the bottom left half of the correlation spectrum retrieved by selecting the first electron and symmetrize the obtained spectrum with respect to the $p_2 = -p_1$ diagonal.

[1]To avoid confusion with CEP-dependent asymmetries, the evident asymmetry between the two halves of the correlation plot, induced by false coincidences, is denoted with the term inequality.

In order to quantify the above observations, a relative error coefficient is introduced as

$$\Delta(p_1, p_2) = \frac{M_r\,(p_1, p_2) - M_0\,(p_1, p_2)}{M_r\,(p_1, p_2) + M_0\,(p_1, p_2)}, \tag{B.1}$$

where M_r and M_0 are the retrieved and true correlation spectra normalized to their integrals, respectively. An absolute error coefficient R_Δ is then calculated by integrating $|\Delta(p_1, p_2)|$ over the full momentum ranges.

In figure B.5(a), this error coefficient is plotted as a function of the background electron count rate for both methods and shapes of figures B.3 and B.4. Integrated over the full spectrum, the method of selecting a random electron performs slightly better than when the first electron is selected. When the analysis is restricted to the bottom left half of the correlation plot and the spectra are symmetrized, however, selecting the first electron yields the best results, especially at higher count rates.

In figure B.5(b) the count rate dependence of the false-coincidence induced inequality between the left and right halves of the correlation plot, defined as

$$I = \frac{M_1 - M_3}{M_1 + M_3}, \tag{B.2}$$

where M_1 and M_3 are the integrals of the signals in the bottom left and top right quadrant, respectively. While the inequality for selecting a random electron is clearly dependent on the true distribution, it appears nearly independent for selecting the first electron. This behavior suggests that the inequality resulting from selecting always the first electron in the analysis can be used as an indicator of how much the data is affected by false coincidences.

In conclusion, the best results are achieved by the simple approach where only the first electron is considered, when the analysis is restricted to the bottom left half of the correlation spectrum. In this case, the upper right half of the correlation plot is obtained by exploiting the invariance of the CEP-dependent correlation spectra under the symmetry operation $(p, \phi) \to (-p, \phi + \pi)$.

B.4. The distribution induced by false coincidences

The shape of the two-electron distribution induced by false coincidences can be explained as follows. First, note that the projection of any point in the correlation plot onto the main diagonal essentially (up to a factor of 2) yields the negative value of the ion momentum. Therefore, when an ion with momentum p_i is detected, the position of that event in the correlation plot is fixed on a line parallel to the $p_2 = -p_1$ diagonal, which intersects the axes at $p_{1/2} = -p_i$. This p_i-diagonal is indicated in figure B.6 (a). For false coincidences, an electron is detected with a small momentum p_1, independent of the detected ion momentum. For simplicity, p_1 can be neglected, because the background electron momenta p_1 dominantly originate from the typically narrow momentum distribution of ATI electrons. The second electron momentum is then calculated as the negative momentum sum of p_i and p_1 and has a value $p_2 \approx -p_i$. Because the correlation spectra are always symmetric with respect to the main diagonal, false coincidences with an ion

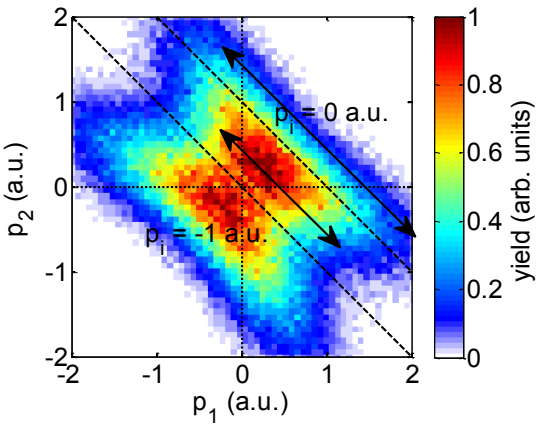

Figure B.6.: Schematic of a correlation spectrum induced by false coincidences. The p_i diagonals for ion momenta $p_i = 0$ a.u. and $p_i = -1$ a.u. are indicated. The arrows indicate the width of the distribution for the two values of p_i. For the simulation, an momentum distribution with a double peak was and a narrow Gaussian distribution were used for the ion and electron momentum, respectively.

of momentum p_i, thus, generate a signal on the corresponding p_i diagonal centered around $(p_i, 0)$ and $(0, p_i)$. This results in the observed triangular distribution of the false-coincidence signal. This has consequences for the measured correlation spectra if the contribution of false coincidences is significant. At large ion momenta, where false coincidences have a broad distribution, population is shifted parallel to the $p_2 = -p_1$ diagonal from the center to the outer regions of the correlation plot. In contrast, at low ion momenta, where the false-coincident distribution is narrow, false coincidences will enhance the signal in the center at expense of the outer regions.

Bibliography

[1] A. L'Huillier, L. Lompre, G. Mainfray, and C. Manus, Phys. Rev. Lett. **48**, 1814 (1982).

[2] R. Moshammer, B. Feuerstein, W. Schmitt, A. Dorn, C. Schroter, J. Ullrich, H. Rottke, C. Trump, M. Wittmann, G. Korn, K. Hoffmann, and W. Sandner, Phys. Rev. Lett. **84**, 447 (2000).

[3] T. Weber, M. Weckenbrock, A. Staudte, L. Spielberger, O. Jagutzki, V. Mergel, F. Afaneh, G. Urbasch, M. Vollmer, H. Giessen, and R. Dorner, Phys. Rev. Lett. **84**, 443 (2000).

[4] T. Weber, H. Giessen, M. Weckenbrock, G. Urbasch, A. Staudte, L. Spielberger, O. Jagutzki, V. Mergel, M. Vollmer, and R. Dorner, Nature **405**, 658 (2000).

[5] P. Corkum, Phys. Rev. Lett. **71**, 1994 (1993).

[6] E. Goulielmakis, M. Schultze, M. Hofstetter, V. S. Yakovlev, J. Gagnon, M. Uiberacker, A. L. Aquila, E. M. Gullikson, D. T. Attwood, R. Kienberger, F. Krausz, and U. Kleineberg, Science **320**, 1614 (2008).

[7] T. Wittmann, B. Horvath, W. Helml, M. G. Schätzel, X. Gu, A. L. Cavalieri, G. G. Paulus, and R. Kienberger, Nat. Phys. **5**, 357 (2009).

[8] A. M. Sayler, T. Rathje, W. Müller, K. Rühle, R. Kienberger, and G. G. Paulus, Opt. Lett. **36**, 16 (2011).

[9] J. Ullrich, R. Moshammer, A. Dorn, R. Dörner, L. P. H. Schmidt, and H. Schmidt-Böcking, Rep. Prog. Phys. **66**, 1463 (2003).

[10] A. Senftleben, A. Wirth, T. Rathje, I. Ben-Itzhak, M. Lezius, R. R. Jones, O. Herrwerth, B. Bergues, G. G. Paulus, W. Müller, C. D. Schröter, K. J. Betsch, K. Rühle, M. F. Kling, A. M. Sayler, J. Ullrich, N. G. Johnson, R. Moshammer, and S. De, Phys. Rev. A **83**, 013412 (2011).

[11] R. Kopold, W. Becker, H. Rottke, and W. Sandner, Phys. Rev. Lett. **85**, 3781 (2000).

[12] B. Feuerstein, R. Moshammer, D. Fischer, A. Dorn, C. Schröter, J. Deipenwisch, J. Crespo Lopez-Urrutia, C. Höhr, P. Neumayer, J. Ullrich, H. Rottke, C. Trump, M. Wittmann, G. Korn, and W. Sandner, Phys. Rev. Lett. **87**, 043003 (2001).

[13] Wikipedia, "Blitz," `http://de.wikipedia.org/wiki/Blitz`.

[14] P. Agostini, F. Fabre, G. Mainfray, G. Petite, and N. Rahman, Phys. Rev. **42**, 1127 (1979).

[15] F. Krausz and M. Ivanov, Rev. Mod. Phys. **81**, 163 (2009).

[16] A. Baltuška, T. Udem, and M. Uiberacker, Nature **421** (2003), 10.1038/nature01364.

[17] R. Kienberger, E. Goulielmakis, M. Uiberacker, A. Baltuska, V. Yakovlev, F. Bammer, A. Scrinzi, T. Westerwalbesloh, U. Kleineberg, U. Heinzmann, M. Drescher, and F. Krausz, Nature **427**, 817 (2004).

[18] T. H. Maiman, Nature **187**, 493 (1960).

[19] A. Franken, P. A. Franken, A. E. Hill, C. W. Peters, and G. Weinreich, Phys. Rev. Lett. **7**, 118 (1961).

[20] A. Wirth, M. T. Hassan, I. Grguras, J. Gagnon, A. Moulet, T. T. Luu, S. Pabst, R. Santra, Z. A. Alahmed, A. M. Azzeer, V. S. Yakovlev, V. Pervak, F. Krausz, and E. Goulielmakis, Science **334**, 195 (2011).

[21] G. G. Paulus, F. Lindner, H. Walther, A. Baltuska, E. Goulielmakis, M. Lezius, F. Krausz, and A. Baltuška, Phys. Rev. Lett. **91**, 253004 (2003).

[22] T. Paasch-Colberg, A. Schiffrin, N. Karpowicz, S. Kruchinin, O. Salam, S. Keiber, O. Razskazovskaya, S. Mühlbrandt, A. Alnaser, M. Kübel, V. Apalkov, D. Gerster, J. Reichert, T. Wittmann, J. V. Barth, M. I. Stockman, R. Ernstorfer, V. S. Yakovlev, R. Kienberger, and F. Krausz, Nat. Photon. **8**, 214 (2014).

[23] M. F. Kling, C. Siedschlag, A. J. Verhoef, J. I. Khan, M. Schultze, T. Uphues, Y. Ni, M. Uiberacker, M. Drescher, F. Krausz, and M. J. J. Vrakking, Science **312**, 246 (2006).

[24] A. Schiffrin, T. Paasch-Colberg, N. Karpowicz, V. Apalkov, D. Gerster, S. Mühlbrandt, M. Korbman, J. Reichert, M. Schultze, S. Holzner, J. V. Barth, R. Kienberger, R. Ernstorfer, V. S. Yakovlev, M. I. Stockman, and F. Krausz, Nature **493**, 70 (2013).

[25] L. V. Keldysh, Sov. Phys. JETP **20**, 1307 (1965).

[26] V. S. Popov, Phys. Usp. **47**, 855 (2004).

[27] M. V. Ammosov, N. B. Delone, and V. P. Krainov, Sov. Phys. JETP **64**, 1191 (1986).

[28] X. M. Tong and C. D. Lin, J. Phys. B **38**, 2593 (2005).

[29] D. B. Milošević, G. G. Paulus, D. Bauer, and W. Becker, J. Phys. B **39**, R203 (2006).

[30] J. Krause, K. Schafer, and K. Kulander, Phys. Rev. Lett. **68**, 3535 (1992).

[31] K. Schafer, B. Yang, L. DiMauro, and K. Kulander, Phys. Rev. Lett. **70**, 1599 (1993).

[32] G. G. Paulus, W. Nicklich, H. L. Xu, P. Lambropoulos, and H. Walther, Phys. Rev. Lett. **72**, 2851 (1994).

[33] A. Mcpherson, G. Gibson, H. Jara, U. Johann, T. S. Luk, I. A. Mcintyre, K. Boyer, and C. K. Rhodes, J. Opt. Soc. Am. **4**, 595 (1987).

[34] M. Ferray, A. Lhuillier, X. F. Li, L. A. Lompre, G. Mainfray, and C. Manus, J. Phys. B **21**, L31 (1988).

[35] G. G. Paulus, F. Lindner, D. B. Milosevic, W. Becker, and D. Milošević, Phys. Scripta **T110**, 120 (2004).

[36] W. Becker, F. Grasbon, R. Kopold, D. B. Milošević, G. G. Paulus, and H. Walther, Adv. At., Mol., Opt. Phys. **48**, 35 (2002).

[37] M. Lewenstein, P. Balcou, M. Ivanov, A. L'Huillier, and P. B. Corkum, Phys. Rev. A **49**, 2117 (1994).

[38] K. Henrichs, M. Waitz, F. Trinter, H. Kim, A. Menssen, H. Gassert, H. Sann, T. Jahnke, J. Wu, M. Pitzer, M. Kunitski, and R. Do, Phys. Rev. Lett. **113003**, 1 (2013).

[39] X. Hao, J. Chen, W. Li, B. Wang, X. Wang, and W. Becker, Phys. Rev. Lett. **112**, 073002 (2014).

[40] C. F. de Morisson Faria and X. Liu, J. Mod. Opt. **58**, 1076 (2011).

[41] W. Becker, X. Liu, P. J. Ho, and J. H. Eberly, Rev. Mod. Phys. **84**, 1011 (2012).

[42] B. Walker, B. Sheehy, and L. DiMauro, Phys. Rev. Lett. **73**, 0 (1994).

[43] R. Dörner, V. Mergel, O. Jagutzki, L. Spielberger, J. Ullrich, R. Moshammer, and H. Schmidt-Böcking, Phys. Rep. **330**, 95 (2000).

[44] Y. Liu, S. Tschuch, A. Rudenko, M. Dürr, M. Siegel, U. Morgner, R. Moshammer, and J. Ullrich, Phys. Rev. Lett. **101**, 053001 (2008).

[45] P. Ho, R. Panfili, S. Haan, and J. Eberly, Phys. Rev. Lett. **94**, 093002 (2005).

[46] X. Liu, H. Rottke, E. Eremina, W. Sandner, E. Goulielmakis, K. Keeffe, M. Lezius, F. Krausz, F. Lindner, M. Schätzel, G. Paulus, and H. Walther, Phys. Rev. Lett. **93**, 263001 (2004).

[47] A. Staudte, C. Ruiz, M. Schöffler, S. Schössler, D. Zeidler, T. Weber, M. Meckel, D. Villeneuve, P. Corkum, A. Becker, and R. Dörner, Phys. Rev. Lett. **99**, 263002 (2007).

[48] T. Shaaran, M. T. Nygren, and C. Figueira de Morisson Faria, Phys. Rev. A **81**, 063413 (2010).

[49] V. L. B. D. Jesus, B. Feuerstein, K. Zrost, D. Fischer, A. Rudenko, F. Afaneh, C. D. Schröter, R. Moshammer, and J. Ullrich, J. Phys. B **37**, L161 (2004).

[50] A. Rudenko, K. Zrost, B. Feuerstein, V. de Jesus, C. Schröter, R. Moshammer, and J. Ullrich, Phys. Rev. Lett. **93**, 253001 (2004).

[51] O. Herrwerth, A. Rudenko, M. Kremer, V. L. B. de Jesus, B. Fischer, G. Gademann, K. Simeonidis, A. Achtelik, T. Ergler, B. Feuerstein, C. D. Schröter, R. Moshammer, and J. Ullrich, New J.Phys. **10**, 025007 (2008).

[52] E. Eremina, X. Liu, H. Rottke, W. Sandner, M. Schätzel, A. Dreischuh, G. Paulus, H. Walther, R. Moshammer, and J. Ullrich, Phys. Rev. Lett. **92**, 173001 (2004).

[53] N. Camus, B. Fischer, M. Kremer, V. Sharma, A. Rudenko, B. Bergues, M. Kübel, N. G. Johnson, M. F. Kling, T. Pfeifer, J. Ullrich, and R. Moshammer, Phys. Rev. Lett. **108**, 073003 (2012).

[54] Y. Liu, L. Fu, D. Ye, J. Liu, M. Li, C. Wu, Q. Gong, R. Moshammer, and J. Ullrich, Phys. Rev. Lett. **112**, 013003 (2014).

[55] N. Camus, *Nonsequential double ionization of atoms with phase-controlled ultra-short laser pulses*, Ph.D. thesis, Ruperto-Carola Universität Heidelberg (2013).

[56] M. Weckenbrock, D. Zeidler, A. Staudte, T. Weber, M. Schöffler, M. Meckel, S. Kammer, M. Smolarski, O. Jagutzki, V. Bhardwaj, D. Rayner, D. Villeneuve, P. Corkum, and R. Dörner, Phys. Rev. Lett. **92**, 213002 (2004).

[57] V. Pervak, I. Ahmad, M. K. Trubetskov, A. V. Tikhonravov, and F. Krausz, Opt. Express **17**, 7943 (2009).

[58] M. Schultze, A. Wirth, I. Grguras, M. Uiberacker, T. Uphues, A. Verhoef, J. Gagnon, M. Hofstetter, U. Kleineberg, E. Goulielmakis, and F. Krausz, J. Electron. Spectrosc. Relat. Phenom. **184**, 68 (2011).

[59] B. Bergues, M. Kübel, N. G. Johnson, B. Fischer, N. Camus, K. J. Betsch, O. Herrwerth, A. Senftleben, A. M. Sayler, T. Rathje, T. Pfeifer, I. Ben-Itzhak, R. R. Jones, G. G. Paulus, F. Krausz, R. Moshammer, J. Ullrich, and M. F. Kling, Nat. Commun. **3**, 813 (2012).

[60] T. Rathje, N. G. Johnson, M. Möller, F. Süß mann, D. Adolph, M. Kübel, R. Kienberger, M. F. Kling, G. G. Paulus, and A. M. Sayler, J. Phys. B **45**, 074003 (2012).

[61] A. M. Sayler, T. Rathje, W. Müller, C. Kürbis, K. Rühle, G. Stibenz, and G. G. Paulus, Opt. Express **19**, 4464 (2011).

[62] K. J. Betsch, N. G. Johnson, B. Bergues, M. Kübel, O. Herrwerth, A. Senftleben, I. Ben-Itzhak, G. G. Paulus, R. Moshammer, J. Ullrich, M. F. Kling, and R. R. Jones, Phys. Rev. A **86**, 063403 (2012).

[63] F. Grasbon, G. Paulus, H. Walther, P. Villoresi, G. Sansone, S. Stagira, M. Nisoli, and S. De Silvestri, Phys. Rev. Lett. **91**, 173003 (2003).

[64] G. N. Gibson, R. R. Freeman, and T. J. McIlrath, Phys. Rev. Lett. **67**, 1230 (1991).

[65] C. Guo, M. Li, J. Nibarger, and G. Gibson, Phys. Rev. A **58**, R4271 (1998).

[66] D. C. Cartwright and T. Dunning, J. Phys. B **8**, L100 (1975).

[67] S. Micheau, Z. Chen, A.-T. Le, and C. Lin, Phys. Rev. A **79**, 013417 (2009).

[68] Z. Chen, Y. Liang, D. H. Madison, and C. D. Lin, Phys. Rev. A **84**, 023414 (2011).

[69] T. Pischke, *Phase- and Intensity-Resolved Photoionization of Noble Gases with Femtosecond Laser Pulses*, Bachelor thesis, Technische Universität München (2013).

[70] M. Kübel, K. J. Betsch, N. G. Johnson, U. Kleineberg, R. Moshammer, J. Ullrich, G. G. Paulus, M. F. Kling, and B. Bergues, New J.Phys. **14**, 093027 (2012).

[71] S. Chelkowski, A. Bandrauk, and A. Apolonski, Phys. Rev. A **70**, 013815 (2004).

[72] A. Emmanouilidou and A. Staudte, Phys. Rev. A **80**, 053415 (2009).

[73] F. Mauger, a. Kamor, C. Chandre, and T. Uzer, Phys. Rev. Lett. **108**, 063001 (2012).

[74] C. Huang, Y. Zhou, Q. Zhang, and P. Lu, Opt. Express **21**, 11382 (2013).

[75] S. D. Price, J. H. D. Eland, P. G. Fournier, J. Fournier, and P. Millie, J. Chem. Phys. **88** (1988).

[76] X. Zhou, P. Ranitovic, C. W. Hogle, J. H. D. Eland, H. C. Kapteyn, and M. M. Murnane, Nat. Phys. **8**, 232 (2012).

[77] N. Kotsina, S. Kaziannis, S. Danakas, and C. Kosmidis, J. Chem. Phys. **139**, 104313 (2013).

[78] I. Znakovskaya, P. von den Hoff, S. Zherebtsov, A. Wirth, O. Herrwerth, M. Vrakking, R. de Vivie-Riedle, and M. Kling, Phys. Rev. Lett. **103**, 103002 (2009).

[79] I. Znakovskaya, P. von den Hoff, N. Schirmel, G. Urbasch, S. Zherebtsov, B. Bergues, R. de Vivie-Riedle, K.-M. Weitzel, and M. F. Kling, Phys. Chem. Chem. Phys. **13**, 8653 (2011).

[80] N. G. Kling, K. J. Betsch, M. Zohrabi, S. Zeng, F. Anis, U. Ablikim, B. Jochim, Z. Wang, M. Kübel, M. F. Kling, K. D. Carnes, B. D. Esry, and I. Ben-Itzhak, Phys. Rev. Lett. **111**, 163004 (2013).

[81] T. Rathje, A. M. Sayler, S. Zeng, P. Wustelt, H. Figger, B. D. Esry, and G. G. Paulus, Phys. Rev. Lett. **111**, 093002 (2013).

[82] M. F. Kling, P. von den Hoff, I. Znakovskaya, and R. de Vivie-Riedle, Phys. Chem. Chem. Phys. **15**, 9448 (2013).

[83] A. S. Alnaser, I. Litvinyuk, T. Osipov, B. Ulrich, A. Landers, E. Wells, C. M. Maharjan, P. Ranitovic, I. Bochareva, D. Ray, and C. L. Cocke, Journal of Physics B: Atomic, Molecular and Optical Physics **39**, S485 (2006).

[84] A. N. Pfeiffer, C. Cirelli, M. Smolarski, X. Wang, J. H. Eberly, R. Dörner, and U. Keller, New J.Phys. **13**, 093008 (2011).

[85] C. F. de Morisson Faria and T. Das, "Personal communication," (2013).

[86] J. Guo, X.-S. Liu, and S.-I. Chu, Phys. Rev. A **88**, 023405 (2013).

[87] P. Eckle, M. Smolarski, P. Schlup, J. Biegert, A. Staudte, M. Schöffler, H. G. Muller, R. Dörner, and U. Keller, Nat. Phys. **4**, 565 (2008).

[88] G. Cerullo, A. Baltuška, O. D. Mücke, and C. Vozzi, Laser Photon. Rev. **5**, 323 (2011).

[89] A. Rudenko, V. de Jesus, T. Ergler, K. Zrost, B. Feuerstein, C. Schröter, R. Moshammer, and J. Ullrich, Phys. Rev. Lett. **99**, 263003 (2007).

[90] L. Moore, M. Lysaght, L. Nikolopoulos, J. Parker, H. van der Hart, and K. Taylor, J. Mod. Opt. **58**, 1132 (2011).

Acknowledgements

At this point, I would like to thank all people who have supported me during this long and productive journey.

For all conceivable support, I am utterly grateful to my supervisor Matthias Kling. I feel honored by the great deal of trust he put into my work. Furthermore, I want to thank him and Ferenc Krausz for the opportunity to do my PhD work in the fruitful environment of MPQ and LMU.

I would like to express my deepest gratitude to Boris Bergues for the productive, friendly and enjoyable cooperation over the past years. His persistent skepticism has taught me to always be prepared to reconsider any assumptions I have made and has helped to improve our work time and again.

For his straightforward cooperation I want to thank Reinhard Kienberger.

There are numerous facets to laboratory work. For sharing these moments of success, frustration, discovery, surprise, and hard (physical) work with me, I would like to thank Nora Kling, Kelsie Betsch, Boris Bergues, Matthias Kling, Ali Alnaser, Oliver Herrwerth, Thomas Pischke, Benjamin Förg, Hui Li, Frederik Süßmann, Sergey Zherebtsov, Irina Znakovskaya, and my successor Christian Jendrzejewski.

For the kind collaboration at the AS-1 laser, my thanks go to Eleftherios Goulielmakis and his team, in particular Mohammed Hassan, Tran Trung Luu, Antoine Moulet, and Adrian Wirth. Likewise, I would like to thank Ulf Kleineberg and his team, in particular Casey Chew and Jürgen Schmidt, for sharing their laser with us and for the fruitful teamwork at the LMU.

Furthermore, I want to thank Elisabeth Bothschafter, Yunpei Deng, Ernst Fill, Michael Jobst, Ioachim Pupeza, Alexander Kessel, Lauryna Lötscher, Fabian Lücking, Tim Paasch-Colberg, Olga Razskazovskaya, Waldermar Schneider, Wolfgang Schweinberger, Johannes Schötz, Hartmut Schröder, Johannes Stierle, Agnieszka Szolno, and Tibor Wittmann for their colleagueship, their help and interesting discussions.

For very reliable technical support my thanks go to Karl Bauer, Harald Haas, Anton Horn, Tobias Kleinhenz, Johann Krapfl, Rolf Oehm, Michael Rogg, Thomas Strobl, and the entire workshop crews at both MPQ and LMU.

The work described in this thesis has benefited from several fruitful external collaborations. Many thanks for assistance in the operation of the REMI go to Arne Senftleben, Robert Moshammer, Joachim Ullrich and Claus-Dieter Schröter, as well as to Nicolas Camus and Andreas Kaldun for experimental support.

In the prolific collaboration with the Heidelberg group we have carried out a variety of highly insightful XUV-pump XUV-probe experiments at the Free Electron Laser in Hamburg (FLASH), which have also had a great deal of educational aspects to me. For the warm welcome, helpful discussions and also good times I want to thank the entire FLASH-REMI team, in particular

Arne Senftleben, Kirsten Schnorr, Artem Rudenko, Thomas Pfeifer, Yuhai Jiang, Kristina Meyer, Moritz Kurka, Robert Moshammer and Joachim Ullrich.

For the warm hospitality during my stay in Kansas and for his valuable suggestions I am grateful to Itzik Ben-Itzhak.

Special thanks for his continued support and stimulating discussions go to my Diplomvater Gerhard Paulus.

For the support and wonderful events organized by the IMPRS-APS I would like to acknowledge the scientific coordinators Peter Hommelhoff, Vladislav Yakovlev and Nick Karpowicz, as well as the coordinator of everything, Monika Wild.

Last but not least, I am fortunate to have an exceedingly supportive family. Vielen Dank!